

**NET POWER OUTPUT AND PRESSURE DROP BEHAVIOR OF  
PEM FUEL CELLS WITH SERPENTINE AND INTERDIGITATED  
FLOW FIELDS**

by

Fang Ruan

A thesis submitted to the Faculty of the University of Delaware in partial fulfillment of the requirements for the degree of Master of Science in Mechanical Engineering

Spring 2014

© 2014 Fang Ruan  
All Rights Reserved

UMI Number: 1562417

All rights reserved

INFORMATION TO ALL USERS

The quality of this reproduction is dependent upon the quality of the copy submitted.

In the unlikely event that the author did not send a complete manuscript and there are missing pages, these will be noted. Also, if material had to be removed, a note will indicate the deletion.



UMI 1562417

Published by ProQuest LLC (2014). Copyright in the Dissertation held by the Author.

Microform Edition © ProQuest LLC.

All rights reserved. This work is protected against unauthorized copying under Title 17, United States Code



ProQuest LLC.  
789 East Eisenhower Parkway  
P.O. Box 1346  
Ann Arbor, MI 48106 - 1346

**NET POWER OUTPUT AND PRESSURE DROP BEHAVIOR OF  
PEM FUEL CELLS WITH SERPENTINE AND INTERDIGITATED  
FLOW FIELDS**

by

Fang Ruan

Approved: \_\_\_\_\_  
Ajay Prasad, Ph.D.  
Professor in charge of thesis on behalf of the Advisory Committee

Approved: \_\_\_\_\_  
Suresh Advani, Ph.D.  
Professor in charge of thesis on behalf of the Advisory Committee

Approved: \_\_\_\_\_  
Suresh Advani, Ph.D.  
Chair of the Department of Mechanical Engineering

Approved: \_\_\_\_\_  
Babatunde Ogunnaike, Ph.D.  
Dean of the College of Engineering

Approved:

\_\_\_\_\_  
James G. Richards, Ph.D.

Vice Provost for Graduate and Professional Education

## ACKNOWLEDGMENTS

I would like to thank the Fuel Cell Research Lab and the Federal Transit Administration for funding me throughout my graduate studies. This program provided me precious and unique opportunity to get involved in cutting-edge research in sustainable energy, and it also inspired my interest in working in the renewable energy industry in my future career.

First and foremost, I would also like express my deepest gratitude to both of my advisors: Dr. Ajay Prasad and Dr. Suresh Advani. Their vast knowledge, great vision combined with the consistent guidance in technical details providing me tremendous help throughout my research work in the past two years. They also offered me the freedom to explore my own research interest as well as encouragement and guidance when I meet difficulties and frustration. Without their excellent advisement, I would not be able to finish this thesis and reach my academic goals.

My sincere gratitude is also given to all of the Fuel Cell Research Lab associates for their help with various stages of my project. In particular, I owe thanks to Dr. Liang Wang for offering lab training, general knowledge and deep understanding in PEM fuel cell principles and testing, tenacity to help to solve problems that I encountered, Andrew Baker for his help with generating SolidWorks drawings for manufacturing, Yongqiang Wang for his help with setting up pressure measurement equipment, Jaehyung Park for his advice and help with fuel cell test training, and Adam Kinzey for his help with manufacturing parts for the Arbin fuel

cell test stand. I also want to thank Mr. Steve Beard for his guidance and help in machining the metal parts for the PEM fuel cell in the Spencer machine shop.

I especially thank my parents, for their continued support, love, concern and motivation throughout all of my endeavors. I also would like to thank my boyfriend Chenglong Zheng for his consistent love, support and understanding in the past two years. I'm also thankful to all my friends for the enjoyable time we shared and great help they provided in work and in life.

Most importantly, I want to give my thanks to my dear God, who has led and sustained me through my life, and always been with me in my best and toughest times. Grace from God is the major source of my strength, ability and enjoyment.

## TABLE OF CONTENTS

LIST OF FIGURES .....	ix
LIST OF TABLES .....	xvi
ABSTRACT .....	xvi
Chapter	
1 INTRODUCTION .....	1
1.1 Overview of PEM Fuel Cells .....	1
1.2 Previous Studies on Fuel Cell Power Analysis and Pressure Drop Behavior .....	5
1.3 Research Objectives and Test Procedures .....	8
1.4 Thesis Overview .....	11
2 EXPERIMENT SETUP AND TEST PROCEDURE .....	12
2.1 Fuel Cell Components and Design .....	12
2.2 Fuel Cell Test Station .....	13
2.3 Pressure Measurement Station .....	14
2.4 Test Procedure .....	16
2.5 Summary.....	16
3 RESULTS OF NET POWER WITH DIFFERENT FLOW FIELD COMBINATIONS .....	17
3.1 Pressure Drop in Four Flow Fields Combinations .....	17
3.2 Effect of Operating Conditions on Pressure Drop.....	22
3.3 Parasitic Power Loss Calculation and Net Power .....	26
3.4 Power Efficiency Discussion.....	30
3.5 Effect of Operating Conditions on Net Power Output and Power Efficiency .....	30
3.6 Summary.....	48
4 PRESSURE DROP BEHAVIOR IN PEM FUEL CELLS UNDER FLUCTUATING HUMIDIFICATION TEMPERATURES.....	50
4.1 Correlation Between Fuel Cell Voltage and Anode Pressure Drop .....	50
4.2 Correlation Between Fuel Cell Current Density and Pressure Drop .....	56

4.3	Correlation Coefficients .....	59
4.4	Discussion.....	60
4.5	Summary.....	61
5	CONCLUSION AND FUTURE WORK .....	62
	REFERENCES .....	65
	Appendix	
	A CALCULATION OF COMPRESSOR POWER.....	68
	B PRESSURE DROP AND CELL OUTPUT DATA.....	73
	C PERMISSION FOR FIGURE USAGE... ..	92

## LIST OF FIGURES

Figure 1.1	Structure of PEM fuel cell and associated chemical reactions [3].....	3
Figure 1.2	Schematics of single serpentine, parallel and interdigitated flow field design [4].....	4
Figure 2.1	Schematics of interdigitated and single serpentine flow field designs built and tested in this work.....	13
Figure 2.2	Details of the Arbin fuel cell test stand.....	14
Figure 2.3	Schematic of connection the four pressure sensors to the cell.....	15
Figure 2.4	Use of a water-filled burette to calibrate the pressure sensors using a Labview program.....	15
Figure 3.1	Average pressure drop in each flow field during discharge at 0.6 V under standard operating conditions for 30 minutes .....	19
Figure 3.2	Pressure drop profile in ASCS flow field during discharge at 0.6 V under standard operating conditions for 30 minutes .....	20
Figure 3.3	Pressure drop profile in ASCI flow field during discharge at 0.6 V under standard operating conditions for 30 minutes .....	20
Figure 3.4	Pressure drop profile in AICS flow field during discharge at 0.6 V under standard operating conditions for 30 minutes .....	21
Figure 3.5	Pressure drop profile in AICI flow field during discharge at 0.6 V under standard operating conditions for 30 minutes .....	21
Figure 3.6	Pressure drop in AICS cell at oxygen flow rates of 1, 2, and 4 slpm.....	22
Figure 3.7	Pressure drop profile in AICS flow field during discharge at 0.6V and oxygen flow rate 1 slpm for 30 minutes.....	23
Figure 3.8	Pressure drop profile in AICS flow field during discharge at 0.6V and oxygen flow rate of 4 slpm for 30 minutes.....	23

Figure 3.9	Average pressure drop in each flow field during discharge at 0.6 V for 30 minutes at 60°C and 70°C .....	24
Figure 3.10	Average pressure drop in each flow field during discharge at 0.6 V for 30 minutes at 50% cathode RH 100% cathode RH.....	25
Figure 3.11	Average pressure drop in each flow field during discharge at 0.5, 1, and 1.5 A/cm <sup>2</sup> for 30 minutes .....	26
Figure 3.12	Average total power output, parasitic power loss and net power in each cell; cells were operated at standard operating conditions for 30 minutes at 0.6 V. Net power is defined as the difference between total power output and parasitic power loss. The quoted values are in watts..	28
Figure 3.13	Average net power in each cell; cells were operated at standard operating condition for 30 minutes at 0.6 V. Standard deviations were calculated from three tests for total power output and parasitic loss to assess variations in test results within the same group of experiments ...	28
Figure 3.14	Power efficiency of each flow field at standard operation conditions at 0.6 V .....	30
Figure 3.15	Average total power output, parasitic power loss and net power in each cell; oxygen flow rate was 4 slpm and other conditions remain the same. Cells were operated for 30 minutes at 0.6 V.....	31
Figure 3.16	Power efficiency of each flow field at oxygen flow rate of 4 slpm at 0.6 V .....	32
Figure 3.17	Current density and voltage profile of ASCI cell during discharge at 0.6V and oxygen flow rate of 4 slpm for 30 minutes .....	33
Figure 3.18	Average total power output, parasitic power loss and net power in each cell; oxygen flow rate was 1 slpm and other conditions remain the same. Cells were operated for 30 minutes at 0.6 V.....	34
Figure 3.19	Power efficiency of each flow field at oxygen flow rate of 1 slpm at 0.6 V .....	35
Figure 3.20	Current density and voltage profile of ASCI cell during discharge at 0.6V and oxygen flow rate of 1 slpm for 30 minutes .....	35

Figure 3.21	Average total power output, parasitic power loss and net power in each cell; cell temperature was 60°C and other conditions remain the same. Cells were operated for 30 minutes at 0.6 V.....	37
Figure 3.22	Power efficiency of each flow field at cell temperature of 60°C and 0.6 V .....	38
Figure 3.23	Current density and voltage profile of ASCI cell during discharge at 0.6V and 60°C for 30 minutes.....	38
Figure 3.24	Average total power output, parasitic power loss and net power in each cell; anode RH was 50% and other conditions remain the same. Cells were operated for 30 minutes at 0.6 V.....	39
Figure 3.25	Average total power output, parasitic power loss and net power in each cell; cathode RH was 50% and other conditions remain the same. Cells were operated for 30 minutes at 0.6 V.....	40
Figure 3.26	Power efficiency of each flow field at anode RH 50% and 0.6 V .....	40
Figure 3.27	Power efficiency of each flow field at cathode RH 50% and 0.6 V .....	41
Figure 3.28	Current density and voltage profile of ASCI cell during discharge at 0.6V and anode RH 50% for 30 minutes.....	41
Figure 3.29	Current density and voltage profile of ASCI cell during discharge at 0.6V at cathode RH 50% for 30 minutes.....	42
Figure 3.30	Average total power output, parasitic power loss and net power in each cell; cells were operated at standard operating conditions for 30 minutes at 0.5 A/cm <sup>2</sup> .....	43
Figure. 3.31	Average total power output, parasitic power loss and net power in each cell; cells were operated at standard operation condition for 30 minutes discharging at 1A/cm <sup>2</sup> . .....	44
Figure 3.32	Average total power output, parasitic power loss and net power in each cell; cells were operated at standard operating conditions for 30 minutes at 1.5 A/cm <sup>2</sup> .....	44
Figure 3.33	Power efficiency of each flow field at standard operating conditions and 0.5 A/cm <sup>2</sup> .....	44
Figure 3.34	Power efficiency of each flow field at standard operating conditions and 1 A/cm <sup>2</sup> .....	45

Figure 3.35	Power efficiency of each flow field at standard operating conditions and $1.5 \text{ A/cm}^2$ .....	46
Figure 3.36	Current density and voltage profile of ASCI cell during discharge at $0.5 \text{ A/cm}^2$ for 30 minutes.....	47
Figure 3.37	Current density and voltage profile of ASCI cell during discharge at $1 \text{ A/cm}^2$ for 30 minutes.....	47
Figure 3.38	Current density and voltage profile of ASCI cell during discharge at $1.5 \text{ A/cm}^2$ for 30 minutes.....	48
Figure 4.1	Pressure drop profile in each flow field at $0.5 \text{ A/cm}^2$ after switching from OCV (2 slpm oxygen flow rate); anode humidification temperature fluctuates in the range of $\pm 20^\circ\text{C}$ . Upper left: ASCS; Upper right: AICI; Lower left: AICS; Lower right: ASCI. ....	51
Figure 4.2	AICI cell test at $0.5 \text{ A/cm}^2$ . Upper left: fuel cell performance data; lower left: anode and cathode pressure drop; right: anode pressure drop and voltage data.....	52
Figure 4.3	AICI cell test at $0.5 \text{ A/cm}^2$ . Upper: time evolution over 30 min of current density overlaid with the anode pressure drop. The other two sub-plots are close-up views of the two spikes over a narrow time span.....	53
Figure 4.4	Humidification temperature and voltage data for the AICI cell at $0.5 \text{ A/cm}^2$ for 30 minutes.....	55
Figure 4.5	ASCI cell test at $0.6 \text{ V}$ . Upper left: fuel cell performance data; lower left: anode and cathode pressure drop; right: anode pressure drop and voltage data.....	56
Figure 4.6	ASCI cell test at $0.6 \text{ V}$ . Upper left: time evolution over 30 min of current density overlaid with the anode pressure drop. The other three sub-plots are close-up views of the three spikes over a narrow time span. ....	58
Figure 4.7	Humidification temperature and voltage data for the ASCI cell at $0.6 \text{ V}$ for 30 minutes.....	59
Figure 4.8	Correlation coefficients of anode pressure drop and cell current density at $0.6 \text{ V}$ .....	60

Figure 4.9	Correlation coefficients of anode pressure drop and cell voltage at $0.5\text{A}/\text{cm}^2$ .....	60
Figure B.1	Pressure drop profile in ASCI flow field during discharge at 0.6V and oxygen flow rate of 1 slpm for 30 minutes.....	73
Figure B.2	Pressure drop profile in AICI flow field during discharge at 0.6V and oxygen flow rate of 1 slpm for 30 minutes.....	74
Figure B.3	Pressure drop profile in ASCS flow field during discharge at 0.6V and oxygen flow rate of 1 slpm for 30 minutes.....	75
Figure B.4	Pressure drop profile in ASCI flow field during discharge at 0.6V and oxygen flow rate of 4 slpm for 30 minutes.....	75
Figure B.5	Pressure drop profile in AICI flow field during discharge at 0.6V and oxygen flow rate of 4 slpm for 30 minutes.....	76
Figure B.6	Pressure drop profile in ASCS flow field during discharge at 0.6V and oxygen flow rate of 4 slpm for 30 minutes.....	76
Figure B.7	Pressure drop profile in ASCI flow field during discharge at 0.6V cathode RH 50% for 30 minutes .....	77
Figure B.8	Pressure drop profile in AICI flow field during discharge at 0.6V and cathode RH 50% for 30 minutes .....	77
Figure B.9	Pressure drop profile in ASCS flow field during discharge at 0.6V and cathode RH 50% for 30 minutes .....	78
Figure B.10	Pressure drop profile in ASCI flow field during discharge at 0.6V and $60^\circ\text{C}$ for 30 minutes.....	78
Figure B.11	Pressure drop profile in AICS flow field during discharge at 0.6V and $60^\circ\text{C}$ for 30 minutes.....	79
Figure B.12	Pressure drop profile in AICI flow field during discharge at 0.6V and $60^\circ\text{C}$ for 30 minute .....	79
Figure B.13	Pressure drop profile in ASCI flow field during discharge at 0.6V and $60^\circ\text{C}$ for 30 minutes.....	80
Figure B.14	Performance profile in AICI flow field during discharge at 0.6V under standard operating condition for 30 minutes .....	80

Figure B.15	Performance profile in ASCS flow field during discharge at 0.6V under standard operating condition for 30 minutes.....	81
Figure B.16	Performance in ASCI flow field during discharge at 0.6V under standard operating condition for 30 minutes.....	81
Figure B.17	Performance profile in AICS flow field during discharge at 0.6V under standard operating condition for 30 minutes.....	82
Figure B.18	Performance profile in AICS flow field during discharge at 0.6V and 60°C for 30 minutes.....	82
Figure B.19	Performance profile in ASCS flow field during discharge at 0.6V and 60°C for 30 minutes.....	83
Figure B.20	Performance profile in AICI flow field during discharge at 0.6V and 60°C for 30 minutes.....	83
Figure B.21	Performance profile in AICS flow field during discharge at 0.6V and cathode RH 50% for 30 minutes.....	84
Figure B.22	Performance profile in AICI flow field during discharge at 0.6V cathode RH 50% for 30 minutes.....	84
Figure B.23	Performance profile in ASCS flow field during discharge at 0.6V and cathode RH 50% for 30 minutes.....	85
Figure B.24	Performance profile in AICS flow field during discharge at 0.6V and oxygen flow rate of 4 slpm for 30 minutes.....	85
Figure B.25	Performance profile in AICI flow field during discharge at 0.6V and oxygen flow rate of 4 slpm for 30 minutes.....	86
Figure B.26	Performance profile in ASCS flow field during discharge at 0.6V and oxygen flow rate of 4 slpm for 30 minutes.....	86
Figure B.27	Performance profile in ASCS flow field during discharge at 0.5A/cm <sup>2</sup> for 30 minutes.....	87
Figure B.28	Performance profile in AICS flow field during discharge at 0.5A/cm <sup>2</sup> for 30 minutes.....	87
Figure B.29	Performance profile in AICI flow field during discharge at 0.5A/cm <sup>2</sup> for 30 minutes.....	88

Figure B.30 Performance profile in AICS flow field during discharge at $1.0\text{A}/\text{cm}^2$ for 30 minutes.....	88
Figure B.31 Performance profile in AICI flow field during discharge at $1.0\text{A}/\text{cm}^2$ for 30 minutes.....	89
Figure B.32 Performance profile ASCS flow field during discharge at $1.0\text{A}/\text{cm}^2$ for 30 minutes .....	89
Figure B.33 Performance profile AICS flow field during discharge at $1.5\text{A}/\text{cm}^2$ for 30 minutes .....	90
Figure B.34 Performance profile in AICI flow field during discharge at $1.5\text{A}/\text{cm}^2$ for 30 minutes.....	90
Figure B.35 Performance profile in ASCS flow field during discharge at $1.5\text{A}/\text{cm}^2$ for 30 minutes.....	91

## LIST OF TABLES

Table 1.1	Flow field combinations used in this work.....	9
Table 1.2	Operating conditions employed in tests (green area is the base line).....	10
Table 3.1	P-values for the net power results for the ASCI and ASCS flow fields at each specific operating condition .....	29
Table A.1	Voltage=0.6V; oxygen flow rate=2 slpm; temperature=70°C; anode RH=50%; cathode RH=100% .....	69
Table A.2	Voltage=0.6V; oxygen flow rate=2; slpm temperature=70°C; anode RH=100%; cathode RH=50% .....	69
Table A.3	Voltage=0.6V; oxygen flow rate=1 slpm; temperature=70°C; anode RH=100%; cathode RH=100% .....	70
Table A.4	Voltage=0.6V; oxygen flow rate=4; slpm temperature=70°C; anode RH=100%; cathode RH=100% .....	70
Table A.5	Voltage=0.6V; oxygen flow rate=2; slpm temperature=60°C; anode RH=100%; cathode RH=100% .....	71
Table A.6	Voltage=0.6V; oxygen flow rate=2; slpm temperature=70°C; anode RH=100%; cathode RH=100% .....	71
Table A.7	Current density 1A/cm <sup>2</sup> ;oxygen flow rate=2; slpm temperature=70°C; anode RH=100%; cathode RH = 100%.....	72
Table A.8	Current density=1.5A/cm <sup>2</sup> ;oxygen flow rate=2; slpm temperature=70°C; anode RH=100%; cathode RH=100% .....	72
Table A.9	Current density=0.5A/cm <sup>2</sup> ;oxygen flow rate=2; slpm temperature=70°C; anode RH=100%; cathode RH=100% .....	72

## **ABSTRACT**

Experiments were conducted with proton exchange membrane fuel cells (PEMFC) incorporating two different anode and cathode flow field designs to carry the reactants and products to and from the cell. The net performance of the PEMFC was experimentally measured for each case. The net power output from two conventional flow fields: (i) serpentine flow fields on both anode and cathode (ASCS), and (ii) interdigitated flow fields on both anode and cathode (AICI) were compared with two alternate combination flow fields: (i) serpentine on the anode and interdigitated on the cathode (ASCI), and (ii) interdigitated on the anode with serpentine on the cathode (AICS). A fuel cell test stand was used to record the gross power generated by the PEMFC at fixed currents and voltages. The parasitic power consumed by the air compressor was obtained by employing pressure transducers to measure the pressure drop across the cathode flow field. It was found that the pressure drop in the interdigitated channel was much lower than that in the serpentine channel, so the parasitic power loss incurred by the use of the compressor was much lower when the interdigitated flow field is used on the cathode side. The effect of operating conditions including temperature, relative humidity, oxygen flow rate and current density on the pressure drop and net power output is also explored.

ANOVA analysis was performed to suggest confidence levels for the results obtained. Results show that the ASCI cell has the best net power output out of the four sets of flow field combinations under all the operating conditions applied. Energy

efficiency is calculated for each case, and the influence of the flow field combination and operating conditions on energy efficiency is presented.

## **Chapter 1**

### **INTRODUCTION**

#### **1.1 Overview of PEM Fuel Cells**

Environmental concerns about modern society's dependence upon reliable energy sources and global warming have created the need for sustainable energy sources with high energy-conversion efficiency. Among various technologies developed to reduce the consumption of fossil fuels, hydrogen-powered fuel cells are a promising alternative. Proton exchange membrane fuel cell (PEMFC), which is also called solid polymer fuel cell (SPFC), is a device that can convert chemical energy directly into electrical energy through an electrochemical reaction between hydrogen and oxygen in the presence of a catalyst. The only byproduct of this electrochemical process is water and heat, which makes it environment-friendly. The well-to-wheel energy efficiency for fuel cells is higher than conventional energy conversion devices such as the internal combustion engine for automotive applications, and the steam turbine for stationary power applications [1]. The low operating temperature of the PEMFC guarantees a quick startup and safe operation for automotive applications. There are no moving parts in the PEMFC, which increases its life span, and also reduces operating noise [2]. Based on all the advantages mentioned above, the PEMFC has been considered as one of the best renewable energy sources for the automotive and portable electronics industries for its high power density, clean operation, low operating temperature, and high energy efficiency.

The main components in PEMFCs include a solid membrane, two catalyst-coated electrodes, two gas diffusion layers (GDLs), and two bipolar plates (flow field plates). The schematic of the PEMFC is shown in Fig. 1.1. Reactant gases are fed through the gas channels and diffuse through the GDLs to reach the electrodes, where the electrochemical reactions take place. At the anode, hydrogen splits into protons and electrons as follows:



$H^+$  ions are conducted through the electrolyte to the cathode catalyst layer. Electrons produced at the anode are conducted through the bipolar plates and the external circuit which provides the electricity and arrive at the cathode electrode. Oxygen fed through the cathode gas channel reacts with  $H^+$  ions and electrons to create water and heat:



The sum total of the reaction is that hydrogen and oxygen are consumed, while water, electricity and heat are produced. About 50% of the energy in the fuel is converted into electricity, and the rest is converted to heat [5].

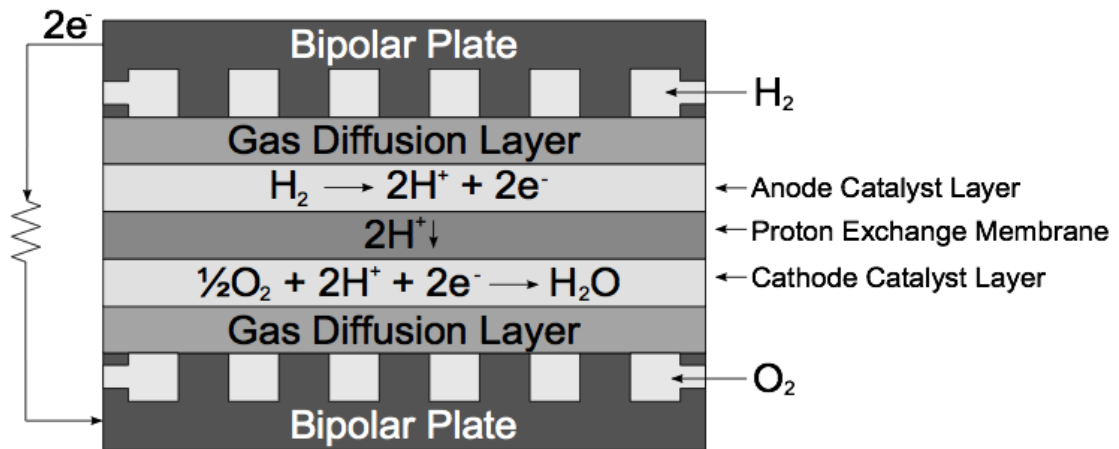
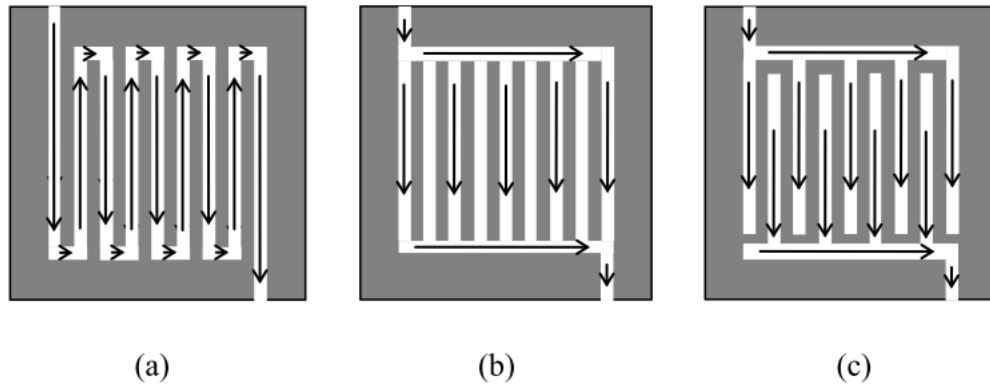


Figure 1.1 Structure of PEM fuel cell and associated chemical reactions [3]

As shown in Fig.1.1, the bipolar plates incorporate channels to transport the reactant gases to the cell, act as current collectors to transfer the electrons to the external circuit to generate electricity, and provide the structural support necessary for the fuel cell. Bipolar plates are typically made of graphite or aluminum, or composite materials for considerations of high electrical and thermal conductivity, durability, low cost, and low weight and volume [6]. Gas channels are cut into the inner surface of the bipolar plates, and the ribs located in between adjacent channels make contact with the GDL. The most important functions of the bipolar plates are (i) distributing reactant gases to the fuel cell electrodes, (ii) removal of product water, excess reactant gases and heat, and (iii) transporting electrons. There are three standard types of gas channel designs that are routinely used in PEM fuel cells: single-serpentine, parallel, and interdigitated. Schematics of these channel designs are shown in Fig. 1.2.



**Figure 1.2 Schematics of single serpentine, parallel and interdigitated flow field design [4]**

The material and geometry of the channels inscribed in the bipolar plate can have a major influence on the PEM fuel cell's overall performance due to the role it plays in gas and electron transport, and water and heat management. Spornjak et al. [7] compared the performance and power output of PEM fuel cells with parallel, single-serpentine and interdigitated flow fields, and found that the single-serpentine flow field yielded the best and most stable output; the interdigitated flow field exhibited performance which was comparable to the single-serpentine cell except at high current densities, whereas the parallel cell exhibited much lower and unstable output.

Besides the flow field's influence on cell output, the performance of PEMFCs is also influenced by the operating conditions such as the operating pressure, temperature, relative humidity (RH), and flow rates of reactant gases. Parametric studies of operating conditions has been carried out by Wang et al. [9], and the experimental results showed the effects of operating temperature, anode/cathode RH, operating pressure, and various combinations of these parameters. Higher pressure in the cell can boost its performance according to the Nernst equation and reduce mass transport voltage losses at high current densities. Balasubramanin et al. [10] also revealed that higher operating pressures can improve fuel cell performance. The

voltage of a single fuel cell was improved from 0.5 V to 0.6 V at a current density of 1200 mA/cm<sup>2</sup> when the operating pressure was increased from 170 kPa to 300 kPa. However, the power consumed by the compressor also increased by 100% when the pressure was increased from 170 kPa to 300 kPa, which increases the parasitic power loss by 30%. This parasitic power loss has to be subtracted from the fuel cell's total power output, thus offsetting the voltage gain at higher operating pressures.

To supply reactant gases and operate the fuel cell under selected operating conditions, auxiliary components are needed in the fuel cell system. Pumps, fans, compressors, blowers, heaters, humidifiers, and a cooling system are the major components in the gas supply and thermal management system. Among these components, the air compressor is the major source of power loss in the fuel cell system. Air must be compressed and driven into fuel cell system by the compressor, and work is done on the gas to raise its pressure and temperature. In this work, we define the parasitic power loss as the power consumed by the compressor, which is a function of the pressure drop inside the fuel cell, as described in Chapter 2. A previous study showed that the typical compressor power consumption would be about 20% or more of the total power generated [10]. Flow field designs that cause a higher pressure drop across the flow field channel will increase the reactant pumping power and reduce the system performance [6, 11]. Spornjak et al. [7] also showed that water dynamics and parasitic power loss (the power needed to pump the reactant gases through the flow field) in different flow fields might vary substantially.

## **1.2 Previous Studies on Fuel Cell Power Analysis and Pressure Drop Behavior**

Pressure requirements to pump the reactant gases at a given mass flow rate will depend on the flow field design. For a given width and height of the flow channel, the

overall length and architecture of the flow field will determine the associated pressure drop. Accordingly, the channel pressure gradient across a serpentine flow field is the highest, followed by the interdigitated flow field which experiences a moderate pressure gradient, followed by the parallel flow field which has the lowest channel pressure drop [6], as explained below.

Let the number of ribs in the flow field be  $N$ , and the length of each rib  $L$ ; from the schematics of the three types of flow fields shown in Figure 1.2, the serpentine flow field has one continuous flow channel whose total length is  $L(N + 1)$ ; the parallel flow field has  $(N + 1)$  flow channels each of length  $L$ ; the interdigitated flow field has  $(N + 1)/2$  flow channels on the inlet side, and the length of each channel is  $L$ .

According to Darcy's law, pressure drop for incompressible pipe flow is:

$$\Delta p = f \frac{L\rho\bar{V}^2}{2D_H} \quad 1.3$$

where  $f$  is the friction factor,  $L$  is the channel length,  $\rho$  is the fluid density,  $\bar{V}$  is the flow velocity, and  $D_H$  is the hydraulic diameter. As the channel length in the single-serpentine flow field is much larger than that of the parallel flow field, one can see from Eq. 1.3 that the pressure drop in a single serpentine flow field from inlet to outlet will be higher. In the case of the interdigitated flow field, the pressure drop calculation is more complicated because the gas has to transit from the inlet to the exit channels by passing through the GDL underneath the lands. The pressure drop through the porous GDL has to be added to the pressure drop in the channel to obtain the total pressure drop for the interdigitated design [8].

A higher pressure gradient from the inlet to the outlet requires higher supply pressure for hydrogen on the anode side and air on the cathode side, causing higher power consumption by the compressor, thereby increasing the parasitic losses and lowering the net system power output. Hence the ideal flow field is the one that can deliver the highest *net* system power output.

A simple cost/benefit study performed by Spernjak et al. [13] showed that at low to moderate current densities, the interdigitated flow field gives better PEMFC system performance than the single-serpentine flow field due to lower parasitic power loss in the compressor. To calculate compressor power for each cell as well as to study the relationship between water dynamics and pressure drop behavior, Spernjak et al. [13] measured the pressure drop across both anode and cathode flow fields as a function of time while recording polarization curves, during cell startup at a constant voltage of 0.2 V, and at a constant current density of 0.5 A/cm<sup>2</sup> for 30 minutes after cell was operated at OCV for 30 minutes. They found a positive correlation between pressure drop and water content, and a negative correlation between pressure drop and cell performance because a higher pressure drop indicates water flooding in flow channels; a sudden drop of pressure difference denoted water removal from the flow channels and a recovery of cell performance.

The pressure drop behavior from inlet to outlet was used to detect water flooding by Barbir et al [10, 11] at General Motors. The pressure drop increases when liquid water accumulates, and decreases when water is removed from the cell. General Motors patented a method to detect and correct water flooding in PEMFCs by monitoring the pressure drop across the flow fields and comparing them against a threshold reference pressure drop [14, 15]. If the actual pressure drop exceeded the

threshold reference pressure drop, corrective action would be triggered such as reducing the RH, increasing the gas flow rate, reducing the stack current draw, and reducing the absolute pressure. The effect of cell temperature, operating time and current density on the cathode pressure drop was investigated by Liu et al. [12] in a parallel cell. Visualization of liquid water in both anode and cathode flow channels in an operating cell showed that the pressure drop depended strongly on the liquid water content in the flow channels, and that it increased with current density and operating time.

### **1.3 Research Objectives and Test Procedures**

To improve PEMFCs' energy efficiency, one could investigate the use of different channel designs on the cathode and anode sides with a focus on reducing the parasitic power losses and thus improving the net power output in PEMFCs. It has been shown in previous studies that serpentine flow fields exhibit better cell performance than interdigitated and parallel flow fields. However, they also require a larger share of the cell's output power to drive the reactants across the cell which could result in lower energy efficiency at high current density due to higher parasitic losses. The goal of this thesis is to explore flow field combinations with the serpentine flow field on one side and interdigitated on the other, to learn if either one of those combinations delivers a higher net power than either serpentine or interdigitated flow fields on both sides. Two combinations of channel layouts: (1) serpentine channel on anode and interdigitated channel on cathode (ASCI), and (2) interdigitated channel on anode and serpentine channel on cathode (AICS) will be explored at low and high current densities to identify the combination that gives the best net power output. A series of experiments has been designed to compare the net power output and energy

efficiencies of these two new flow field designs and compare them with conventional approaches employing the same channel layouts on both sides. This thesis reports results from studies with four sets of fuel cells with flow field combinations on the anode and cathode side as listed in Table 1.1:

	<b>Anode flow field</b>	<b>Cathode flow field</b>
<b>ASCS cell</b>	Single-serpentine	Single-serpentine
<b>AICI cell</b>	Interdigitated	Interdigitated
<b>AICS cell</b>	Interdigitated	Single-serpentine
<b>ASCI cell</b>	Single-serpentine	Interdigitated

**Table 1.1 Flow field combinations used in this work**

We operated each fuel cell at the operating conditions listed in Table 1.2 in order to investigate the performance of each flow field combination under different operating conditions, as well as to determine the net power by studying the effect of operating conditions on the pressure drop from the inlet and the outlet of the flow fields.

First, we define the operating condition in the green area in Table 1.2 as the baseline operating condition, and conduct baseline tests for each flow field combination. Parameters that were varied one at a time are also listed in Table 1.2. One parameter was changed at a time while using the baseline values for the remaining parameters. For example, when the influence of oxygen flow rate is explored and the flow rate is set to 1 slpm in the test, all the other parameters are set to the values in the first column, namely discharging at 0.6 V, cell temperature is 70°C, and anode and cathode RH are both 100%. As shown in Table 1.2, nine separate test conditions were run for each of the four flow field combinations. For each specific set

of test conditions, three independent runs were conducted to assess repeatability. Hence, a total of  $9 \times 4 \times 3 = 108$  tests were conducted, and the net power output and energy efficiency of the four flow field combinations compared under different operating conditions. Representative pressure drop profiles for each fuel cell were measured and monitored.

Voltage/current density	0.6 V	0.5 A/cm <sup>2</sup>	1.0 A/cm <sup>2</sup>	1.5 A/cm <sup>2</sup>
Temperature	70°C	60°C		
Anode RH	100%	50%		
Cathode RH	100%	50%		
Oxygen flow rate	2 slpm	1 slpm	4 slpm	
Hydrogen flow rate	1 slpm			

**Table 1.2 Operating conditions employed in tests (green area is the base line)**

Due to an occasional malfunction in the temperature controller of the PEMFC humidifier, the reactant gas humidifier temperature fluctuated from time to time, which affected the pressure drop and power performance of the PEMFC system. Although inadvertent, this fluctuation provided us with an opportunity to gain a better understanding of the relationship between gas channel pressure drop and fuel cell performance in realistic situations. Therefore, we conducted a detailed investigation of the pressure drop behavior at constant voltage and constant current density under large humidifier temperature fluctuations to improve our understanding of the mechanism that controls the pressure drop. The anode humidifier temperature experienced fluctuations of  $70^{\circ}\text{C} \pm 15^{\circ}\text{C}$  and the tests were run at a fixed current density of 0.5

A/cm<sup>2</sup> or a fixed voltage of 0.6 V for 30 minutes for each cell. All other operating conditions were set to the baseline conditions as listed in Table 1.2.

#### **1.4 Thesis Overview**

The goal of this study is to improve the net power output of a PEM fuel cell by employing different channel layouts on the anode and cathode sides. Net power output will be compared for all four permutations of serpentine and interdigitated flow fields on the cathode and anode sides, for different operating temperatures and relative humidities. Chapter 1 described the background and motivation for this work along with the objectives. A description of the experimental setup and fuel cell test procedure is given in Chapter 2. The representative results showing pressure drop, parasitic loss and net power output for fuel cells with different flow field layouts are presented and discussed in Chapter 3. The influence of various operating conditions such as temperature, oxygen flow rate and relative humidity on pressure drop and power output is also presented in Chapter 3. The relationship between operating conditions and energy efficiency for each flow field combination is also discussed. Chapter 4 presents the correlation between fuel cell output and anode pressure drop under large fluctuations in humidifier temperature, and investigates the mechanism behind this correlation. Chapter 5 summarizes the major findings of this thesis, and suggests potential future work.

## Chapter 2

### EXPERIMENTAL SETUP AND TEST PROCEDURE

#### 2.1 Fuel Cell Components and Design

The objective of this thesis is to measure the net power output from fuel cells employing different combinations of flow fields on the anode and cathode side. A total of four combinations as listed in Table 1.1 were investigated. Accordingly, serpentine and interdigitated flow field plates were designed and fabricated. The flow field channels are 0.1016 cm (0.04 inch) wide  $\times$  0.1016 cm high (0.04 inch)  $\times$  5.0038 cm long (0.5 inch) with a 0.0686 cm land width separating the channels in both flow field plates, as shown in Fig. 2.1. The active area of each flow field is 25 cm<sup>2</sup>. The flow field plates are made of 1.27 cm thick gold-coated aluminum 6061-T6. Other associated components include end plates (2.5 cm thick Al 6061-T6) and current collectors (0.2 cm thick gold plated aluminum).

Each end plate has one 180 W, 10 cm long embedded heater. A thermocouple is bonded to the cathode end plate to control the cell temperature to within  $\pm 2^\circ\text{C}$  of the set value.

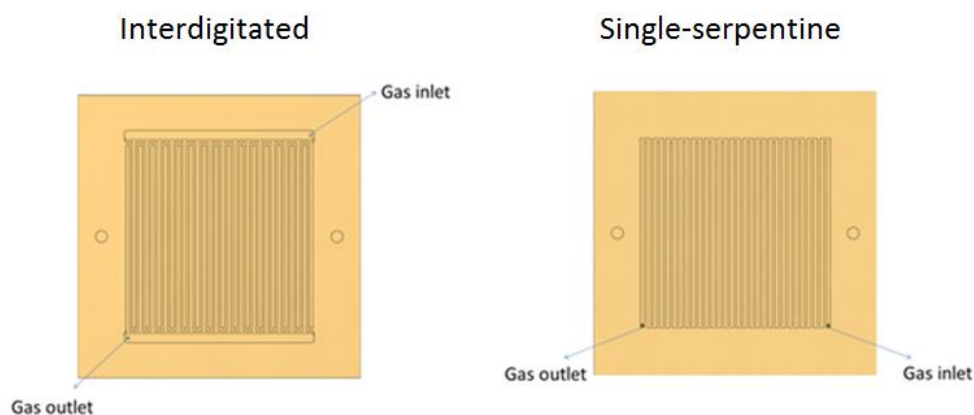


**Figure 2.1 Schematics of interdigitated and single serpentine flow field designs built and tested in this work**

Identical membrane-electrode assemblies (MEAs) were used in all tests, and each was comprised of a 5 cm × 5 cm Nafion NRE212 membrane (50 μm thick) sandwiched between two sheets of catalyst-coated gas diffusion electrodes (GDE) loaded with 0.5 mg/cm<sup>2</sup> Pt (purchased from FuelCellsEtc). The MEAs were fabricated by hot-pressing the Nafion membrane between the two GDEs at 130°C for 2 minutes.

## 2.2 Fuel Cell Test Station

An Arbin fuel cell test stand was used to test the performance of all the flow field combinations as shown in Figs. 2.2 and 2.3. The electronic load, flow rate, temperature, humidity and back pressure were controlled and monitored by the test stand at a sampling rate of 1 Hz. All tests were conducted with constant flow rates. For our baseline operating condition, reactant gases were supplied at 70°C and 100% RH with H<sub>2</sub>/O<sub>2</sub> flow rates of 1/2 slpm, respectively.

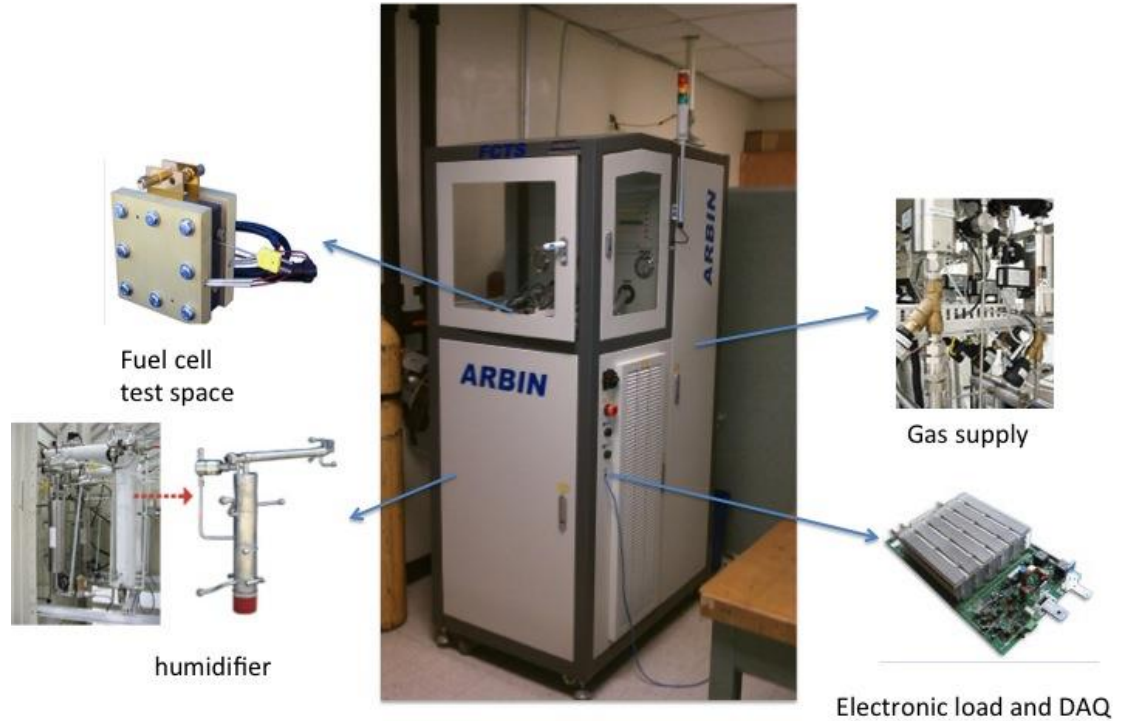
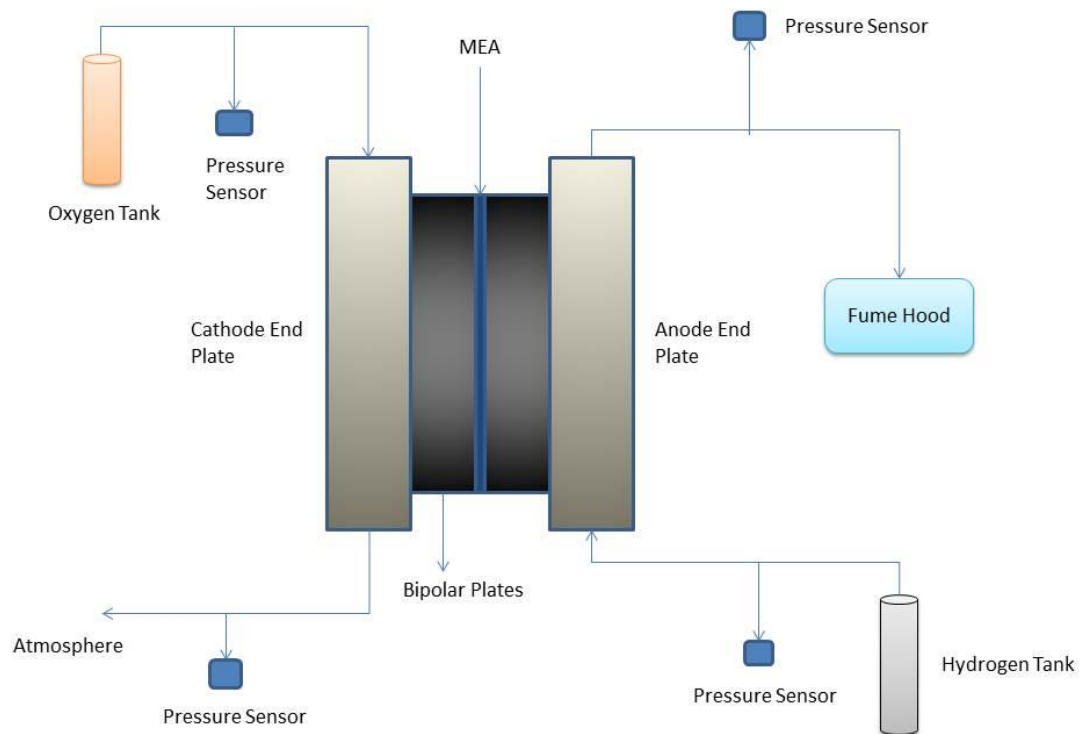


Figure 2.2 Details of the Arbin fuel cell test stand

### 2.3 Pressure Measurement Station

Pressure drop across the cathode and anode sides of the cell are measured using four Honeywell pressure sensors – 24PCDFA6A (14-200 kPa, accuracy 0.5% of the full range) connected to the cell’s gas inlets and outlets, as shown in Fig. 2.3. The data were recorded by a National Instruments DAQ board, which served as an interface between the pressure sensors and a computer with LabVIEW, at a sampling rate of 1 Hz. All pressure sensors were calibrated using a water-filled burette as shown in Fig. 2.4 before testing.



**Figure 2.3 Schematic of connection the four pressure sensors to the cell.**



**Figure 2.4 Use of a water-filled burette to calibrate the pressure sensors using a Labview program**

## **2.4 Test Procedure**

For each fuel cell with different combinations of flow fields as listed in Table 1.1, data were collected from cell tests. Test stand data (voltage, current density, cell temperature, humidifier temperature, reactant gas temperatures, and gas mass flow rates) and pressure differentials across the cathode and anode sides of the cell were recorded simultaneously for each test. Each test run measured current data at a fixed voltage, or voltage data at a fixed current for 30 minutes for the nine different operating conditions listed in Table 1.2. Performance and pressure drop data were plotted separately for each test and presented using the same time line. However, Chapter 4 includes some plots which contain performance data overlaid with pressure drop data to study the correlation between pressure drop and cell performance.

## **2.5 Summary**

This chapter presented materials and dimensions of fuel cell components and schematics of flow fields designs employed in this study. Details of the fuel cell test stand and pressure measurement station used in the tests were also described. Baseline operating conditions were described, as well as the methods used to collect and present fuel cell test stand data and pressure differential data.

## Chapter 3

### RESULTS OF NET POWER WITH DIFFERENT FLOW FIELD COMBINATIONS

#### 3.1 Pressure Drop in Four Flow Fields Combinations

In most previous studies, researchers measured only the gross power from the fuel cell but not the net power. Net power is gross power minus parasitic losses, which are mainly due to the power required to pump air through the cathode flow field. Pumping losses can be estimated by measuring the pressure drop across the flow fields when conducting tests with the Arbin test stands. Experiments were conducted using four flow field combinations as listed in Table 1.1 and cell performance and pressure drops were recorded during testing. Net power was subsequently determined using the pressure drop and cell performance data.

Cell performance and pressure drop behavior were recorded simultaneously after stepping down to a constant voltage 0.6 V from open circuit, and tests were run at standard operating conditions shown in Table 3.1. Current density fluctuated in a small range when the cell was operated at fixed voltage as shown in the following sections. Here, we chose 0.6 V because this is the voltage at which the cell can give a high and steady gross power output. Prior to the test, the cell was operated at OCV for 30 minutes to preclude flooding, and thus the pressure drop and performance data were not influenced by flooding at the beginning of the test. The test duration was set to 30 minutes in order to provide adequate time to observe the occurrence of flooding in the flow channels and any subsequent recovery.

Figure 3.1 shows the anode and cathode pressure differential profile in the four types of cells tested. In the case of the ASCS cell, the average pressure drop was around 28 kPa on the cathode side, and less than 10 kPa on the anode side. For the AICI cell, the average pressure drop is around 12 kPa on the cathode side and 1 kPa on the anode side. These values are reasonable because the gas flow velocities and Reynolds number are much lower in the interdigitated flow field than those in the serpentine flow field. Here, the gas flow velocity is defined at the inlet of each channel, not at the inlet of the bipolar plates. Since the interdigitated flow field contained 16 channels, the cross sectional area available for gas flow will be 16 times higher than the cross sectional area in the single-serpentine channel, so the flow velocity in each interdigitated channel will be proportionally lower [7]. In the case of the AICS cell (Table 1.1), the average pressure drop in the interdigitated flow field (anode) is close to the pressure drop in the anode side of the AICI cell, and the average pressure drop in the ASCS flow field (cathode) is close to that in the cathode side of the ASCS cell. In the case of the ASCI cell (Table 1.1), the average pressure drop in each flow field is also close to that in the corresponding flow field in the ASCS and AICI cells.

In Fig. 3.2, Fig. 3.3, Fig. 3.4 and Fig. 3.5, pressure drop curves in anode and cathode flow fields were given for the four types of cells discharged at standard operating condition for 30 minutes respectively. Fig. 3.2 shows the pressure drop curves in ASCS cell, Fig. 3.3 shows the pressure drop curves in ASCI cell, Fig. 3.4 shows the pressure drop curves in AICS cell and Fig. 3.5 shows the pressure drop curves in AICI cell. It is observed that the pressure drop on the anode side is always lower than that on the cathode side even when the flow fields on both sides are the

same because the anode gas flow rate is only a half of the cathode flow rate. Second, it is observed that the pressure drop sometimes increases after the fuel cell had been in operation for a while, which is a sign of liquid water accumulation in channels. Liquid water accumulation in the form of drops and slugs can block the gas channel, reducing the cross sectional flow area of the gas channels, leading to a higher pressure drop according to Darcy's law. Third, water is produced at the cathode, so liquid water is more likely to form on the cathode side in the cells; this could also contribute to the higher pressure drop observed on the cathode side for each flow field combination.

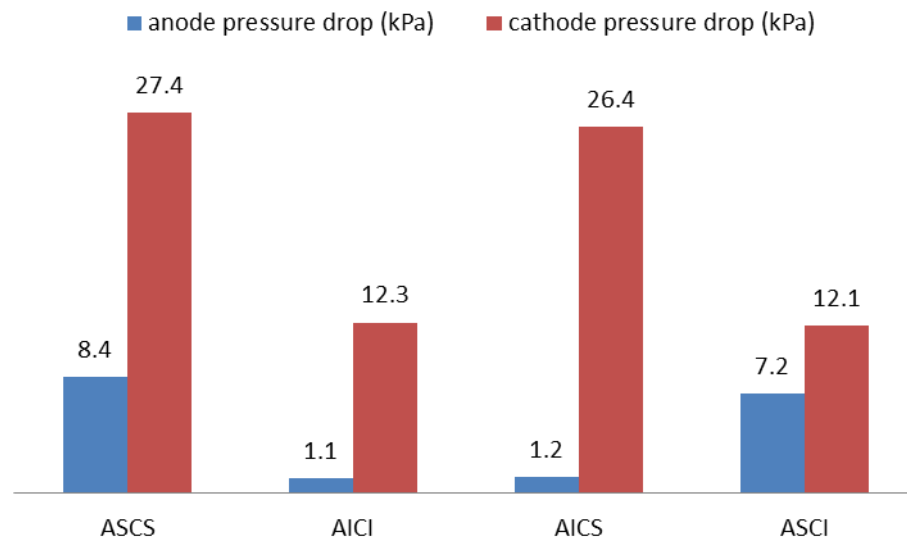


**Figure 3.1 Average pressure drop in each flow field during discharge at 0.6 V under standard operating conditions for 30 minutes**

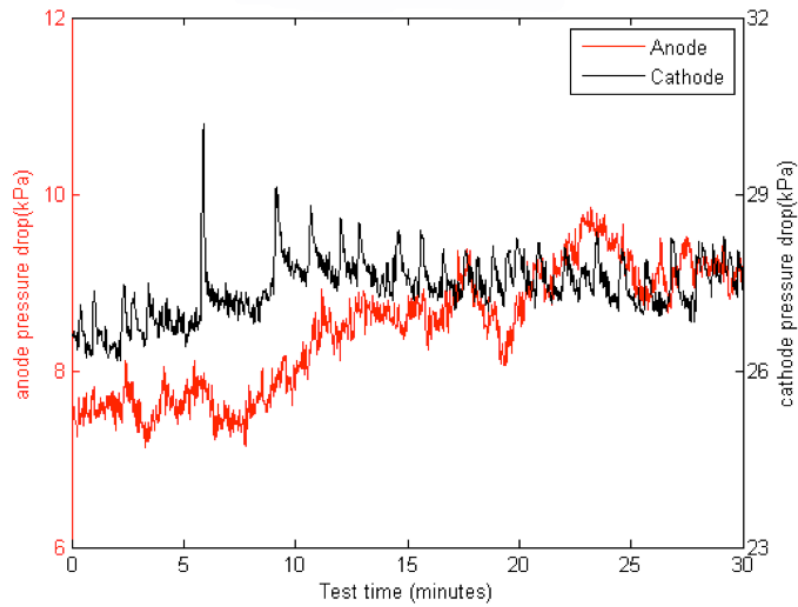


**Figure 3.2 Pressure drop profile in ASCS flow field during discharge at 0.6 V under standard operating conditions for 30 minutes**

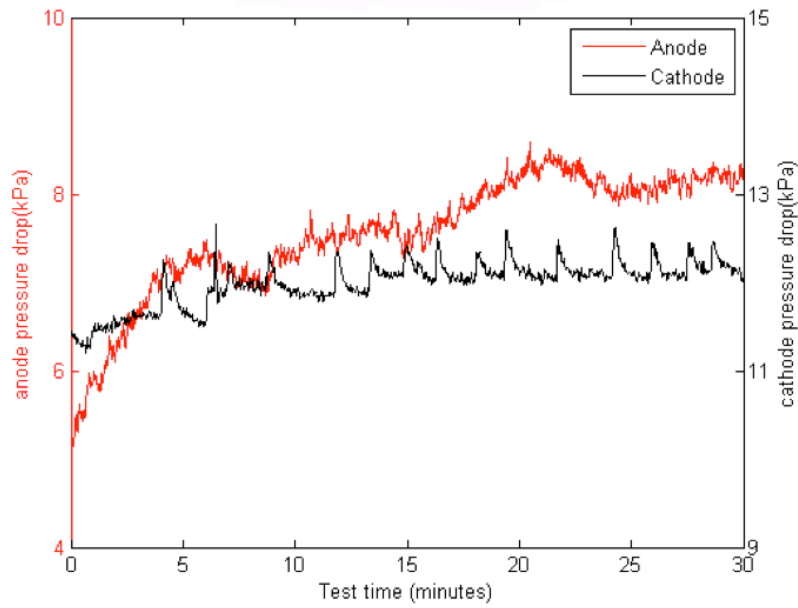


**Figure 3.3 Pressure drop profile in ASCI flow field during discharge at 0.6 V under standard operating conditions for 30 minutes**

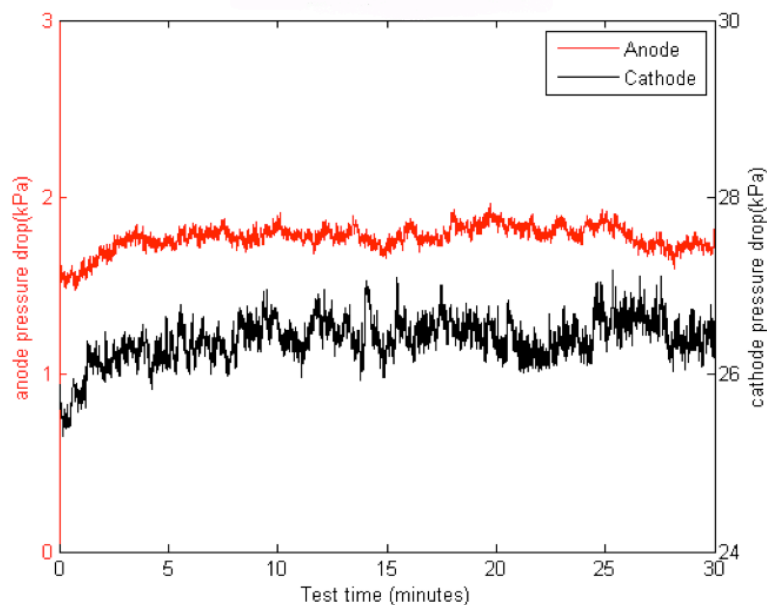


**Figure 3.4 Pressure drop profile in AICS flow field during discharge at 0.6 V under standard operating conditions for 30 minutes**

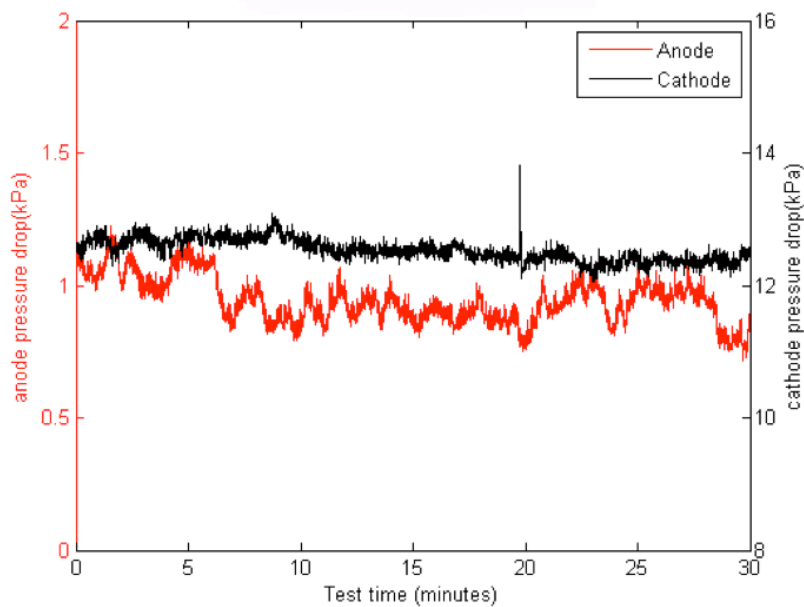


**Figure 3.5 Pressure drop profile in AICI flow field during discharge at 0.6 V under standard operating conditions for 30 minutes**

### 3.2 Effect of Operating Conditions on Pressure Drop

As stated in Section 1.3, besides the standard operating conditions, eight additional operating conditions listed in Table 1.2 were applied to each cell with the four different flow field combinations. The influence of oxygen flow rate, cell temperature, relative humidity, and current density on pressure drop is presented next.

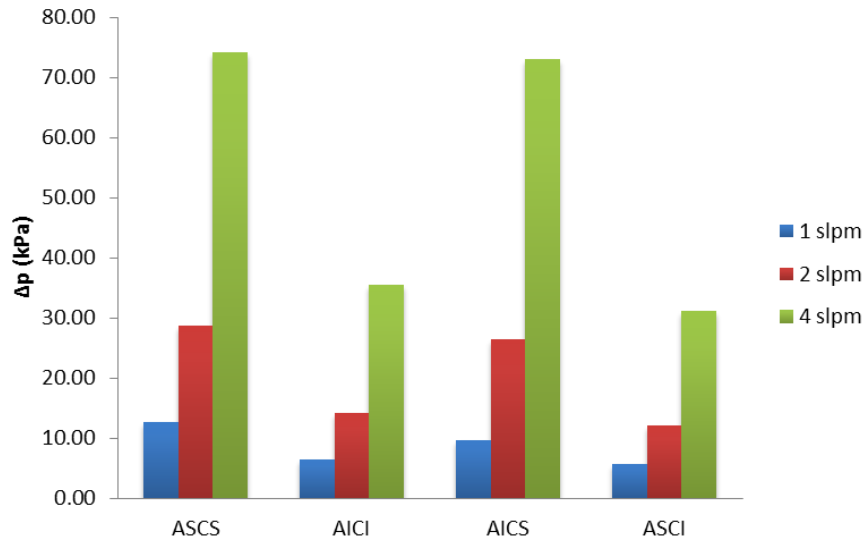
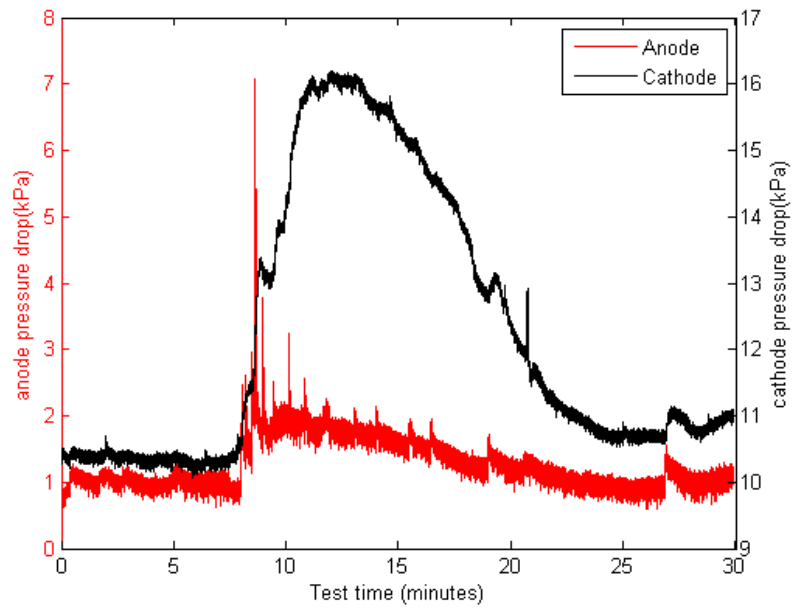
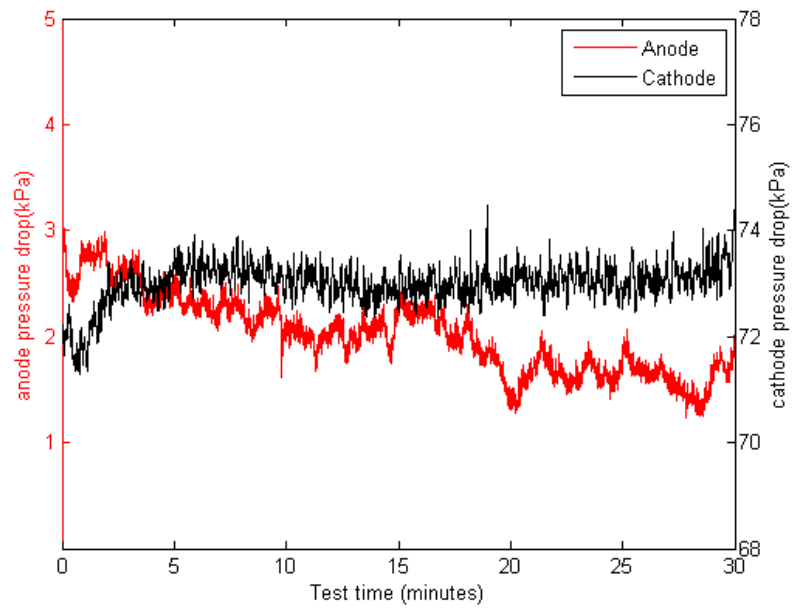


Figure 3.6 Pressure drop in AICS cell at oxygen flow rates of 1, 2, and 4 slpm

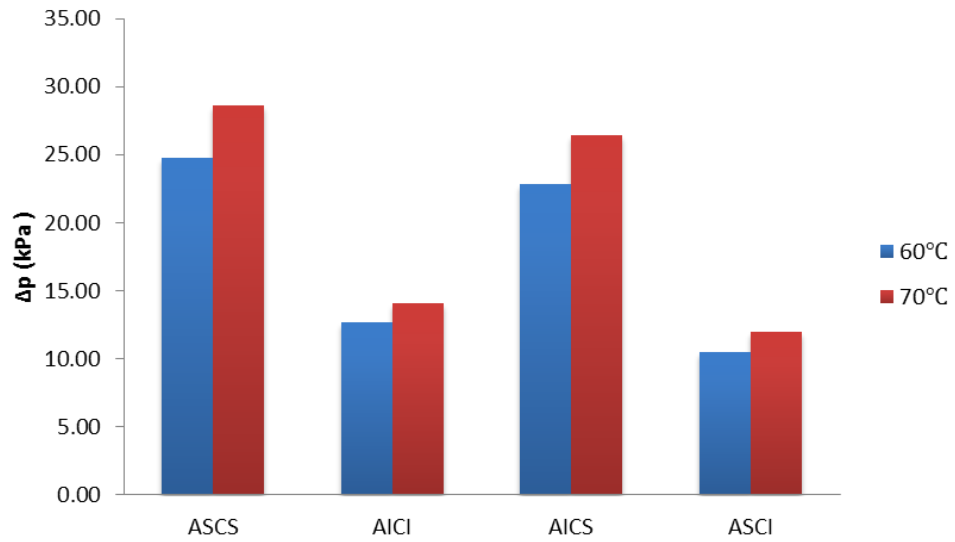
Figure 3.6 shows the influence of oxygen flow rate on the cathode pressure drop. Here, the pressure drop was monitored at 1 Hz, and the average pressure drop was calculated over the full test duration of 30 minutes. In each flow field, we see that cathode pressure drop is nearly proportional to the oxygen mass flow rate, which is consistent with Eq.1.3. Figures 3.7 and 3.8 show the pressure drop curves for the AICS cell at different oxygen flow rates. We can see that the average cathode pressure drop is about 14kPa in when oxygen flow rate is 1 slpm and about 73kPa when oxygen flow rate is 4 slpm, which indicates that oxygen flow rate has a major impact on cathode pressure drop in flow fields.



**Figure 3.7 Pressure drop profile in AICS flow field during discharge at 0.6V and oxygen flow rate 1 slpm for 30 minutes**

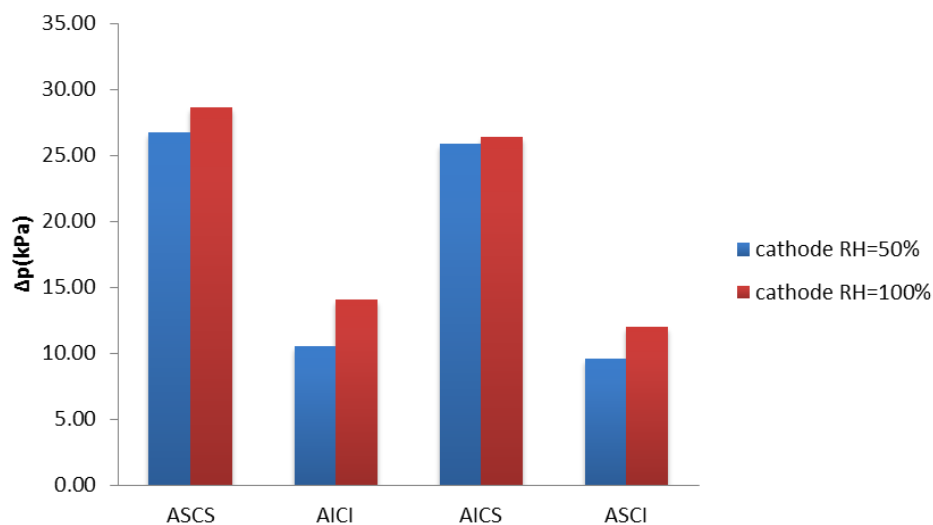


**Figure 3.8 Pressure drop profile in AICS flow field during discharge at 0.6V and oxygen flow rate of 4 slpm for 30 minutes**



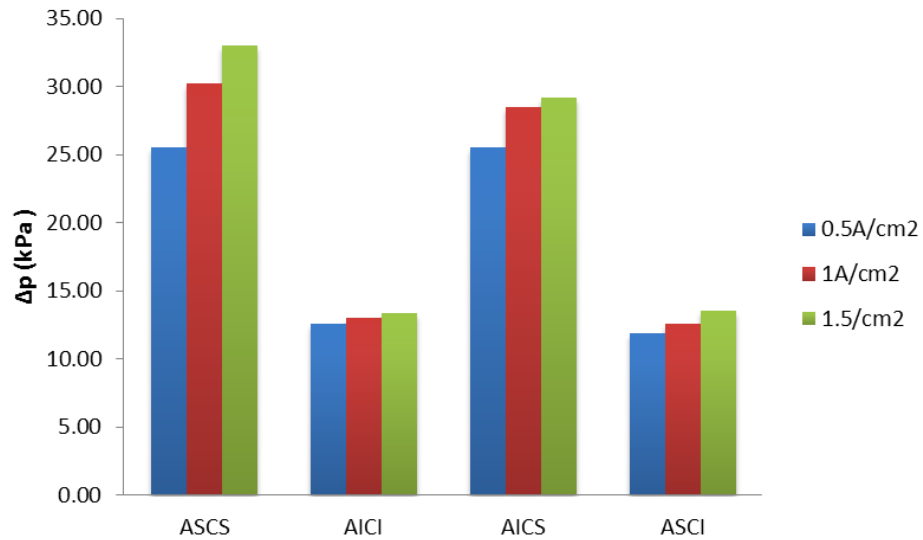
**Figure 3.9 Average pressure drop in each flow field during discharge at 0.6 V for 30 minutes at 60°C and 70°C**

Figure 3.9 shows that the pressure drop reduces slightly when the temperature is reduced to 60°C. From the performance profiles in the following sections, we will see that the current density for 0.6 V at 60°C is lower than that at 70°C. A lower current density means that the reaction rate is lower, implying a lower water production rate and a lower propensity for water flooding. Hence, the pressure drop can be expected to reduce when the current density decreases.



**Figure 3.10 Average pressure drop in each flow field during discharge at 0.6 V for 30 minutes at 50% cathode RH 100% cathode RH**

Figure 3.10 compares the cathode pressure drop for cathode RH levels of 50% and 100%. The cathode pressure drop at 50% RH is always lower than that for 100% RH. This is to be expected because a lower RH decreases the propensity for flooding. Moreover, lower RH in the inlet gas flow may cause membrane dryout leading to low protonic conductivity of membrane, and thus higher ohmic losses. For a fixed operating voltage, higher ohmic losses will result in a reduced current density, which means a lower reaction rate. As explained above, a lower reaction rate implies water production rates, leading to a smaller pressure drop in the cathode gas channels.



**Figure 3.11 Average pressure drop in each flow field during discharge at 0.5, 1, and 1.5 A/cm<sup>2</sup> for 30 minutes**

Next, the fuel cell was operated at a fixed current density (0.5, 1, and 1.5 A/cm<sup>2</sup>) instead of a fixed voltage for 30 minutes to study the effect of current density on pressure drop and net power in the different flow field combinations. For a fixed current density, the cell voltage fluctuates slightly as shown in the performance curves. As shown in Fig. 3.11, the pressure drop increases with current density for the same reasons as presented earlier.

### 3.3 Parasitic Power Loss Calculation and Net Power

In the preceding sections, the measured voltage and current density data provided the gross power produced by the cell. In order to obtain the net power, the parasitic power losses must be subtracted from the gross power. Usually, compressor power is the major contributor to the parasitic losses in a fuel cell system, so we assumed that the entire parasitic loss can be equated to the power consumed by the compressor to drive air through the cathode flow field [11]. Anode pumping losses are

ignored since in most applications the hydrogen is supplied from a high pressure tank without the need of a pump. Compressor power is evaluated as follows [5]:

$$P_{\text{compressor}} = c_p \frac{T_1}{\eta_m \eta_c} \dot{m} \left[ \left( \frac{p_2}{p_1} \right)^{\frac{\gamma-1}{\gamma}} - 1 \right] \quad 3.1$$

where  $T_1$  is the inlet temperature (in K),  $c_p$  is the specific heat capacity at constant pressure (in J/kg-K),  $p_1$  is atmosphere pressure,  $p_2$  is inlet pressure,  $\dot{m}$  is the gas mass flow rate (in kg/s),  $\eta_c$  is the compressor efficiency,  $\eta_m$  is the motor efficiency, and  $\gamma$  is the ratio of specific heat capacities,  $c_p/c_v$ . Here we use values for oxygen at standard conditions:  $p_1 = 100$  kPa,  $T_1 = 293$  K,  $c_p = 0.918$  kJ/kg-K,  $\gamma = 1.40$ , and typical values for efficiencies:  $\eta_c = 0.7$  and  $\eta_m = 0.9$ . An oxygen flow rate of 2 slpm at  $1.33 \text{ kg/m}^3$  gives a mass flow rate of  $4.43 \times 10^{-5}$  kg/s [5].

Equation 3.1 was used to calculate the compressor power by inserting the measured value of  $p_2$  for each cell discharging at either constant voltage or constant current density for 30 minutes. The net power for each test was obtained as the difference between the measured gross power output and the calculated parasitic power loss.

Three tests were conducted for each operating condition and we report the average value for the measured performance and pressure drop. We also calculated the standard deviation and examined the confidence level from an ANOVA analysis. If the standard deviation exceeds the difference between the mean values of net power output, then it cannot be guaranteed that the differences within the same test group can be ignored compared to the differences across different test groups. As shown in Fig. 3.12, the ASCI fuel cell has the highest net power output for the four flow field combinations at standard operating conditions due to the lower pressure drop on the cathode side, and hence lower parasitic loss. The values of standard deviation

presented in Fig. 3.13 show that the variations in net power within the same test group are much too small to affect our conclusions.

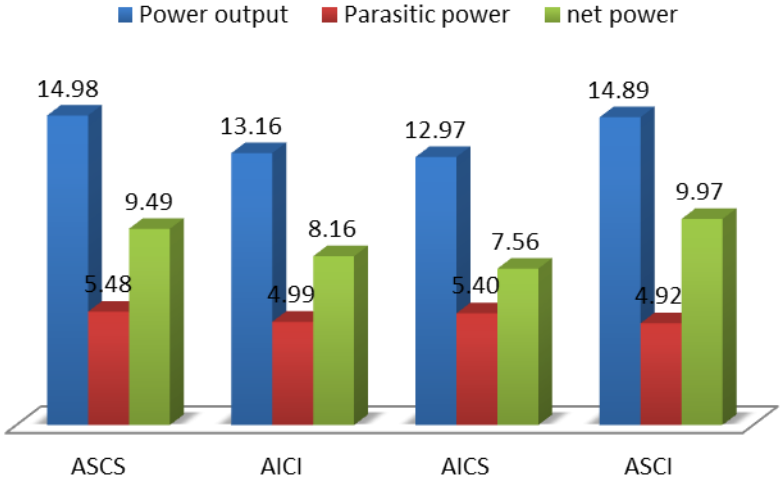


**Figure 3.12 Average total power output, parasitic power loss and net power in each cell; cells were operated at standard operating conditions for 30 minutes at 0.6 V. Net power is defined as the difference between total power output and parasitic power loss. The quoted values are in watts.**

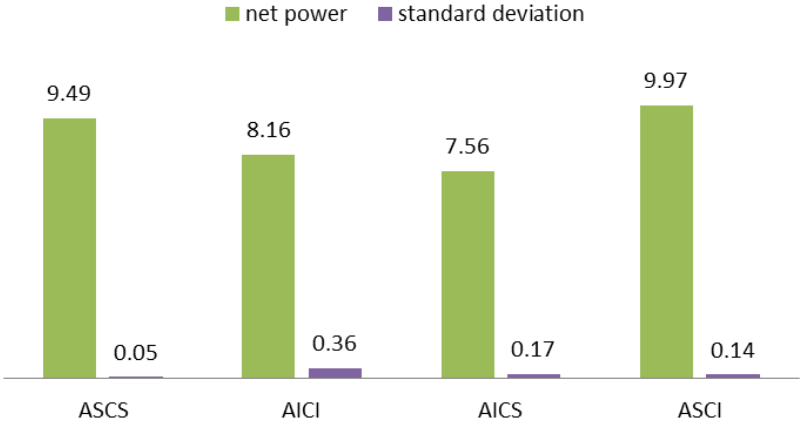


**Figure 3.13 Average net power in each cell; cells were operated at standard operating condition for 30 minutes at 0.6 V. Standard deviations were calculated from three tests for total power output and parasitic loss to assess variations in test results within the same group of experiments.**

Since we have three tests for each flow field at the same operating condition, to ensure that the difference in net power of different cells is significant and our

conclusions are robust, we conducted an ANOVA test for four flow field combinations in each test group.

Since we have three tests for each flow field at the same operating condition, to ensure that the difference in net power of different cells is significant and our conclusions are robust, we conducted an ANOVA test for two groups of test results corresponding to the flow fields exhibiting the better results: the ASCI and ASCS cells. Here we set the confidence limit as 95%; so when the p-value of the ANOVA test is smaller than 0.05, the null hypothesis (the mean values of data groups are equal) will be rejected, and we can conclude that there is a significant difference between groups. Conversely, when the p-value of the ANOVA test exceeds 0.05, we cannot conclude that there is a significant difference between groups. The p-values of the ANOVA tests for each case are summarized in Table 3.1. All the p-values calculated by the ANOVA analysis for all the test groups were smaller than 0.05 which confirms that our conclusions regarding which flow field has the better net power output are robust.

<i>Operating condition</i>	<i>p-value</i>
0.6 V	0.0001
0.5 A/cm <sup>2</sup>	0.0016
1 A/cm <sup>2</sup>	0.0018
1.5 A/cm <sup>2</sup>	0.002
anode RH 50%	0.016
cathode RH 50%	0.0003
oxygen flow rate 1 slpm	0.018
oxygen flow rate 4 slpm	3.12E-5
60°C	0.001

**Table 3.1 P-values for the net power results for the ASCI and ASCS flow fields at each specific operating condition**

### 3.4 Power Efficiency Discussion

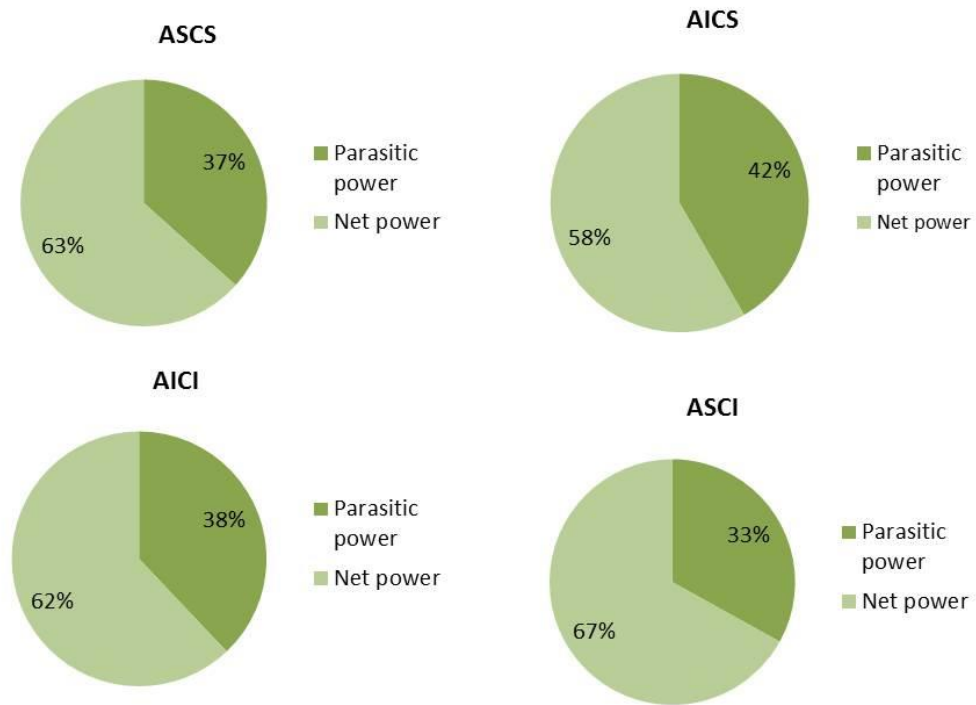


Figure 3.14 Power efficiency of each flow field at standard operation conditions at 0.6 V

An example of energy efficiency evaluation is shown in Fig. 3.14 by calculating the fraction of parasitic losses for all cell combinations discharging at 0.6 V under standard operating conditions. We noticed that parasitic losses can be as large 42% of the total power output. The energy efficiency of the ASCI cell is the highest of all the four cells, whereas the AICS cell has the lowest energy efficiency.

### 3.5 Effect of Operating Conditions on Net Power Output and Power Efficiency

One specific operating parameter is changed at a time to investigate the net power output of four cells under various operating conditions. As described earlier, the influence of relative humidity on each side, temperature, current density, and oxygen

flow rate on the net power of each cell was investigated, and three tests were conducted for each condition to ensure repeatability.

From Eq.3.1, we see that parasitic losses should double if we double the oxygen flow rate. However, the performance of the fuel cell will also improve when the oxygen flow rate increases because of lower concentration losses. Performance and pressure drop were measured for each cell, and the net power was calculated and compared in Fig. 3.15. As shown, the ASCI cell has the best net power output among the four cells, and the difference between it and the other cells exceeds the calculated standard deviations. It can also be seen that the AICI cell exhibits a better net power output than the ASCS cell because of the large parasitic losses experienced by the ASCS cell at large gas flow rates.

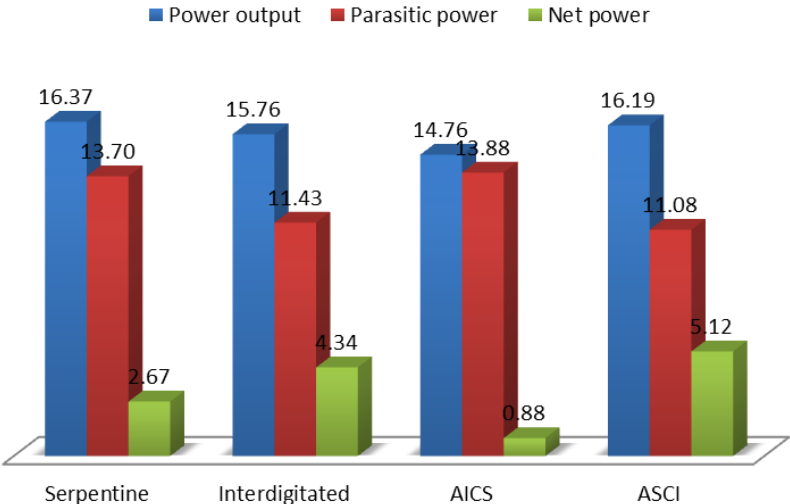


**Figure 3.15 Average total power output, parasitic power loss and net power in each cell; oxygen flow rate was 4 slpm and other conditions remain the same. Cells were operated for 30 minutes at 0.6 V.**

Energy efficiency at high oxygen flow rates were also calculated for the four cells. From Fig. 3.16, we see that the energy efficiency at a high oxygen flow rate (4 slpm) is much lower than that at the standard oxygen flow rate (2 slpm). In particular,

with the serpentine flow field on the cathode side (serpentine and AICS cells), the parasitic losses exceed 80% of the gross power! Current and voltage curves of the ASCI cell at an oxygen flow rate of 4 slpm are shown in Fig. 3.17. In Fig. 3.17 we can see that the current density is stable to  $1.1\text{A}/\text{cm}^2$  at constant voltage  $0.6\text{V}$ .

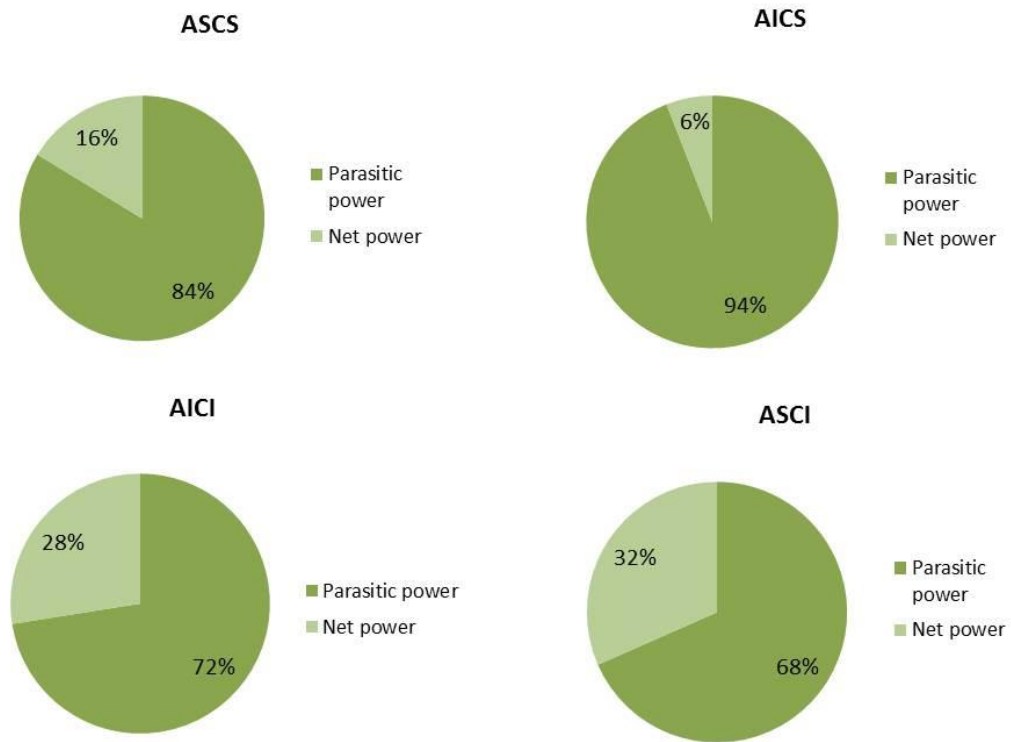
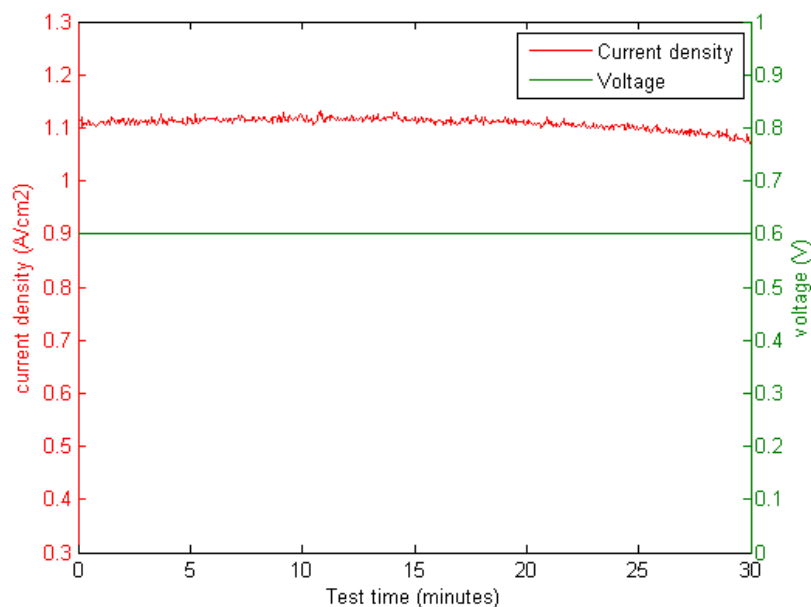


Figure 3.16 Power efficiency of each flow field at oxygen flow rate of 4 slpm at 0.6 V



**Figure 3.17 Current density and voltage profile of ASCI cell during discharge at 0.6V and oxygen flow rate of 4 slpm for 30 minutes**

The net power of the four cells at the low oxygen flow rate of 1 slpm is shown in Fig. 3.18. We note that the gross power output for each cell drops significantly compared with the gross power output at high oxygen flow rates due to increased mass transport losses; however, the parasitic loss at the low gas flow rate is also much lower. Therefore, the net power at 1 slpm oxygen flow rate is still higher than the net power at 4 slpm because of the large parasitic losses at this highest oxygen flow rate; however, it is not better than the net power at the oxygen flow rate of 2 slpm. From the above comparison we can see that there is a trade-off between high gross performance and high power losses when the oxygen flow rate is changed. We also see that the ASCI cell still has the best net power amongst the four cells; however, the difference of the net power between cells is much smaller, and is probably not significant if we take the standard deviation into consideration. According to the p-values in Table 3.1

for this test group, there is still a significant difference between the net power results of different cells since the p-value is smaller than 0.05.

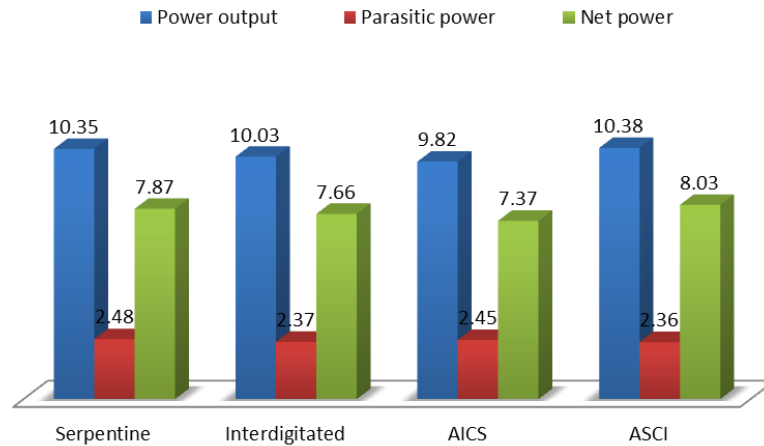


**Figure 3.18 Average total power output, parasitic power loss and net power in each cell; oxygen flow rate was 1 slpm and other conditions remain the same. Cells were operated for 30 minutes at 0.6 V.**

Figure 3.19 shows the energy efficiency of each cell at the oxygen flow rate of 1 slpm. Compared with Fig. 3.16 it is clear that the energy efficiency at this lowest oxygen flow rate is higher, about 75% for each cell. This could be easily understood through Eq.3.1 that a low gas flow rate should result in a small parasitic power loss. Current density and voltage curves of the ASCI cell at an oxygen flow rate of 1 slpm are shown in Fig. 3.20. In Fig.3.20 we see that current density is steady around  $0.71\text{A}/\text{cm}^2$ , which is much smaller than it in Fig.3.17 since lower oxygen flow rate can affect reaction rate at the electrodes.

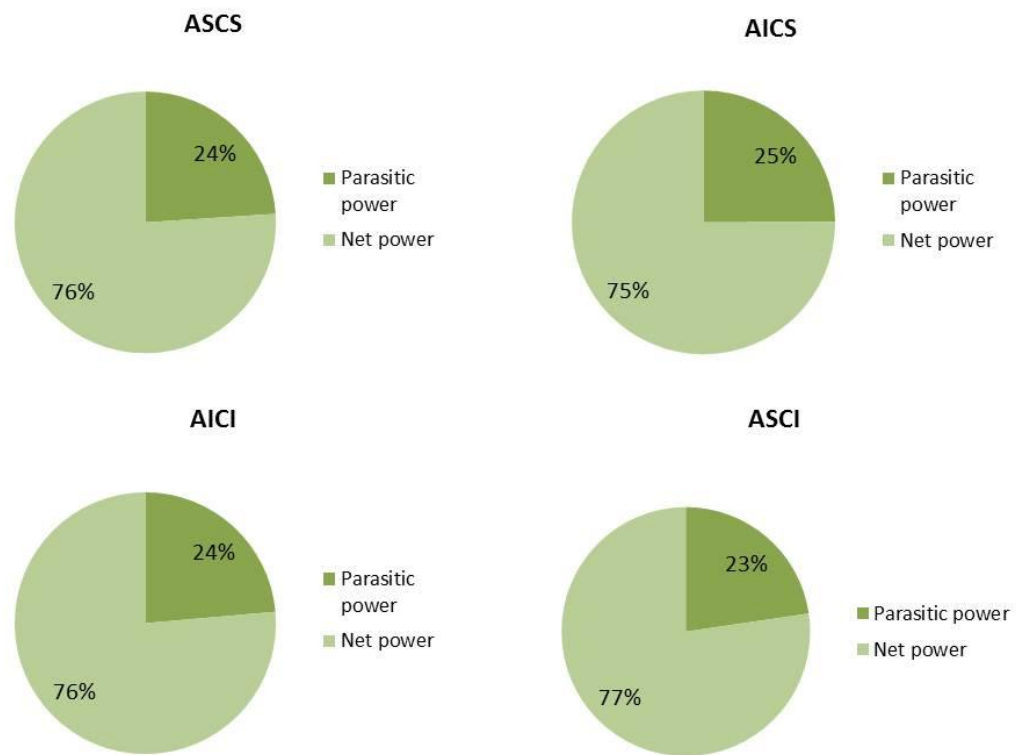


Figure 3.19 Power efficiency of each flow field at oxygen flow rate of 1 slpm at 0.6 V

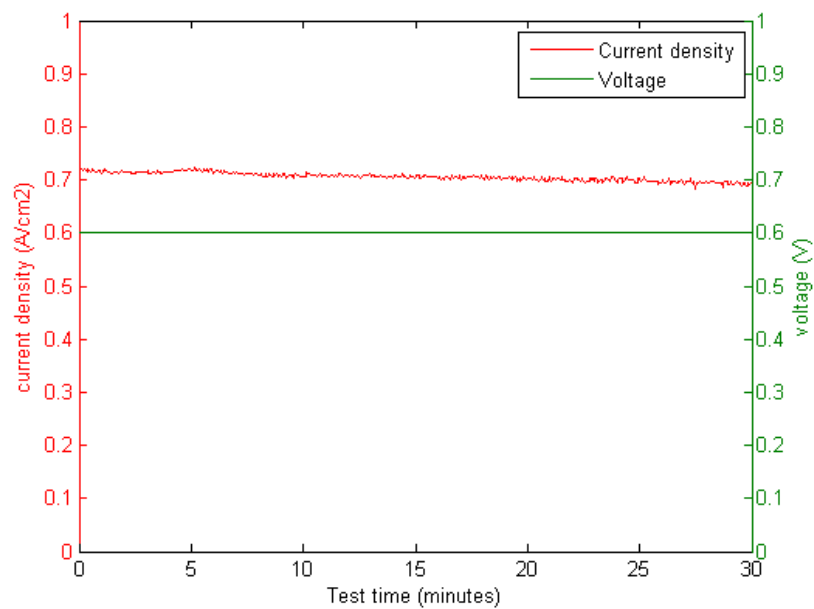


Figure 3.20 Current density and voltage profile of ASCI cell during discharge at 0.6V and oxygen flow rate of 1 slpm for 30 minutes

The influence of temperature on each cell's performance and net power is shown in Fig. 3.21. We see that the gross performance of all four cells at 60°C is lower than that at 70°C, and the parasitic loss is also lower because of the lower pressure drop. The ASCI cell has the best net power among the four cells.

Since in fuel cell test, size of cell has a large impact on gas consumption and power output, we will discuss how net power will change when size of cell changes. First we give the calculation of power output and oxygen usage in a single cell:

$$P = V \times I \quad 3.2$$

$$O_2 = 8.29 \times 10^{-8} \times \frac{P}{V} \text{kg s}^{-1} \quad 3.3$$

We assume the size of cell doubled, so it would be 50cm<sup>2</sup>. Since current I is proportional to cell size, according to Eq. 3.2 and Eq. 3.3, power output and oxygen usage will both double. From Eq.3.1 we know that parasitic power loss is proportional to oxygen mass flow rate, which indicates that it will also be proportional to cell size. However, pressure drop will also increase when oxygen flow rate doubled; and it is proportional to the square of oxygen flow rate. So in total parasitic power loss will be more than the double of the cell size. So when cell size doubled, net power output would be much smaller than the twice of the original value, and ASCI cell should still be better than ASCS cell under this situation.

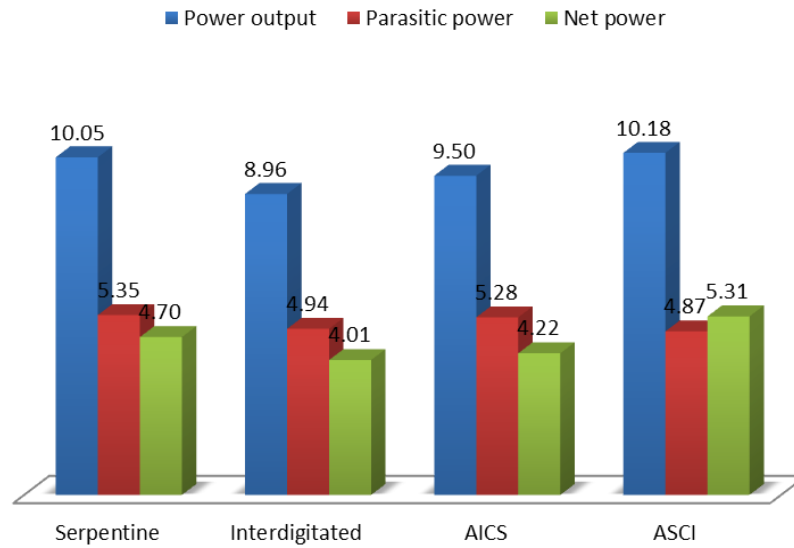


**Figure 3.21 Average total power output, parasitic power loss and net power in each cell; cell temperature was 60°C and other conditions remain the same. Cells were operated for 30 minutes at 0.6 V.**

From Fig. 3.22, we find that the average energy efficiency of the cells at 60°C is around 50% which is lower than the average energy efficiency at the standard operating condition (70°C). It seems that the lower power output at low temperature has a larger influence on energy efficiency than the lower parasitic loss. Current and voltage curves of the ASCI cell at 60°C are shown in Fig. 3.23. In Fig. 3.23 we can see that the current density is steady around 0.68A/cm<sup>2</sup> at constant voltage 0.6V.

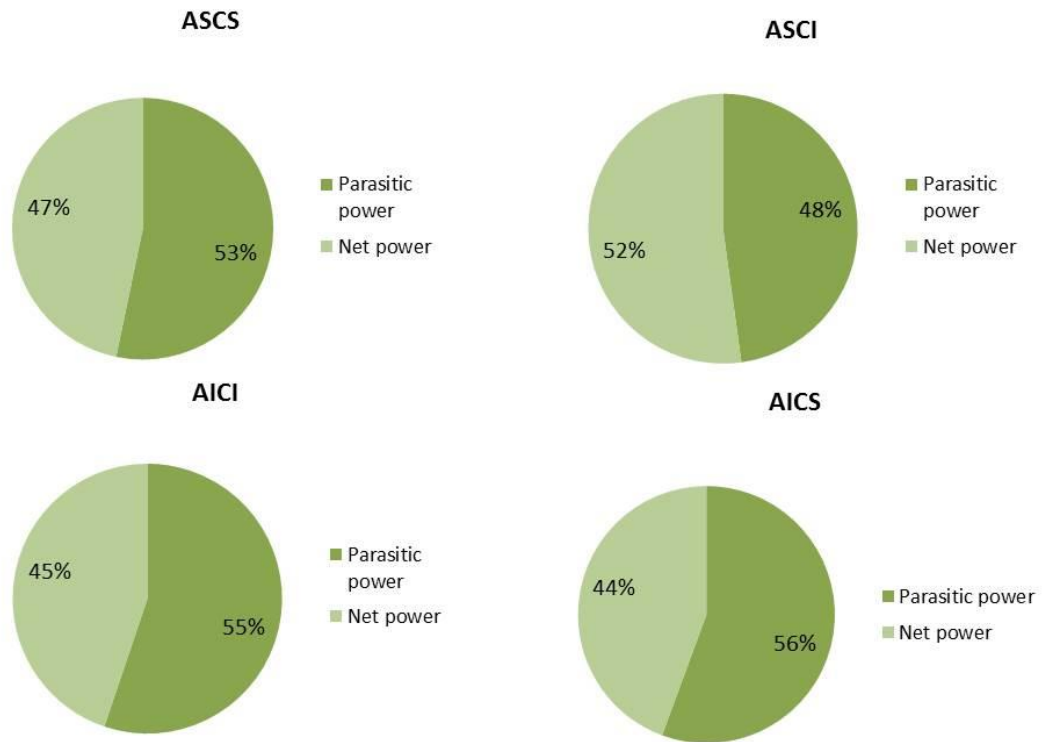


Figure 3.22 Power efficiency of each flow field at cell temperature of 60°C and 0.6 V

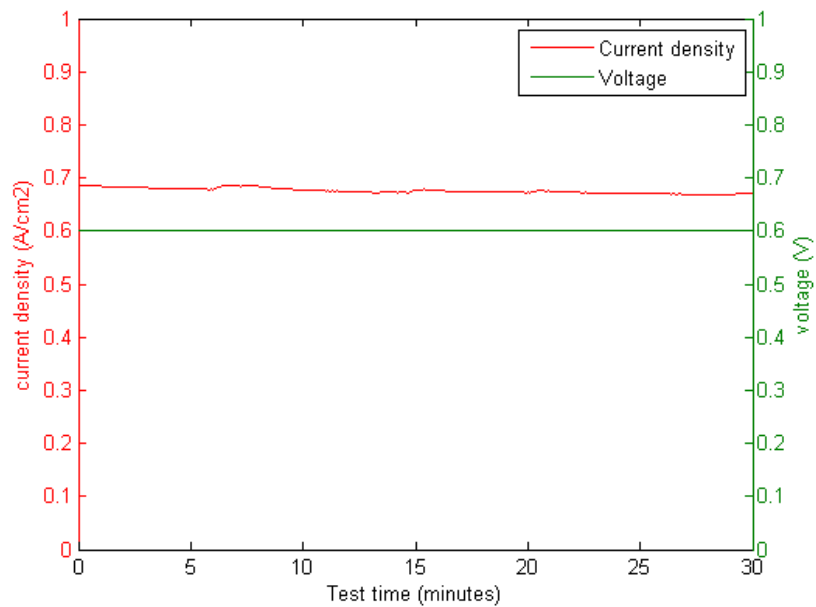
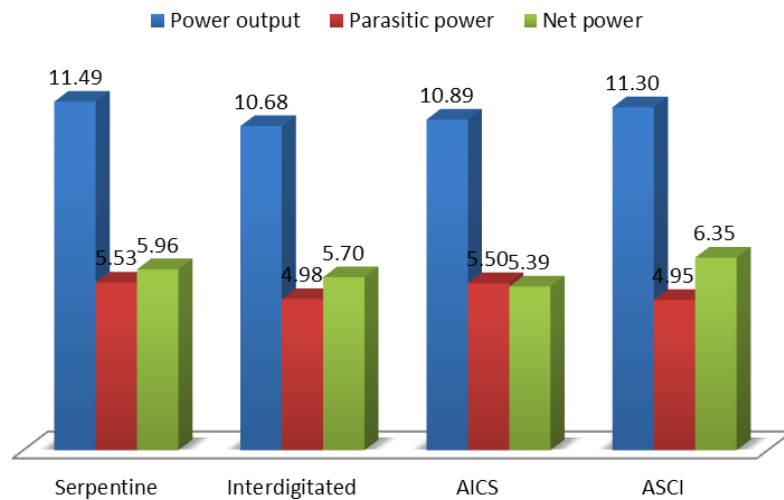


Figure 3.23 Current density and voltage profile of ASCI cell during discharge at 0.6V and 60°C for 30 minutes

From Figs. 3.24 and 3.25, we see that at 50% RH, either on the anode or the cathode side, all the cells show lower performance than at 100% RH on both sides, while also showing lower parasitic losses. The values of net power for each cell in the two cases are very close. In Fig. 3.26 and Fig. 3.27 we see that the energy efficiency of each cell is between 50-60%, which is higher than the fully humidified case. The low parasitic power loss at 50% RH has a larger influence on energy efficiency than the lower gross power output. In both cases, the ASCI cell has the best net power output of the four cells. Current and voltage curves of the ASCI cell for both cases are shown in Fig. 3.28 and Fig. 3.29. In Fig. 3.28 we see that current density fluctuates around  $0.75\text{A}/\text{cm}^2$  when anode relative humidity is 50%, and Fig. 3.29 shows that current density is around  $0.74\text{A}/\text{cm}^2$  when cathode relative humidity is 50%.



**Figure 3.24** Average total power output, parasitic power loss and net power in each cell; anode RH was 50% and other conditions remain the same. Cells were operated for 30 minutes at 0.6 V

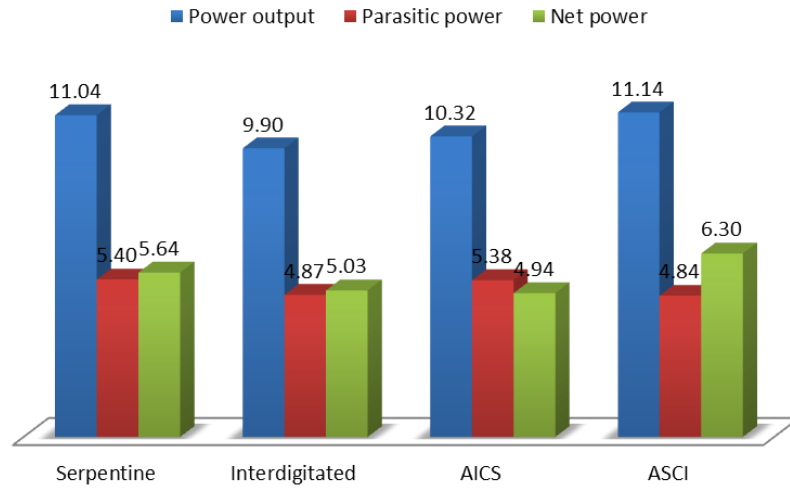


Figure 3.25 Average total power output, parasitic power loss and net power in each cell; cathode RH was 50% and other conditions remain the same. Cells were operated for 30 minutes at 0.6 V.

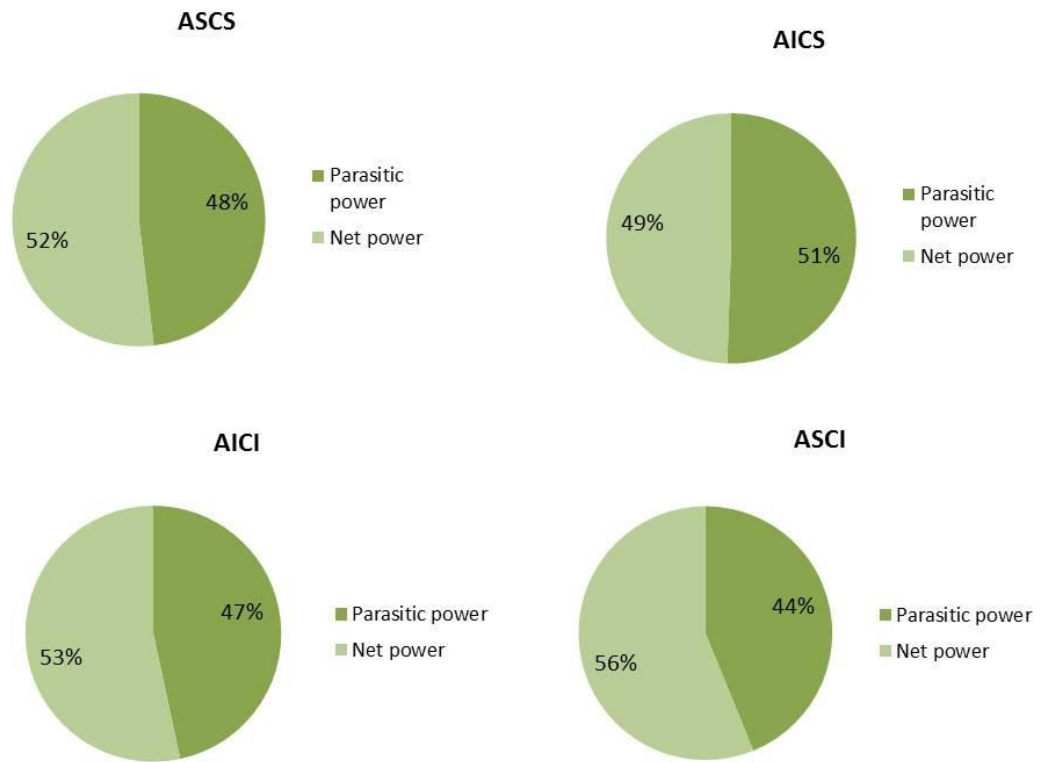


Figure 3.26 Power efficiency of each flow field at anode RH 50% and 0.6 V

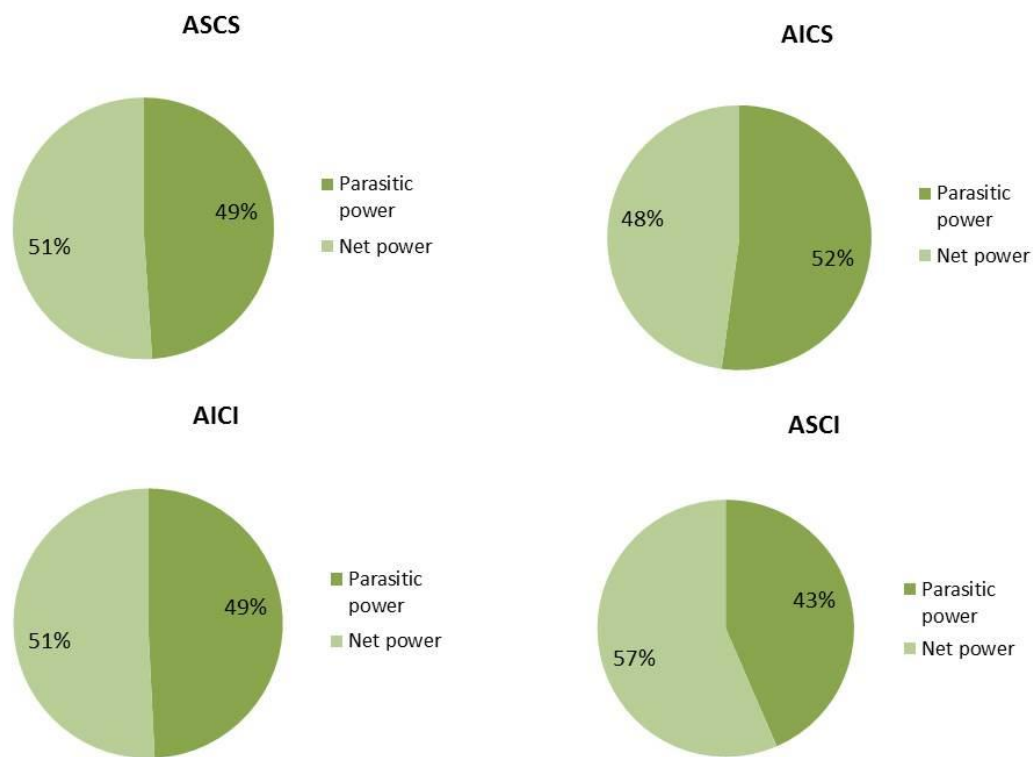


Figure 3.27 Power efficiency of each flow field at cathode RH 50% and 0.6 V

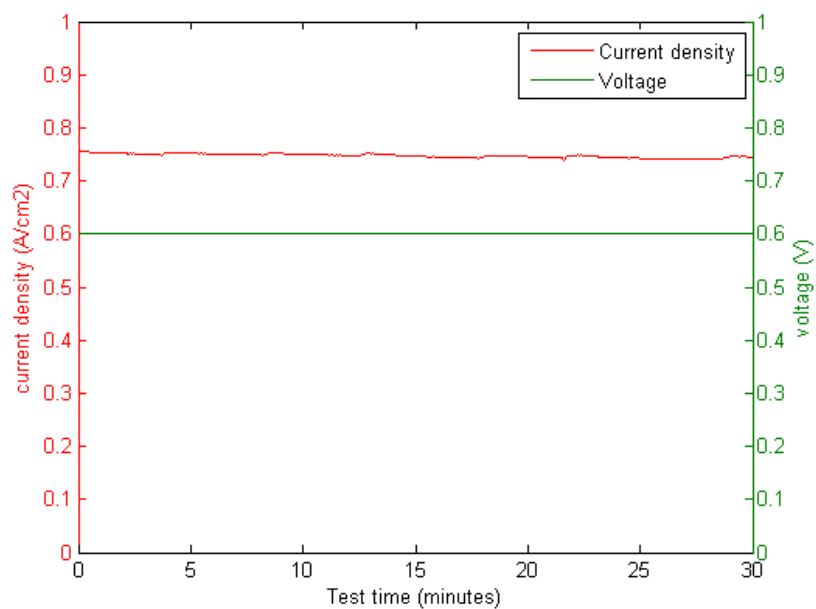
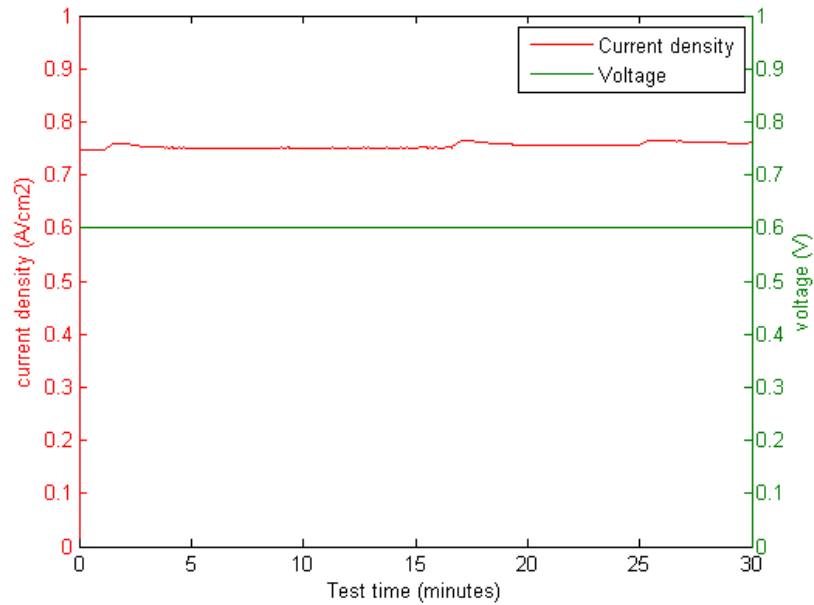


Figure 3.28 Current density and voltage profile of ASCI cell during discharge at 0.6V and anode RH 50% for 30 minutes



**Figure 3.29 Current density and voltage profile of ASCI cell during discharge at 0.6V at cathode RH 50% for 30 minutes**

As shown before, the current density also affects the pressure drop in the flow field, which means that it can influence the parasitic losses. The gross power output of the fuel cell also depends strongly on the current density. Here, we operated each fuel cell at a constant current density of 0.5, 1.0, and 1.5 A/cm<sup>2</sup> for 30 minutes and calculated the net power based on the performance and pressure drop measurements. As for all the above cases, three tests were run for each current density value, and the average power output and parasitic loss was used to calculate the net power. From the Fig. 3.30, Fig. 3.31 and Fig. 3.32, it is easy to conclude that the parasitic losses hardly change with current density; on the other hand, the power output at 1.5 A/cm<sup>2</sup> is around twice the power output at 0.5 A/cm<sup>2</sup>. Therefore, the net power at 1.5 A/cm<sup>2</sup> is much higher than that at low current densities. Observation of Fig. 3.33, Fig. 3.34 and Fig. 3.35 shows that the ASCI cell gives the best net power performance irrespective

of current density. Energy efficiency also increases with current density. At 0.5 A/cm<sup>2</sup>, the net power is only around 40% of the total power output in each cell; at 1.5 A/cm<sup>2</sup>, the energy efficiency is around 70% for each cell. Fig. 3.36 shows that voltage is steady around 0.71V when current density is constant at 0.5A/cm<sup>2</sup>; Fig. 3.37 shows that voltage stays around 0.61V while current density is 1A/cm<sup>2</sup>; Fig. 3.38 shows that voltage is around 0.48V when current density is 1.5A/cm<sup>2</sup>.

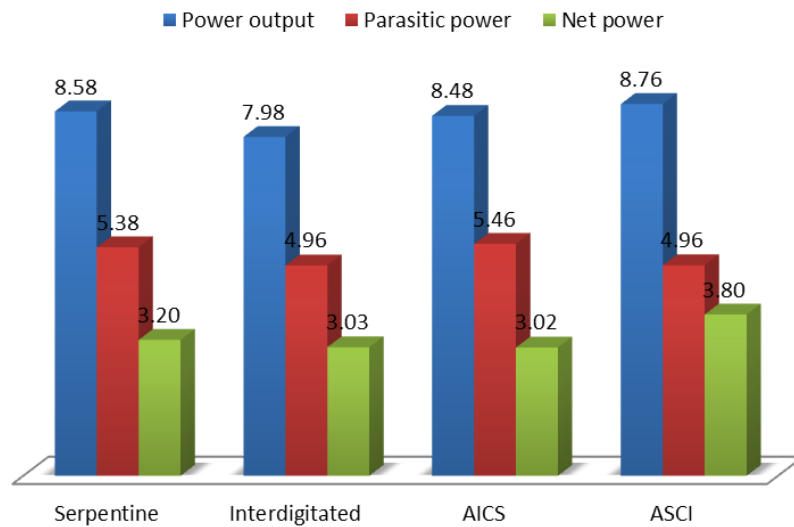


**Figure 3.30 Average total power output, parasitic power loss and net power in each cell; cells were operated at standard operating conditions for 30 minutes at 0.5 A/cm<sup>2</sup>**

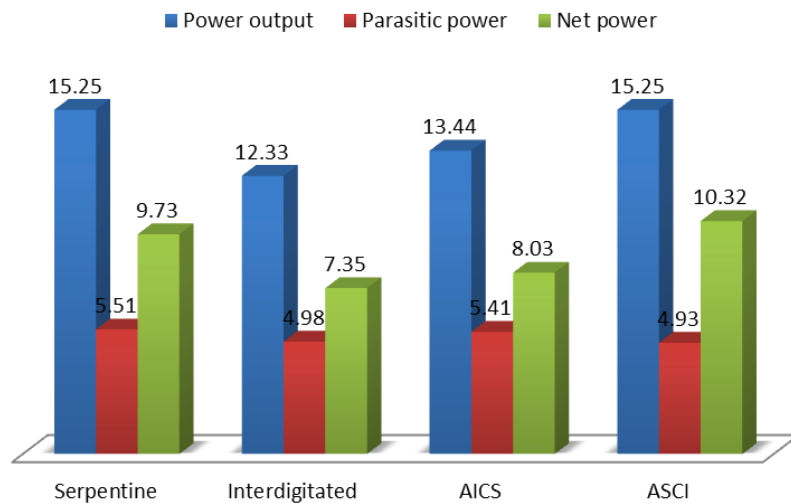


Figure 3.31 Average total power output, parasitic power loss and net power in each cell; cells were operated at standard operation condition for 30 minutes discharging at  $1\text{A}/\text{cm}^2$ .

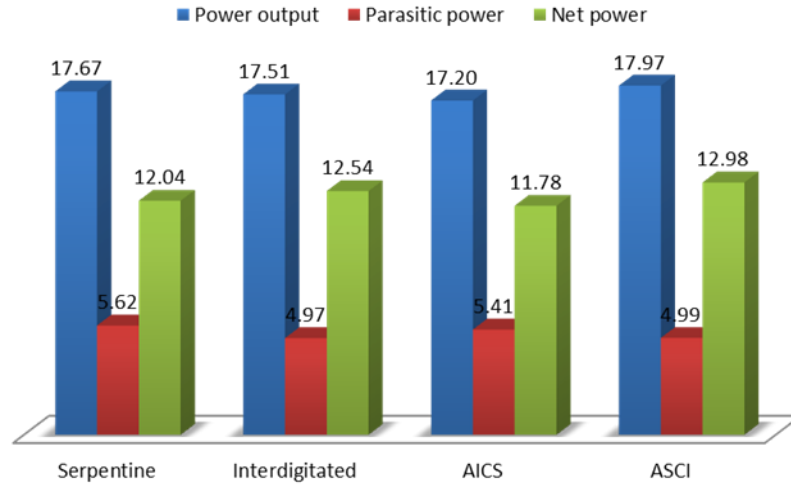


Figure 3.32 Average total power output, parasitic power loss and net power in each cell; cells were operated at standard operating conditions for 30 minutes at  $1.5\text{A}/\text{cm}^2$

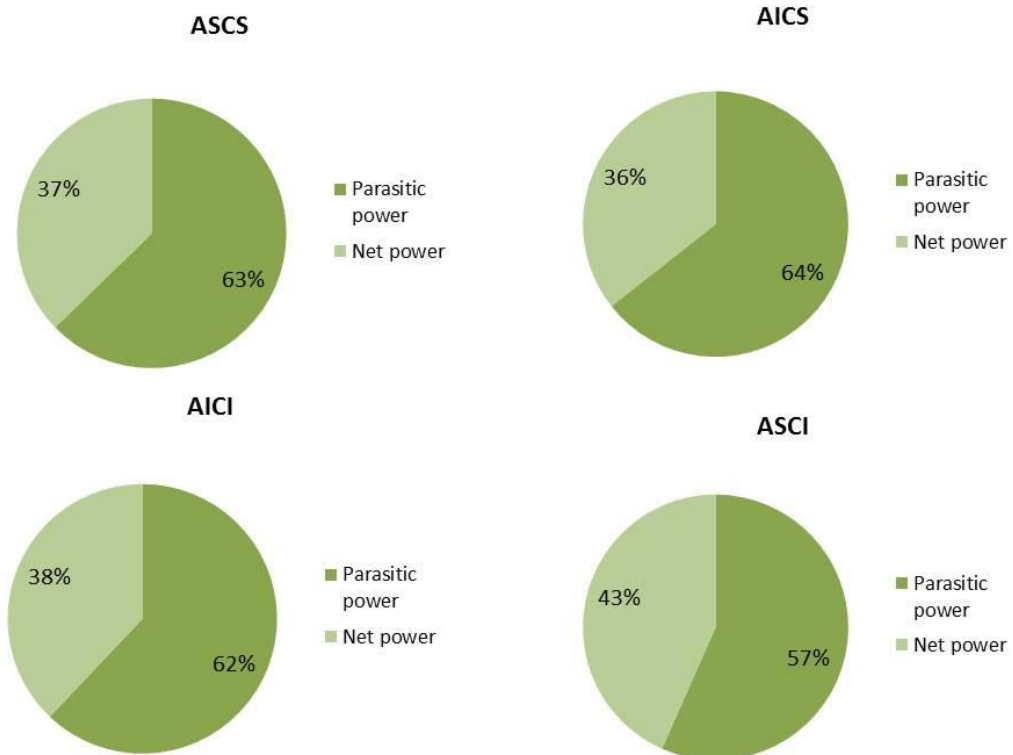


Figure 3.33 Power efficiency of each flow field at standard operating conditions and  $0.5\text{A}/\text{cm}^2$

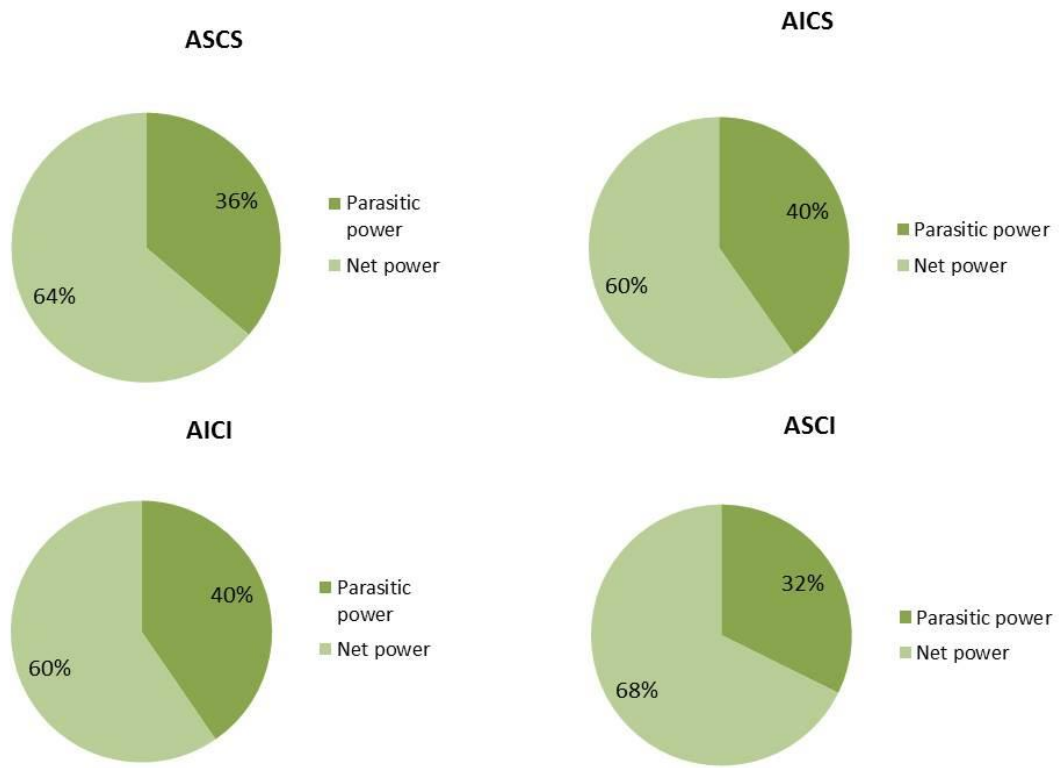


Figure 3.34 Power efficiency of each flow field at standard operating conditions and  $1 \text{ A/cm}^2$

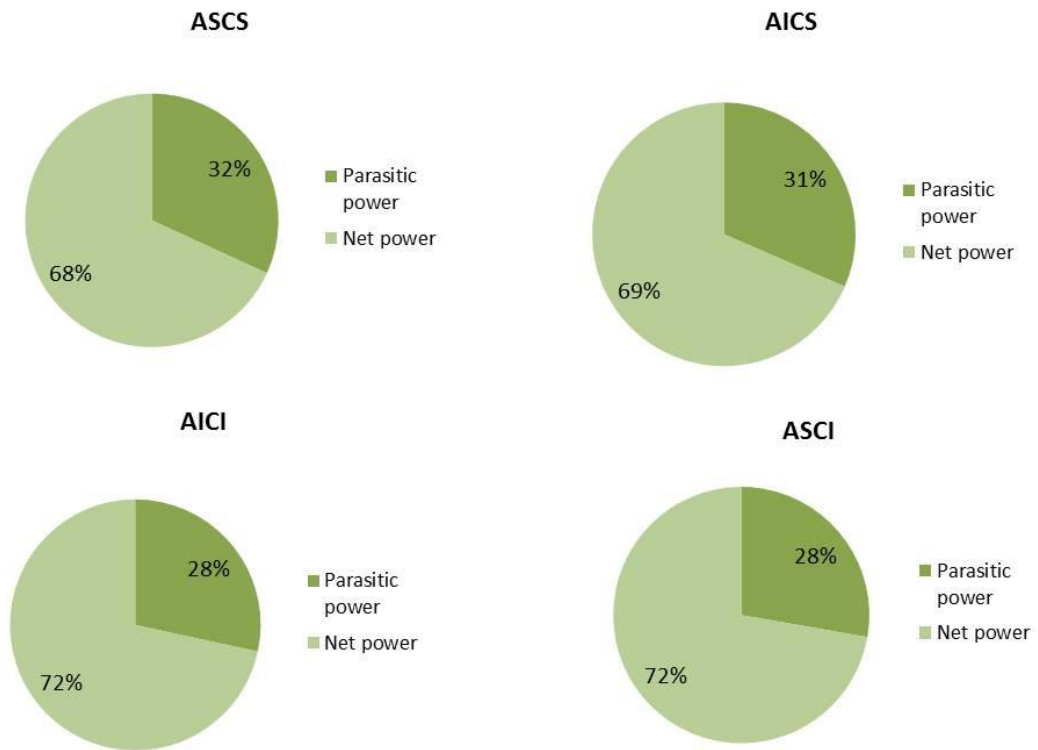
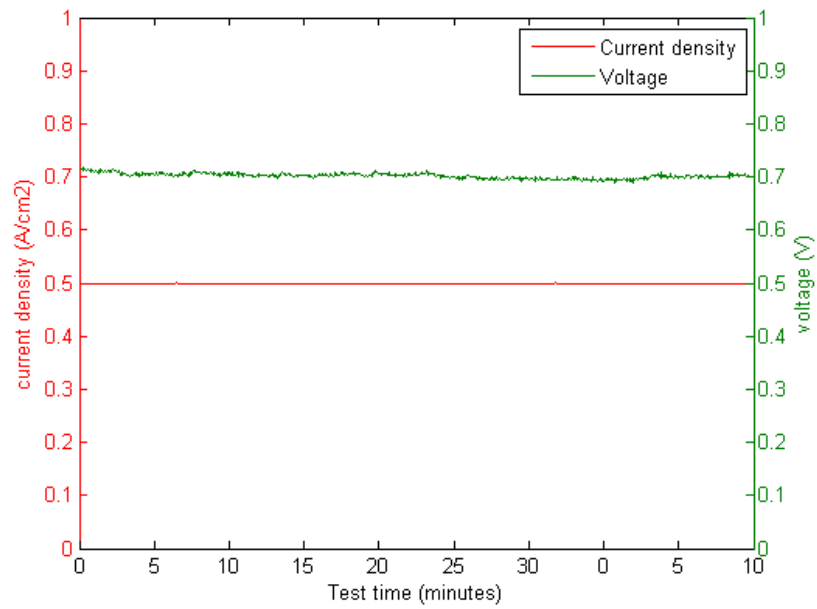
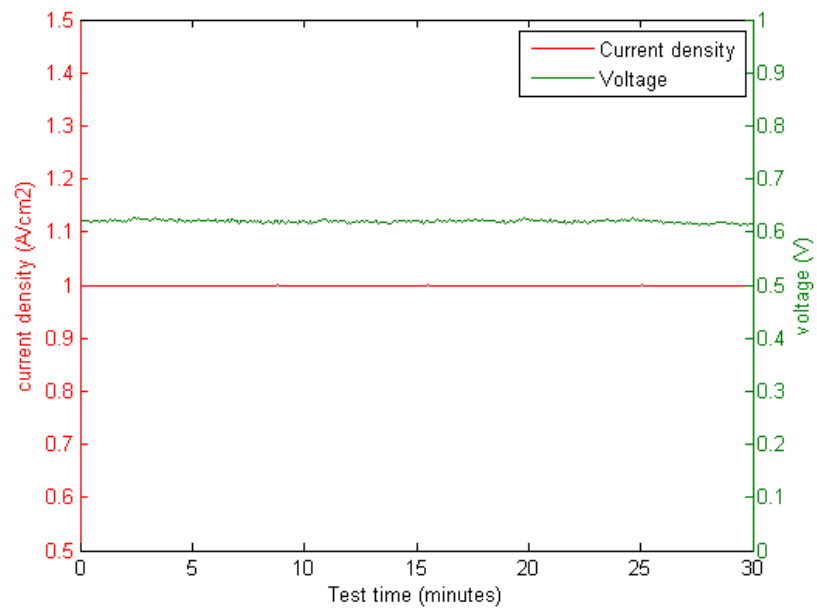


Figure 3.35 Power efficiency of each flow field at standard operating conditions and  $1.5 \text{ A/cm}^2$



**Figure 3.36** Current density and voltage profile of ASCI cell during discharge at  $0.5\text{A}/\text{cm}^2$  for 30 minutes



**Figure 3.37** Current density and voltage profile of ASCI cell during discharge at  $1\text{A}/\text{cm}^2$  for 30 minutes

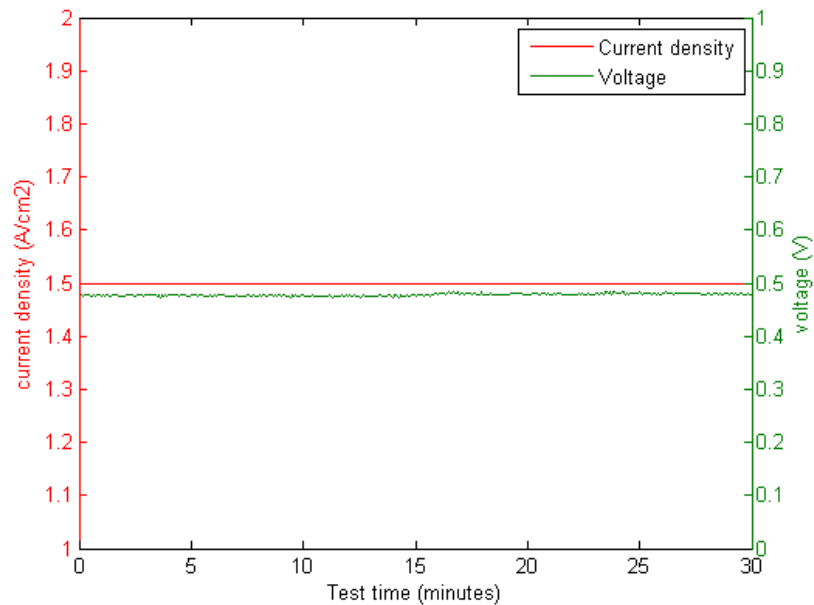


**Figure 3.38** Current density and voltage profile of ASCI cell during discharge at  $1.5\text{A}/\text{cm}^2$  for 30 minutes

### 3.6 Summary

In this chapter, pressure drop data for four flow field combinations was presented and compared, and the effect of operating conditions on pressure drop was also discussed. It was found that the pressure drop in the interdigitated flow field was usually much lower than that in the serpentine flow field. It was also shown that the pressure drop is nearly proportional to the gas flow rate in the same flow field when other operating conditions are the same. The pressure drop at an operating temperature of  $60^\circ\text{C}$  is lower than that at  $70^\circ\text{C}$ . Lower relative humidity at either anode or cathode can also result in a lower pressure drop. In addition, high current densities can cause a higher pressure drop in the same flow field when all the other operating conditions are the same.

Also presented in this chapter were gross power output, parasitic power loss, and net power output for each flow field combination and each set of

operating conditions. The effect of operating condition on energy efficiency of each cell was also discussed. The ASCI cell always gave the best net power output for all operating conditions due to high gross power and low parasitic loss. We also found that a lower oxygen flow rate can give higher energy efficiency than a higher gas flow rate. The current density of  $1.5\text{A}/\text{cm}^2$  leads to higher energy efficiency than the current density  $0.5\text{A}/\text{cm}^2$ . However, the influence of relative humidity and operating temperature on energy efficiency is not as significant as current density and oxygen flow rate.

## Chapter 4

### PRESSURE DROP BEHAVIOR IN PEM FUEL CELLS UNDER FLUCTUATING HUMIDIFICATION TEMPERATURES

#### 4.1 Correlation Between Fuel Cell Voltage and Anode Pressure Drop

During fuel cell operation in automotive, portable and stationary applications, the operating temperature and relative humidity could fluctuate due to imperfections in design or minor disturbances in the cooling system or other auxiliary systems. To understand the effect of temperature fluctuations on fuel cell performance and pressure drop behavior, we exploited fluctuations in the humidification temperature of  $\pm 20^{\circ}\text{C}$  around the set point of  $70^{\circ}\text{C}$ . Figure 4.1 shows the typical pressure drop profiles under such humidification temperature fluctuations. In contrast with the stable pressure drop profiles presented in the section 3.1 wherein the humidification temperature was stable, it is observed that the pressure drop profile in Fig. 4.1 undergoes large fluctuations.

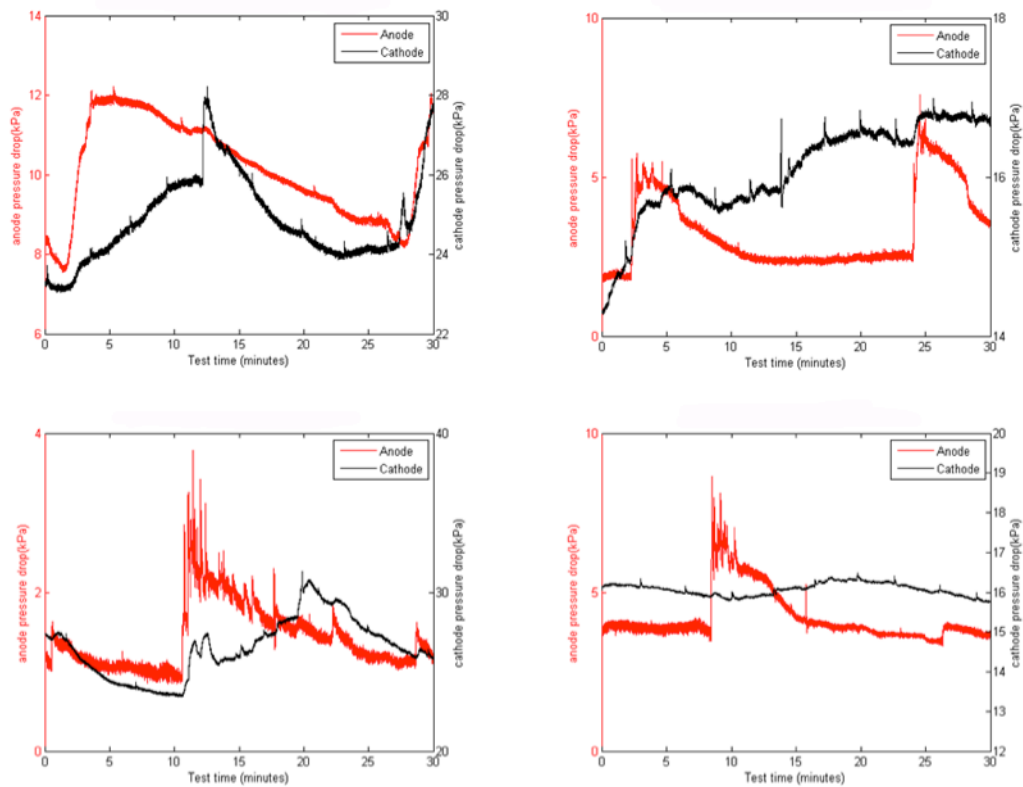


**Figure 4.1** Pressure drop profile in each flow field at  $0.5 \text{ A/cm}^2$  after switching from OCV (2 slpm oxygen flow rate); anode humidification temperature fluctuates in the range of  $\pm 20^\circ\text{C}$ . Upper left: ASCS; Upper right: AICI; Lower left: AICS; Lower right: ASCI.

When the time evolutions of fuel cell output and pressure drop are compared, it is seen that the two profiles are strongly correlated. Fig. 4.2 depicts voltage vs. time overlaid with anode pressure drop vs. time for the AICI case. Both voltage and anode pressure drop show a rapid increase at about 2 min, followed by a long period of decline. Another similar upward spike is seen in both profiles at about 25 min. Clearly, the two profiles are strongly correlated. Since the current density is held constant for this test, the reaction rate and water production rate are fixed as well; therefore, the reason for the positive correlation between voltage and anode pressure drop is not immediately obvious.

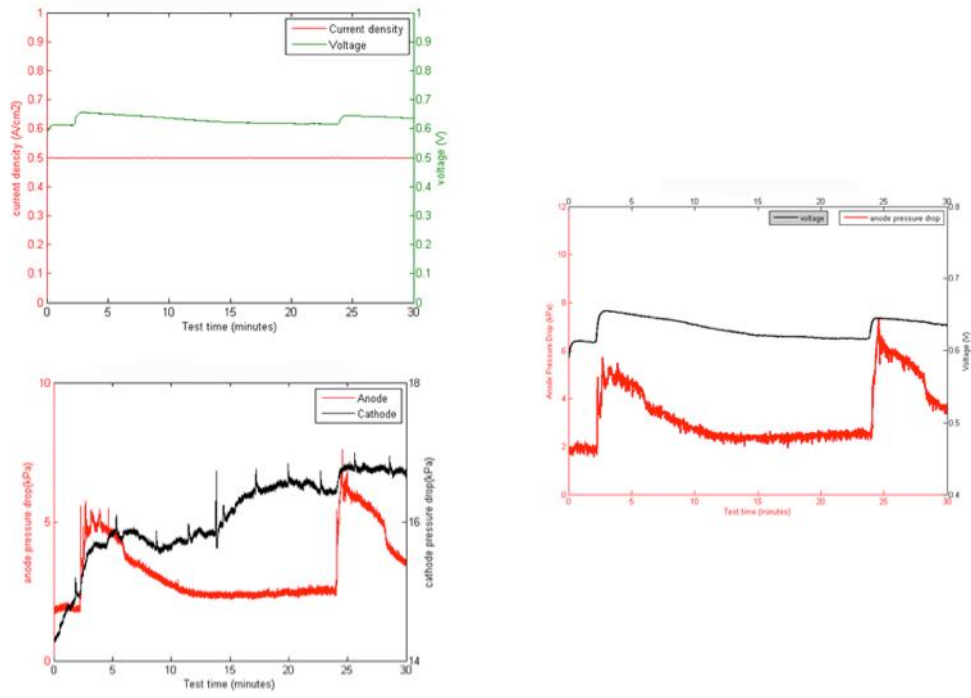
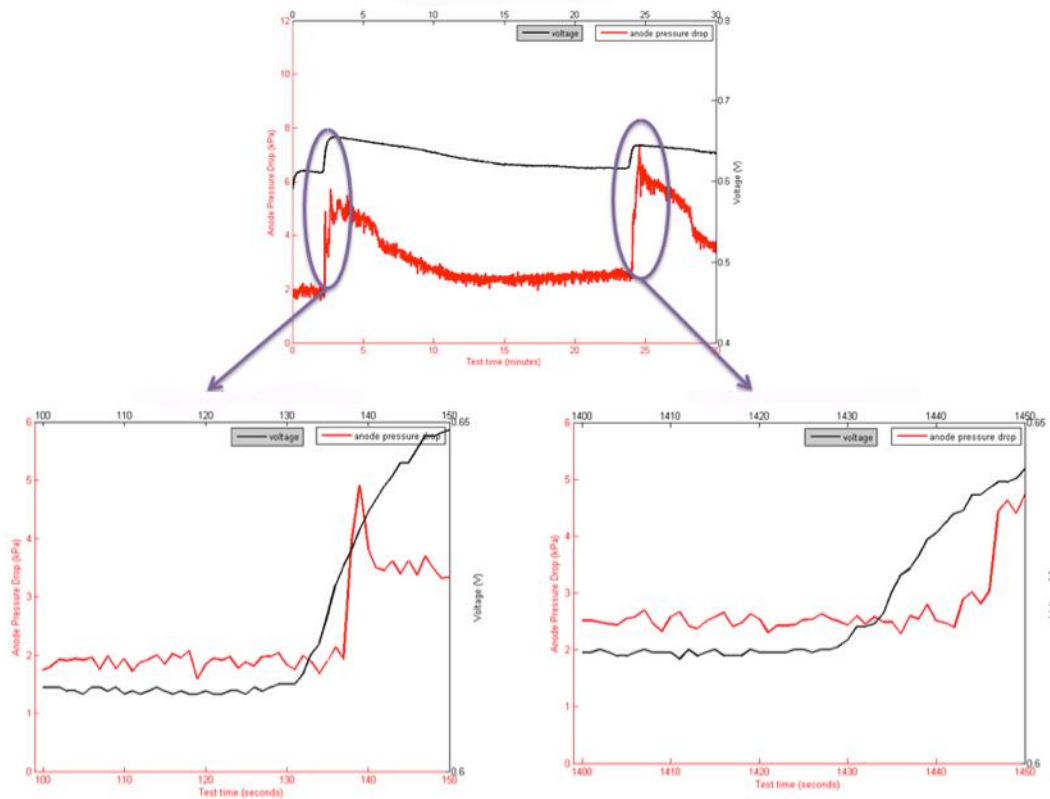


Figure 4.2 AICI cell test at 0.5 A/cm<sup>2</sup>. Upper left: fuel cell performance data; lower left: anode and cathode pressure drop; right: anode pressure drop and voltage data



**Figure 4.3** AICI cell test at  $0.5 \text{ A/cm}^2$ . Upper: time evolution over 30 min of current density overlaid with the anode pressure drop. The other two sub-plots are close-up views of the two spikes over a narrow time span.

To understand the mechanism behind this correlation, we take a closer look at the two profiles in the vicinity of the spikes over a narrow time span of 50 s. In Fig. 4.3, we see that at the first voltage spike commences at 131 s, and the anode pressure drop responds after a slight delay at 138 s. Similarly, at the second spike, the voltage begins to rise at 1430 s, followed by the pressure drop's response at 1445s. The voltage and anode pressure drop profiles were examined for fuel cells with the other flow field combinations as well, and it was noticed that the spike in the pressure drop always followed the voltage spike after a short delay.

Since the water production rate was held constant for these tests, the rise in the anode pressure drop must be due to water buildup in the anode channel. At the same

time, the rise in voltage must be due to a sudden drop in voltage losses. Since internal current and activation losses are less likely to change for the given cell temperature, the most likely scenario is that the ohmic loss was decreased by a sudden improvement in the membrane's proton conductivity. We examined the anode humidifier temperature profile for the same time period from the test datasheet, and investigated the possible influence of humidifier temperature on fuel cell voltage. Fig. 4.4 shows that the cell voltage increased shortly after the hydrogen humidifier temperature spiked, and then decreased after the humidifier temperature dropped. Since the fuel cell was operated at open circuit for 30 min before discharging at  $0.5 \text{ A/cm}^2$ , the membrane might initially be in a relatively dry condition. Due to a spike in the humidifier temperature, the anode RH would rise rapidly improving the membrane's hydration level, and consequently, its proton conductivity. Thus, a spike in the anode humidifier temperature leads to a drop in the ohmic voltage loss, and a spike in the cell voltage. Higher anode RH would also lead to a higher likelihood of liquid water condensation in the anode channels, which will cause a sudden rise in the anode pressure drop. Therefore, we see a strong correlation between the cell voltage and anode pressure drop. Furthermore, because the membrane is very thin, its rate of hydration is quicker than the rate at which water vapor condenses and accumulates in the gas flow channels, therefore the spike in the cell voltage slightly precedes the spike in the anode pressure drop.

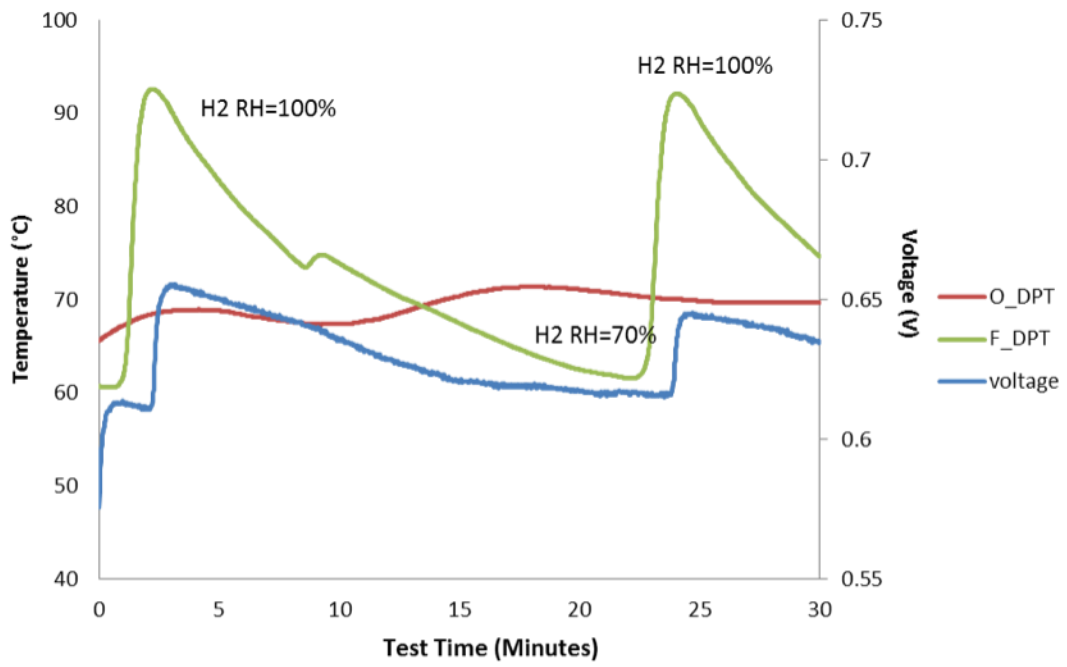
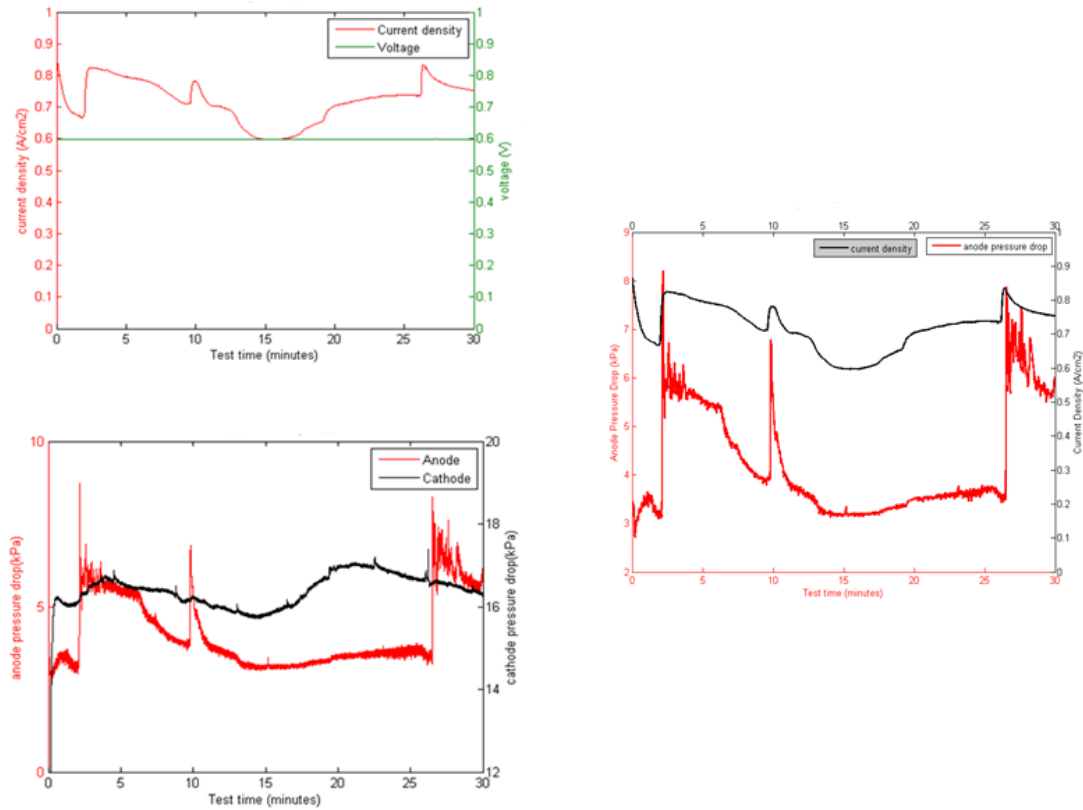


Figure 4.4 Humidification temperature and voltage data for the AICI cell at  $0.5 \text{ A/cm}^2$  for 30 minutes

## 4.2 Correlation Between Fuel Cell Current Density and Pressure Drop



**Figure 4.5** ASCI cell test at 0.6 V. Upper left: fuel cell performance data; lower left: anode and cathode pressure drop; right: anode pressure drop and voltage data

Figure 4.5 depicts the current density overlaid with the anode pressure drop at a fixed voltage of 0.6 V. The spikes in the current curve are strongly correlated with the spikes in the pressure drop profile. As before, we focused on the data in the vicinity of the spikes over a narrow time span of 50 s to investigate the mechanism responsible for this correlation, as shown in Fig. 4.6.

As seen earlier for the case of constant current density where the voltage spikes preceded the spikes in anode pressure drop, Fig. 4.6 shows that when the cell is operated at constant voltage, the current spike precedes the spike in anode pressure drop. It is reasonable that the spike in anode pressure drop is caused by a rise in the water production rate, i.e. the reaction rate, which is proportional to the cell's current

density. Therefore, it stands to reason that the pressure drop rise lags a few seconds behind the sharp rise in current density. To investigate the reason for the spike in current density, we examined the anode humidifier temperature vs. time profile. Fig. 4.7 shows that the two spikes in the hydrogen humidifier temperature correspond closely to the two spikes in the current density curve; moreover, the rise in the humidifier temperature is always followed a short time later by a rise in current density. In fact, this behavior is identical to the one seen earlier in Fig. 4.4. Fig. 4.7 also shows that the sharp increase in current density at around 20 minutes is correlated with an increase in the oxygen humidifier temperature. Higher humidifier temperature on either the anode or the cathode can increase the RH within the cell leading to better membrane hydration and reduced ohmic losses. Therefore, at a fixed cell voltage, a reduction in ohmic losses has the effect of increasing the cell's current. A higher current implies a higher reaction rate, which means that the water production rate increases. Higher relative humidity also can aggravate flooding within the flow field channels. Considering the influence of both higher water production rate and higher water content in the incoming gas flow, we can conclude that they together contribute to the increase in the pressure drop; furthermore, it also explains why the rise in pressure drop lags slightly behind the rise in current density.

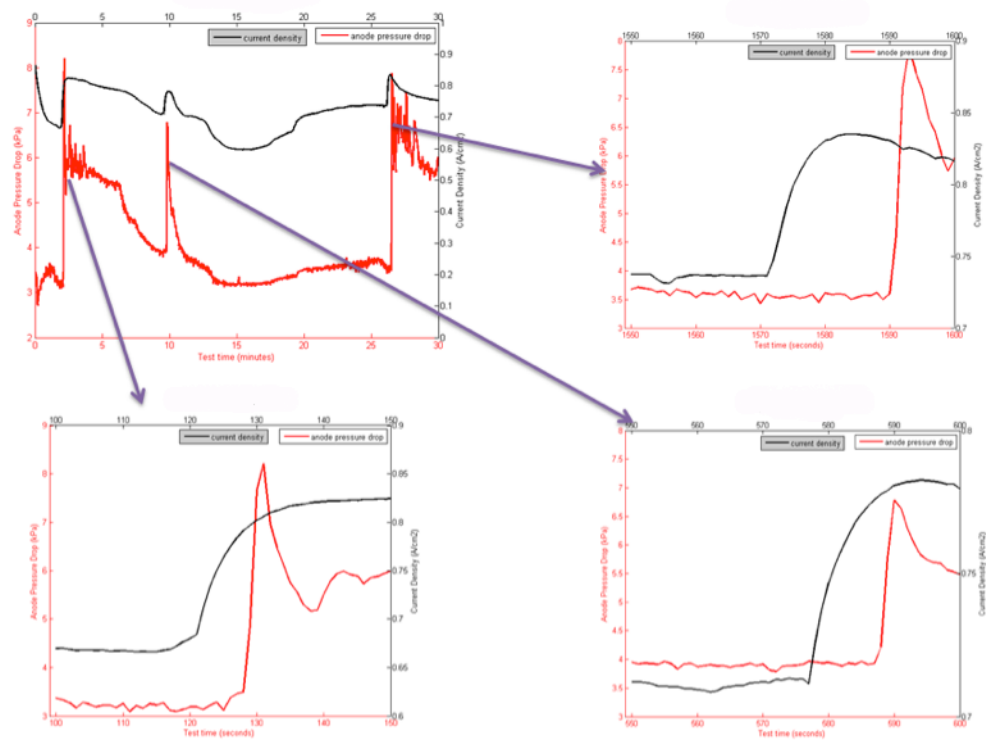


Figure 4.6 ASCI cell test at 0.6 V. Upper left: time evolution over 30 min of current density overlaid with the anode pressure drop. The other three sub-plots are close-up views of the three spikes over a narrow time span.

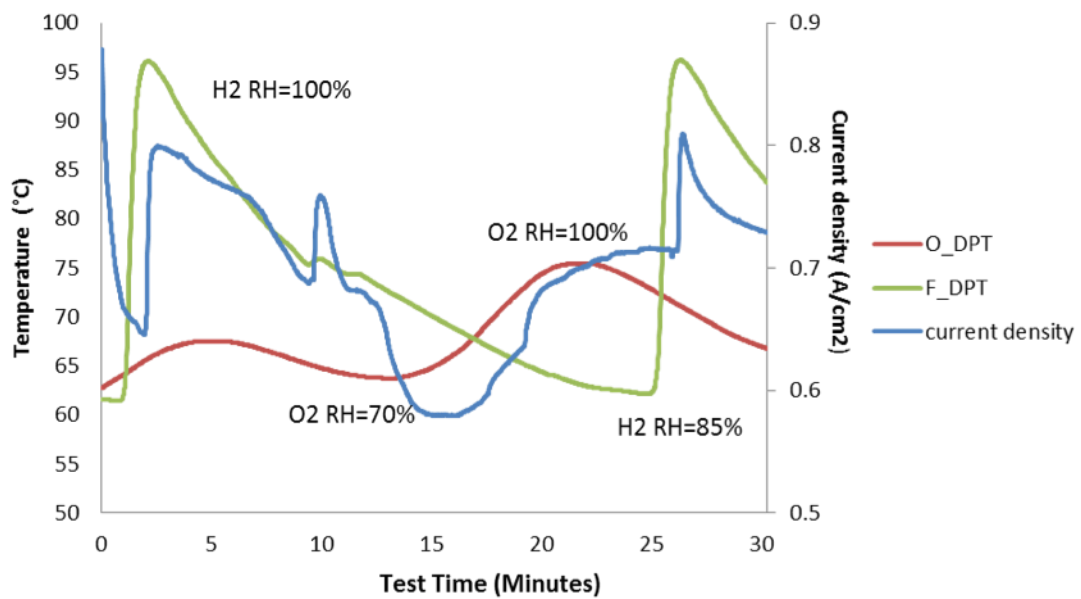


Figure 4.7 Humidification temperature and voltage data for the ASCI cell at 0.6 V for 30 minutes

### 4.3 Correlation Coefficients

We calculated the correlation coefficients between the anode pressure drop and cell output (voltage in the case of fixed current density, or current density in the case of fixed voltage) for each test run at standard operating conditions. The results are summarized in Fig. 4.8 and confirm that there is always a strong correlation between

anode pressure drop and cell output (correlation coefficient always exceeds 0.5).

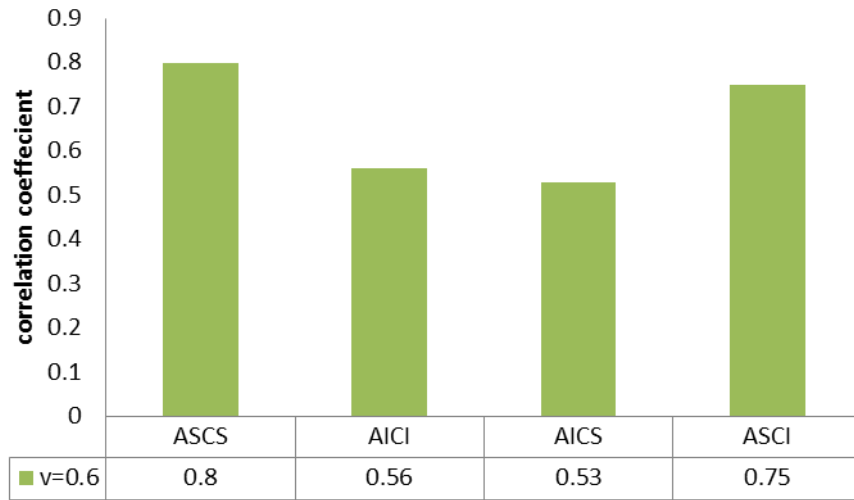


Figure 4.8 Correlation coefficients of anode pressure drop and cell current density at 0.6 V

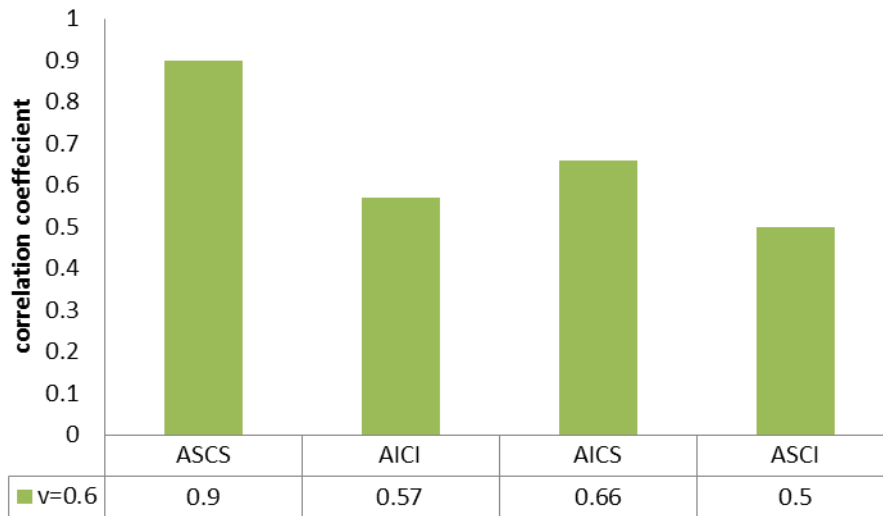


Figure 4.9 Correlation coefficients of anode pressure drop and cell voltage at 0.5A/cm<sup>2</sup>

#### 4.4 Discussion

From Fig.4.2 and Fig. 4.5, it is interesting to note that the correlation between the anode pressure drop with fuel cell output is stronger than that between the cathode

pressure drop and cell output. For example, in Fig. 4.5, all the spikes in the current curve correspond with the spikes in the anode pressure drop profile; however, a similar correspondence is not evident for the cathode pressure drop profile. This could be due to the fact that the anode humidifier temperature experienced larger fluctuations than the cathode humidifier temperature. Consequently, the RH fluctuations on the anode side are larger, leading to a higher propensity for flooding in the anode channels and the associated rise in the anode pressure drop.

#### **4.5 Summary**

In this chapter, we exploited fluctuations in the humidifier temperature of  $\pm 20^{\circ}\text{C}$  around the set point of  $70^{\circ}\text{C}$  to understand the effect of temperature fluctuations on fuel cell performance and pressure drop behavior. Positive correlation between anode pressure drop and fuel cell output was found. We took a closer look at the anode pressure drop and fuel cell output profiles in the vicinity of spikes over a narrow time span of 50 s and found that the fuel cell power output spike precedes the spike in anode pressure drop. By examining the humidifier temperature vs. time profile, we found that spikes in the humidifier's temperature raised the RH in the cell and led to an increase in the membrane's proton conductivity which reduced ohmic losses. Consequently, fuel cell performance improved. At the same time, higher anode RH also increases the likelihood of liquid water condensation in the anode channels. This explains the positive correlation between fuel cell output and pressure drop.

## Chapter 5

### CONCLUSIONS AND FUTURE WORK

In this work, a novel asymmetric flow field combination design for PEMFCs was presented and its effect on net power output was investigated. The two new flow field combinations investigated here were anode-serpentine/cathode-interdigitated (ASCI), and anode-interdigitated/cathode-serpentine (AICS), and their performance was compared against conventional serpentine and interdigitated flow field designs. Net power output was evaluated for PEMFCs with four sets of flow field combinations using performance data and pressure drop data collected from test runs at constant voltage or constant current. The pressure drop of each cell under different test conditions was presented and compared. It was found that at high oxygen flow rate, high humidity and high current density could cause a relatively high pressure drop, and thus a large parasitic loss.

We also measured performance and pressure drop data for different sets of operating conditions and calculated the net power output and energy efficiency for each specific operating condition. Results show that the ASCI cell always has the best net power output among the four types of flow fields across all operating conditions tested due to a reasonably good performance combined with a small parasitic loss. ANOVA analysis was conducted for all the calculated results to assess the relative magnitude of random error in the experimental results. We also discussed the influence of operating conditions on the energy efficiency of the cells; for example, a

reduced oxygen flow rate can help to improve the energy efficiency by reducing parasitic losses significantly.

In conclusion, the new anode-serpentine/cathode-interdigitated PEMFC design evaluated in this work can significantly improve the net power output of the PEMFC system because of its low parasitic power losses, and offers a simple way to improve the net performance of PEM fuel cells, making it more cost effective.

The mechanisms responsible for dynamic changes in the anode and cathode pressure drops were also studied and discussed in this work; these studies led to a better understanding of the electrochemical reaction rates and their impact on water dynamics in the PEMFC. An increasing trend was found in some of the pressure drop profiles; as operation time increases, water is produced, diffused and condensed continuously inside the fuel cell, and the accumulation of liquid water in the gas channel can result in an increase in the pressure drop.

Besides power analysis, we also investigated dynamic fluctuations in the pressure drop and their relationship with fluctuations in the cell output and humidifier temperature. We found that the pressure drop in the flow channels always showed a positive correlation with the cell output; furthermore, the anode pressure drop was more strongly correlated with cell output than the cathode pressure drop since only the anode humidifier experienced large temperature fluctuations. The positive correlation between cell output and pressure drop arises from the spikes in humidifier temperature which raise the RH in the cell causing an increase in proton conductivity and reduced ohmic losses. The positive correlation is even stronger when the cell is operated at 50% relative humidity. The above findings confirm that inlet gas humidity can play an important role in PEM fuel cell operation due to its strong influence on proton

conductivity, reaction rate, liquid water dynamics, and compressor power consumption. Therefore, it influences the overall performance and net power output of the PEMFC system.

Due to limited time, in addition to the baseline value, we explored the influence of cell temperature and relative humidity at one other value (temperature 60°C and RH 50%). Future work can examine the influence of temperature and RH by conducting a systematic parametric study. For example, temperature can be varied from 30°C to 90°C in 10°C increments to determine the effect of low and high temperature on cell net power output for ASCI and AICS cells. Optimized operating conditions for each flow field can also be studied in the future. Finally, all of the studies presented here pertain to single cells; it would be useful to study how these novel asymmetric flow field combinations would perform when employed within a stack to assess energy savings.

## REFERENCES

- [1] Pukrushpan, J. T. (2003). Modeling and control of fuel cell systems and fuel processors, Doctoral Dissertation, University of Michigan.
- [2] Lee, H. J. (2009). Modeling and Analysis of a PEM Fuel Cell System for a Quadruped Robot, Master of Science Thesis, Mechanical Engineering, Auburn University
- [3] Catlin, G. (2010). PEM fuel cell modeling and optimization using a genetic algorithm, Master of Science Thesis, Mechanical Engineering, University of Delaware
- [4] Wang, L., and Liu, H. (2004). Performance studies of PEM fuel cells with interdigitated flow fields. *Journal of Power Sources*, 134(2), 185-196.
- [5] Larminie, J., Dicks, A., and McDonald, M.S. *Fuel cell systems explained*, Second Ed., John Wiley & Sons Ltd, Chichester, 2003.15
- [6] Hermann, A., Chaudhuri, T., & Spagnol, P. (2005). Bipolar plates for PEM fuel cells: A review. *International Journal of Hydrogen Energy*, 30(12), 1297-1302.
- [7] Spornjak, D., Prasad, A. K., & Advani, S. G. (2010). In situ comparison of water content and dynamics in parallel, single-serpentine, and interdigitated flow fields of

polymer electrolyte membrane fuel cells. *Journal of Power Sources*, 195(11), 3553-3568.

[8] Kuo, J. K., Yen, T. S., & Chen, C. O. K. (2008). Improvement of performance of gas flow channel in PEM fuel cells. *Energy Conversion and Management*, 49(10), 2776-2787.

[9] Wang, L., Husar, A., Zhou, T., and Liu, H. (2003). A parametric study of PEM fuel cell performances. *International Journal of Hydrogen Energy*, 28(11), 1263-1272.

[10] Barbir, F., Balasubramanian, B., and Neutzler, J. K. (1999). Trade-off design study of operating pressure and temperature in PEM fuel cell systems. In 1999 ASME International Mechanical Engineering Congress and Exposition.

[11] Barbir, F. (1999). Review of hydrogen conversion technologies. *Hemijaska Industrija*, 53(12), 426-433.

[12] Liu, X., et al. (2007). Water flooding and pressure drop characteristics in flow channels of proton exchange membrane fuel cells. *Electrochimica Acta* 52(11): 3607-3614.

[13] Spornjak, D. (2010). Experimental characterization of water transport in polymer electrolyte fuel cells, Doctoral Dissertation, University of Delaware

[14] Bosco, A. D., and Fronk, M. H. (2000). U.S. Patent No. 6,103,409. Washington, DC: U.S. Patent and Trademark Office.

[15] M.F. Mathias and S.A. Grot, System and method for controlling the humidity level of a fuel cell, U.S. Patent 6,376,111, 2002

## Appendix A

### CALCULATION OF COMPRESSOR POWER

In Chapter 3, the method to calculate compressor power losses and net power output was given. Here it is explained again with more details:

Compressor power is evaluated using the given equation:

$$P_{compressor} = c_p \frac{T_1}{\eta_m \eta_c} \dot{m} \left[ \left( \frac{p_2}{p_1} \right)^{\frac{\gamma-1}{\gamma}} - 1 \right] \quad (1)$$

On the basis of the above equation, the compressor power for each cell discharging at constant voltage or constant current density for 30 minutes was calculated. Since the sampling rate for pressure drop is 1 Hz, the compressor power can be calculated at the same rate. The total energy consumed by the compressor is obtained by integrating the compressor power over its 30 min operation.

The total power generated by fuel cell was obtained using performance data for each test. Since the sampling rate of voltage and current density data is also 1 Hz, the total energy generated by the cell is obtained by integrating the instantaneous power over 30 min. The difference between the total energy generated by the cell and the total energy consumed by compressor is defined as the net energy output over 30 min. The average net power is calculated by dividing the net energy output by 1800s. In this manner, we obtained the net power for each test, namely as the difference between cell's power output and the parasitic power losses.

Since we repeated tests three times at each specific operating condition for each cell, we obtained three sets of power data for each test group; the mean of these three data sets was used for presentation and comparison in this thesis. Detailed data for each test are presented below.

	Serpentine	Interdigitated	AICS	ASCI
<b><math>\Delta p</math> (kPa)</b>	29.90	12.90	29.00	12.00
	30.00	14.30	29.20	13.47
	30.00	13.61	29.50	13.07
<b>Parasitic power</b>	5.52	4.96	5.49	4.93
	5.53	5.00	5.50	4.98
	5.53	4.98	5.51	4.96
<b>Power output</b>	11.51	10.27	10.68	11.52
	11.40	11.01	10.70	11.09
	11.55	10.76	11.30	11.30
<b>Net Power</b>	5.99	5.31	5.19	6.59
	5.87	6.01	5.20	6.11
	6.02	5.78	5.79	6.34
<b>Standard deviation mean of net power</b>	0.06	0.29	0.28	0.20
	5.96	5.70	5.39	6.35

Table A.1 Voltage=0.6V; oxygen flow rate=2 slpm; temperature=70°C; anode RH=50%; cathode RH=100%

	Serpentine	Interdigitated	AICS	ASCI
<b><math>\Delta p</math> (kPa)</b>	26.71	10.55	25.90	9.60
	25.55	10.49	25.40	9.66
	26.50	10.51	25.30	9.71
<b>Parasitic power</b>	5.42	4.88	5.39	4.84
	5.38	4.87	5.38	4.84
	5.41	4.87	5.37	4.85
<b>Power output</b>	10.80	10.10	10.12	11.30
	11.31	9.95	10.40	11.22
	11.02	9.66	10.43	10.90
<b>Net Power</b>	5.38	5.22	4.73	6.46
	5.93	5.08	5.02	6.38
	5.61	4.79	5.06	6.05
<b>Standard deviation mean of net power</b>	0.22	0.18	0.15	0.17
	5.64	5.03	4.94	6.30

Table A.2 Voltage=0.6V; oxygen flow rate=2; slpm temperature=70°C; anode RH=100%; cathode RH=50%

	Serpentine	Interdigitated	AICS	ASCI
$\Delta p$ (kPa)	12.67	6.51	9.65	5.73
	13.10	6.46	11.80	5.85
	13.10	6.38	11.80	5.81
Parasitic power	2.47	2.37	2.42	2.35
	2.48	2.37	2.46	2.36
	2.48	2.37	2.46	2.36
Power output	10.58	10.10	9.50	10.40
	10.16	9.90	10.00	10.20
	10.30	10.08	9.96	10.55
Net Power	8.11	7.73	7.08	8.05
	7.68	7.53	7.54	7.84
	7.82	7.71	7.50	8.19
Standard deviation mean of net power	0.18	0.09	0.21	0.14
	7.87	7.66	7.37	8.03

Table A.3 Voltage=0.6V; oxygen flow rate=1 slpm; temperature=70°C; anode RH=100%; cathode RH=100%

	Serpentine	Interdigitated	AICS	ASCI
$\Delta p$ (kPa)	73.40	35.87	72.30	29.50
	74.00	35.47	73.00	31.10
	73.30	36.12	73.50	30.50
Parasitic power	13.70	11.43	13.63	11.02
	13.73	11.40	13.67	11.12
	13.69	11.45	13.35	11.08
Power output	16.16	16.09	14.65	16.25
	16.40	15.72	15.13	15.93
	16.55	15.48	14.50	16.40
Net Power	2.46	4.66	1.02	5.23
	2.67	4.32	1.46	4.81
	2.86	4.03	1.15	5.32
Standard deviation mean of net power	0.16	0.26	0.54	0.22
	2.67	4.34	0.88	5.12

Table A.4 Voltage=0.6V; oxygen flow rate=4; slpm temperature=70°C; anode RH=100%; cathode RH=100%

	Serpentine	Interdigitated	AICS	ASCI
$\Delta p$ (kPa)	24.60	12.23	22.00	11.00
	24.75	12.70	22.80	10.52
	24.78	12.60	23.10	9.40
Parasitic power	5.35	4.93	5.26	4.89
	5.35	4.95	5.29	4.87
	5.36	4.95	5.30	4.84

<b>Power output</b>	10.15	8.75	9.50	9.96
	9.96	9.10	9.83	10.50
	10.04	9.02	9.17	10.08
<b>Net Power</b>	4.80	3.82	4.24	5.07
	4.61	4.15	4.54	5.63
	4.68	4.07	3.87	5.24
<b>Standard deviation mean of net power</b>	0.08	0.14	0.27	0.23
	4.70	4.01	4.22	5.31

Table A.5 Voltage=0.6V; oxygen flow rate=2; slpm temperature=60°C; anode RH=100%; cathode RH=100%

	Serpentine	Interdigitated	AICS	ASCI
<b><math>\Delta p</math> (kPa)</b>	28.30	13.79	26.24	11.75
	28.60	14.1	26.40	12.00
	29.08	13.92	26.12	12.10
<b>Parasitic power</b>	5.47	4.99	5.40	4.92
	5.48	5.00	5.41	4.93
	5.50	4.99	5.40	4.93
<b>Power output</b>	14.90	13.40	12.80	15.00
	15.00	12.65	13.20	14.70
	15.03	13.42	12.90	14.98
<b>Net Power</b>	9.43	8.41	7.40	10.08
	9.52	7.65	7.79	9.77
	9.53	8.43	7.50	10.05
<b>Standard deviation mean of net power</b>	0.05	0.36	0.17	0.14
	9.49	8.16	7.56	9.97

Table A.6 Voltage=0.6V; oxygen flow rate=2; slpm temperature=70°C; anode RH=100%; cathode RH=100%

	Serpentine	Interdigitated	AICS	ASCI
<b><math>\Delta p</math> (kPa)</b>	29.10	14.1	26.20	12.36
	30.20	12.98	26.50	11.90
	29.64	13.60	26.40	11.84
<b>Parasitic power</b>	5.50	5.00	5.40	4.94
	5.53	4.96	5.41	4.92
	5.51	4.98	5.41	4.92
<b>Power output</b>	15.45	12.55	13.21	15.46
	15.06	12.33	13.20	15.30
	15.23	12.10	13.90	14.98
<b>Net Power</b>	9.95	7.55	7.81	10.52
	9.53	7.37	7.79	10.38
	9.72	7.12	8.49	10.06
<b>Standard deviation mean of net power</b>	0.17	0.18	0.33	0.19
	9.73	7.35	8.03	10.32

Table A.7 Current density 1A/cm<sup>2</sup> ;oxygen flow rate=2; slpm temperature=70°C; anode RH=100%; cathode RH = 100%

	Serpentine	Interdigitated	AICS	ASCI
<b>Δp (kPa)</b>	33.24	13.4	26.83	14.30
	33.00	13.36	26.51	13.50
	32.89	13.35	26.36	13.40
<b>Parasitic power</b>	5.63	4.97	5.42	5.00
	5.62	4.97	5.41	4.98
	5.62	4.97	5.41	4.97
<b>Power output</b>	17.90	17.29	17.20	17.80
	17.72	17.51	17.53	18.10
	17.38	17.73	16.86	18.00
<b>Net Power</b>	12.27	12.32	11.78	12.80
	12.10	12.54	12.12	13.12
	11.76	12.76	11.45	13.03
<b>Standard deviation mean of net power</b>	0.21	0.18	0.27	0.14
	12.04	12.54	11.78	12.98

Table A.8 Current density=1.5A/cm<sup>2</sup> ;oxygen flow rate=2; slpm temperature=70°C; anode RH=100%; cathode RH=100%

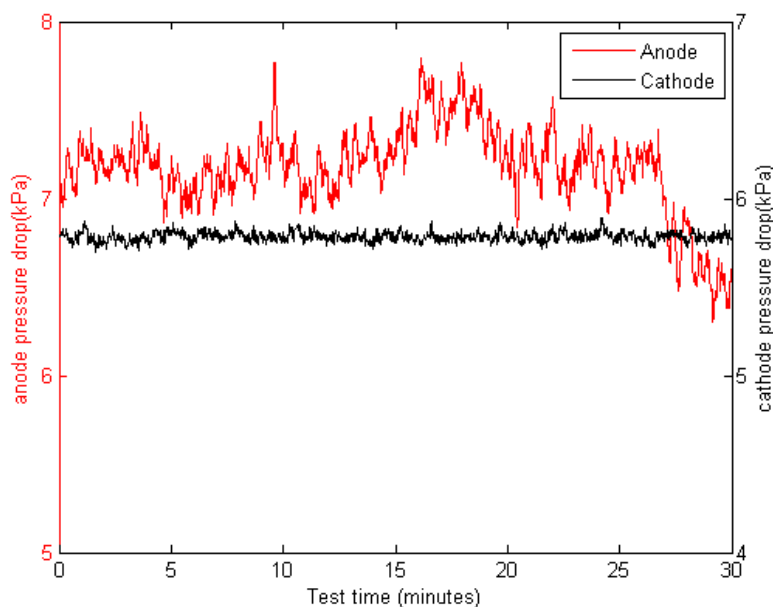
	Serpentine	Interdigitated	AICS	ASCI
<b>Δp (kPa)</b>	24.90	12.93	27.84	13.51
	25.53	12.56	28.10	12.62
	26.34	13.14	27.99	12.80
<b>Parasitic power</b>	5.36	4.96	5.46	4.98
	5.38	4.94	5.46	4.95
	5.41	4.96	5.46	4.95
<b>Power output</b>	8.71	8.16	8.33	8.78
	8.49	7.94	8.57	8.50
	8.55	7.85	8.54	8.99
<b>Net Power</b>	3.35	3.20	2.87	3.80
	3.11	3.00	3.11	3.55
	3.14	2.89	3.08	4.04
<b>Standard deviation mean of net power</b>	0.11	0.13	0.10	0.20
	3.20	3.03	3.02	3.80

Table A.9 Current density=0.5A/cm<sup>2</sup> ;oxygen flow rate=2; slpm temperature=70°C; anode RH=100%; cathode RH=100%

## Appendix B

### PRESSURE DROP AND CELL OUTPUT DATA

In Chapter 3, average pressure drop data and cell output data were presented for each test group; however, actual pressure drop curves and cell performance curves were not shown for brevity. Here, representative plots are presented for each test group to show the actual pressure drop vs. time and cell output vs. time profiles.



**Figure B.1 Pressure drop profile in ASCI flow field during discharge at 0.6V and oxygen flow rate of 1 slpm for 30 minutes**

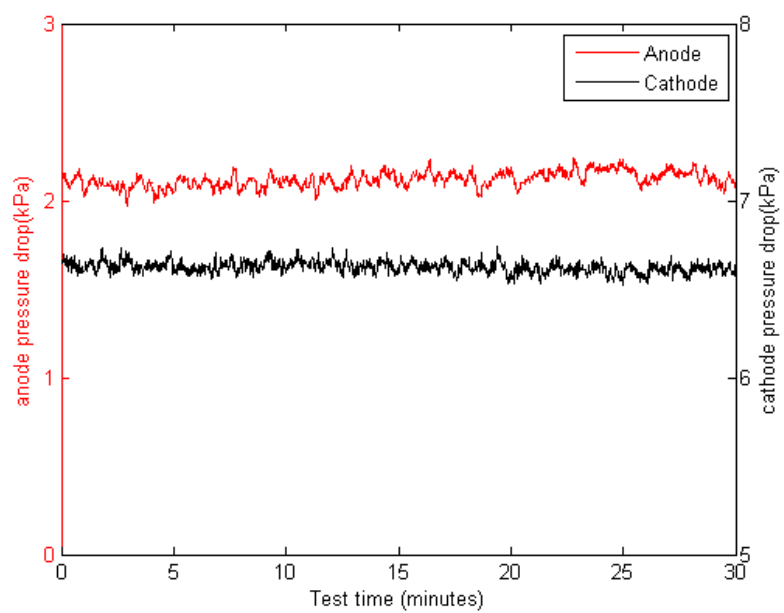


**Figure B.2 Pressure drop profile in AICI flow field during discharge at 0.6V and oxygen flow rate of 1 slpm for 30 minutes**

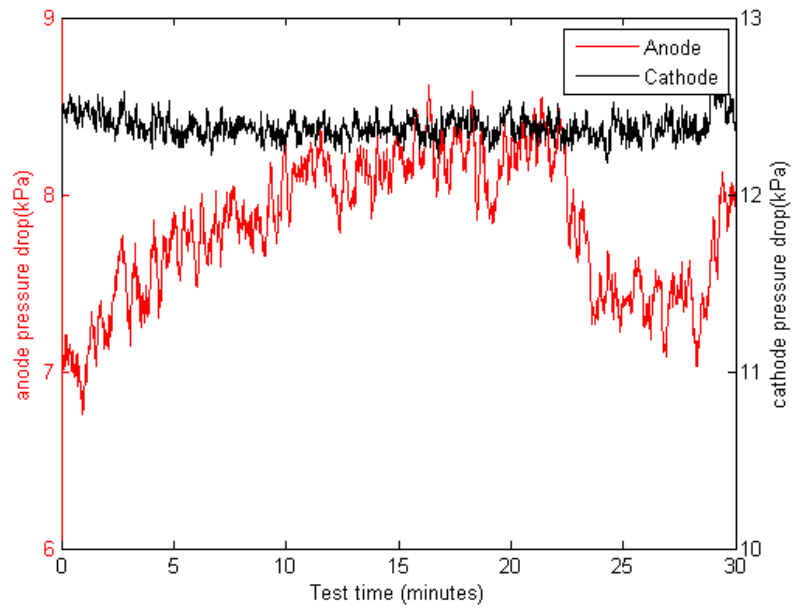


**Figure B.3** Pressure drop profile in ASCS flow field during discharge at 0.6V and oxygen flow rate of 1 slpm for 30 minutes

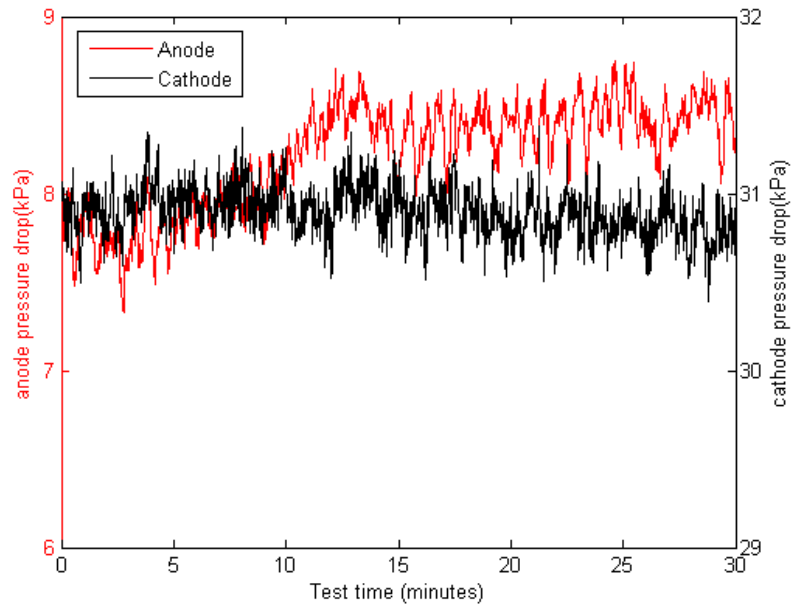


**Figure B.4** Pressure drop profile in ASCI flow field during discharge at 0.6V and oxygen flow rate of 4 slpm for 30 minutes

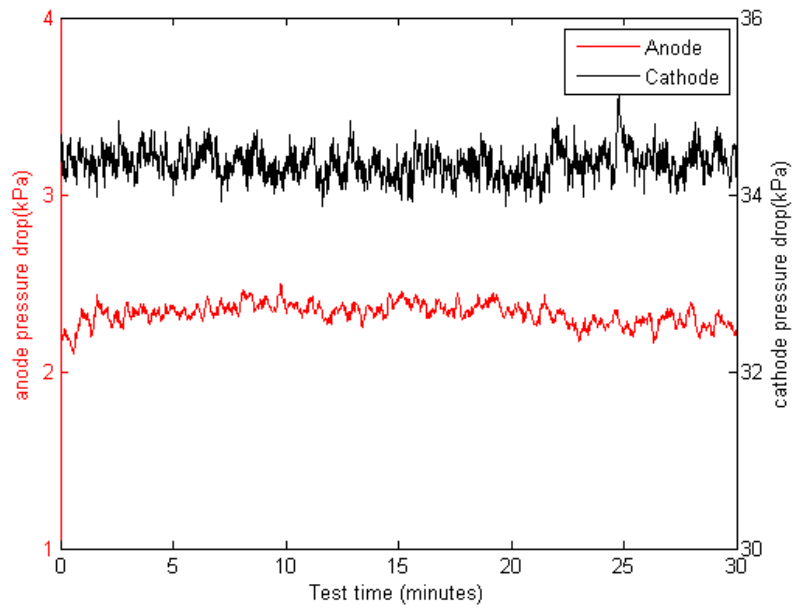


**Figure B.5** Pressure drop profile in AICI flow field during discharge at 0.6V and oxygen flow rate of 4 slpm for 30 minutes

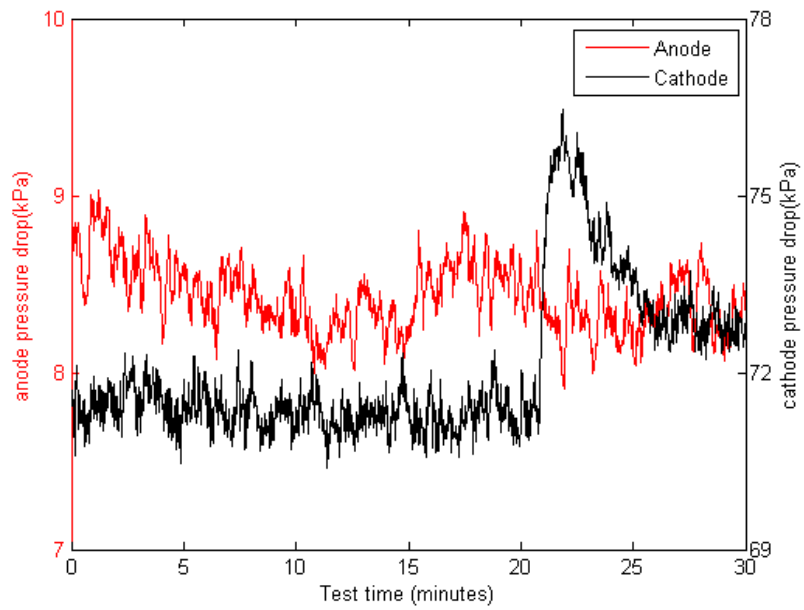


**Figure B.6** Pressure drop profile in ASCS flow field during discharge at 0.6V and oxygen flow rate of 4 slpm for 30 minutes

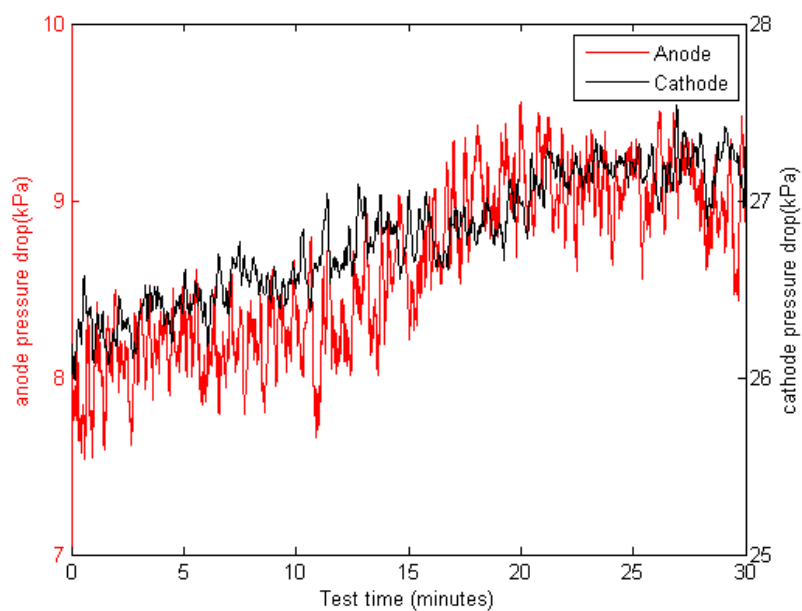


**Figure B.7** Pressure drop profile in ASCII flow field during discharge at 0.6V cathode RH 50% for 30 minutes

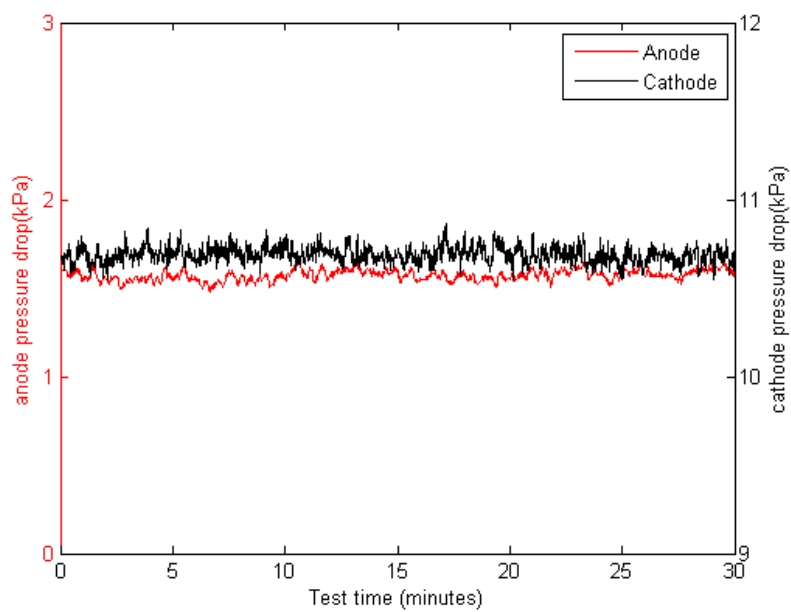


**Figure B.8** Pressure drop profile in AICI flow field during discharge at 0.6V and cathode RH 50% for 30 minutes

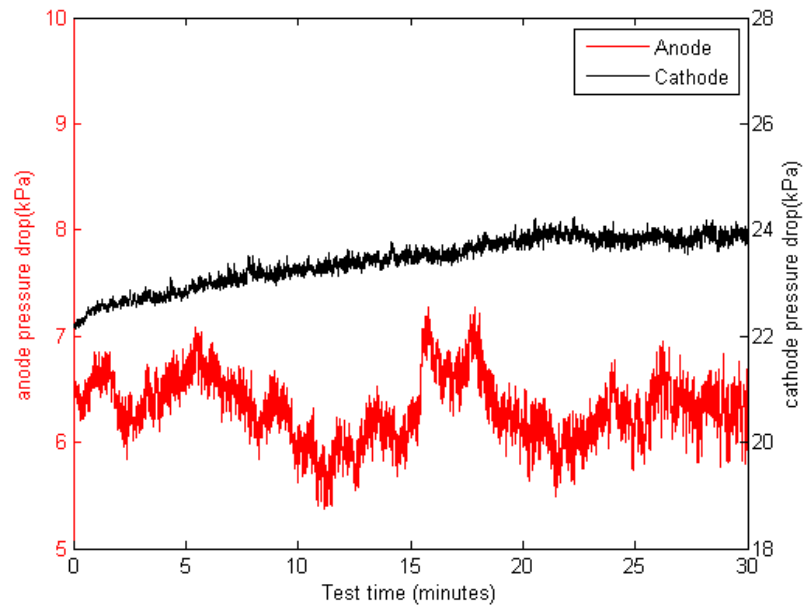


**Figure B.9** Pressure drop profile in ASCS flow field during discharge at 0.6V and cathode RH 50% for 30 minutes

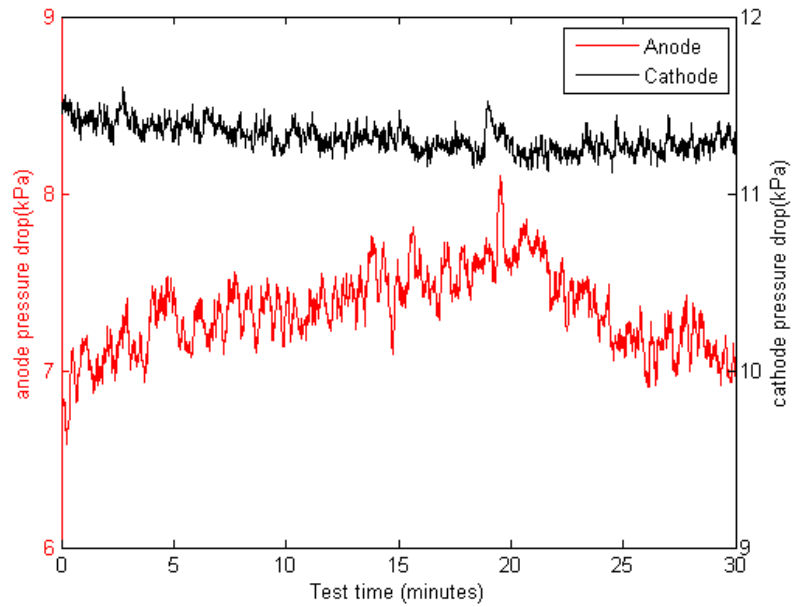


**Figure B.10** Pressure drop profile in ASCI flow field during discharge at 0.6V and 60°C for 30 minutes

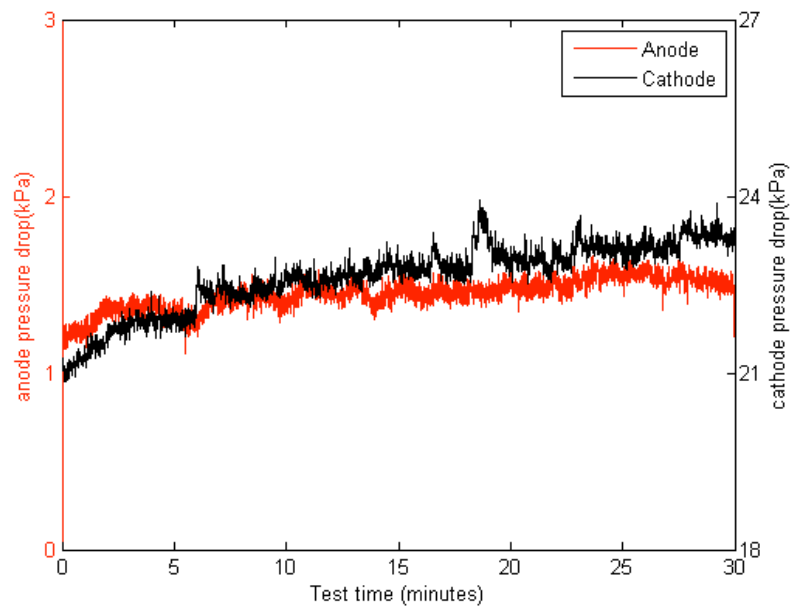


**Figure B.11** Pressure drop profile in AICS flow field during discharge at 0.6V and 60°C for 30 minutes

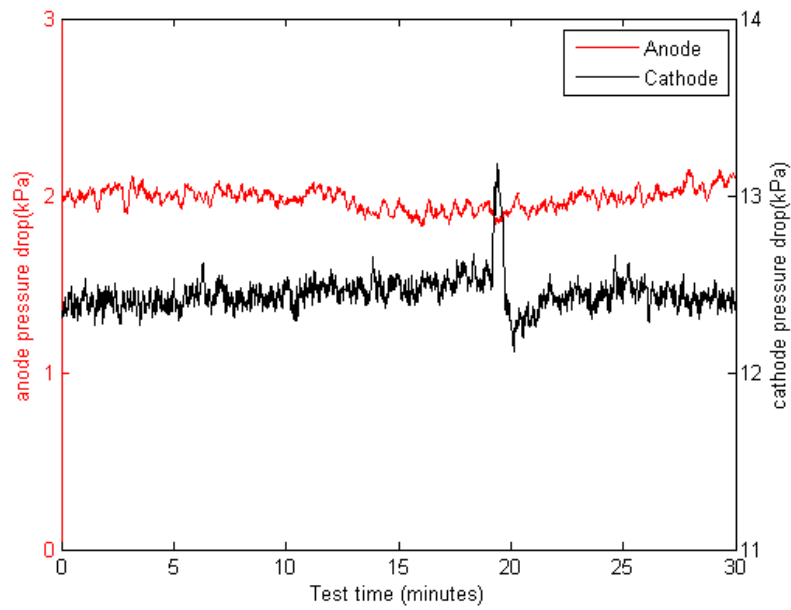


**Figure B.12** Pressure drop profile in AICI flow field during discharge at 0.6V and 60°C for 30 minute

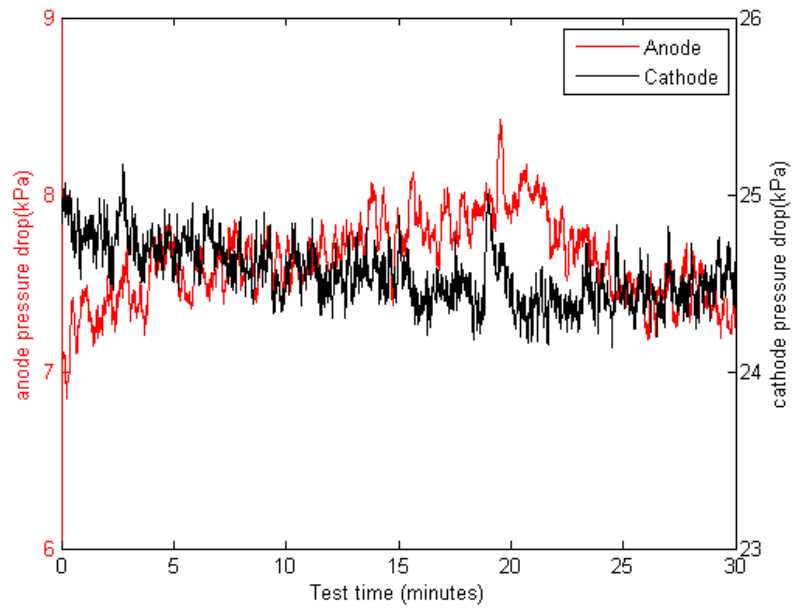


**Figure B.13** Pressure drop profile in ASCI flow field during discharge at 0.6V and 60°C for 30 minutes

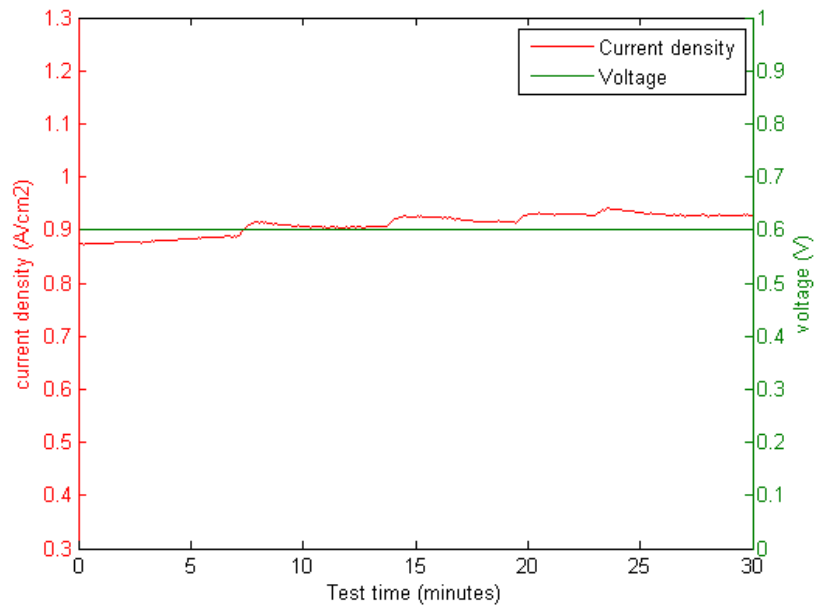


**Figure B.14** Performance profile in AICI flow field during discharge at 0.6V under standard operating condition for 30 minutes

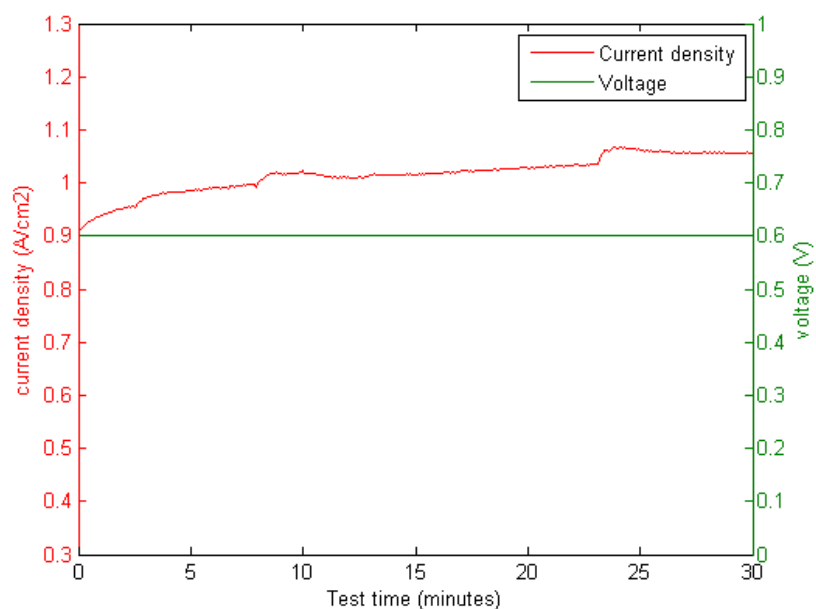


**Figure B.15** Performance profile in ASCS flow field during discharge at 0.6V under standard operating condition for 30 minutes

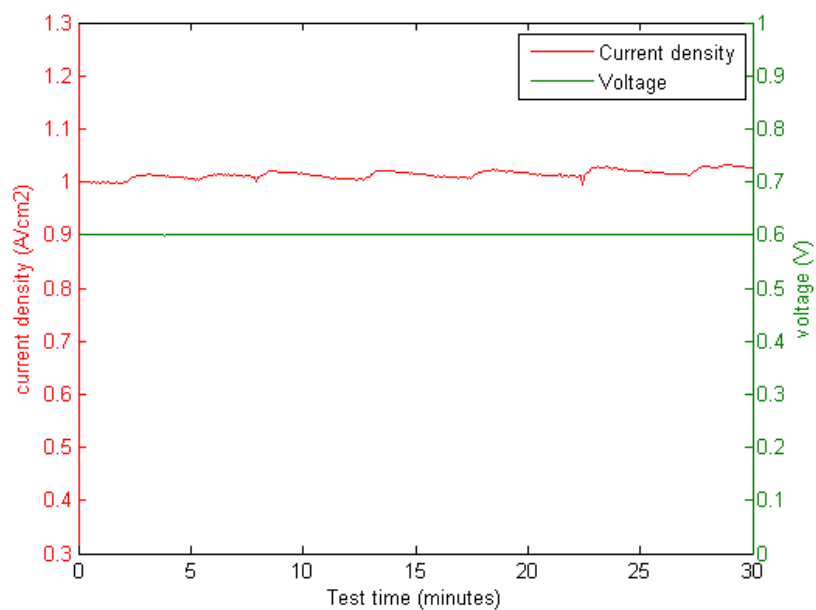


**Figure B.16** Performance in ASCI flow field during discharge at 0.6V under standard operating condition for 30 minutes

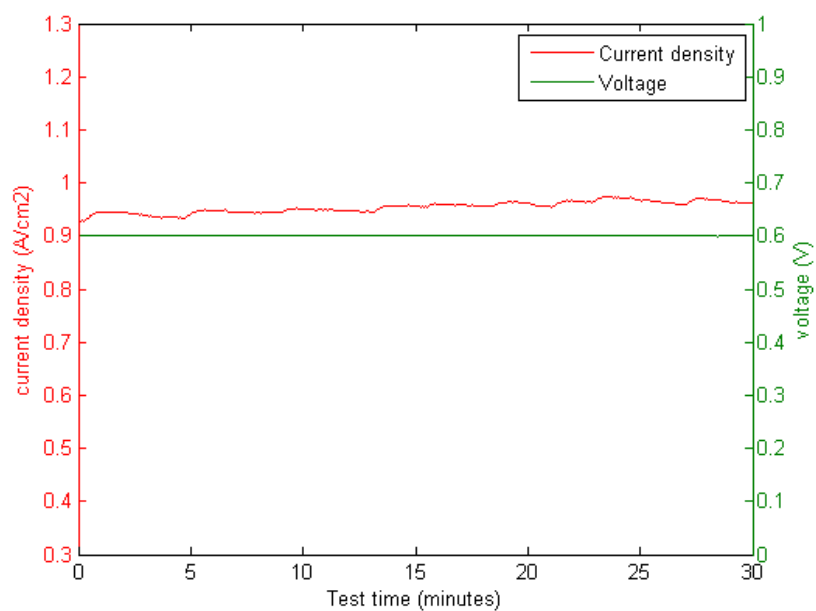


**Figure B.17** Performance profile in AICS flow field during discharge at 0.6V under standard operating condition for 30 minutes

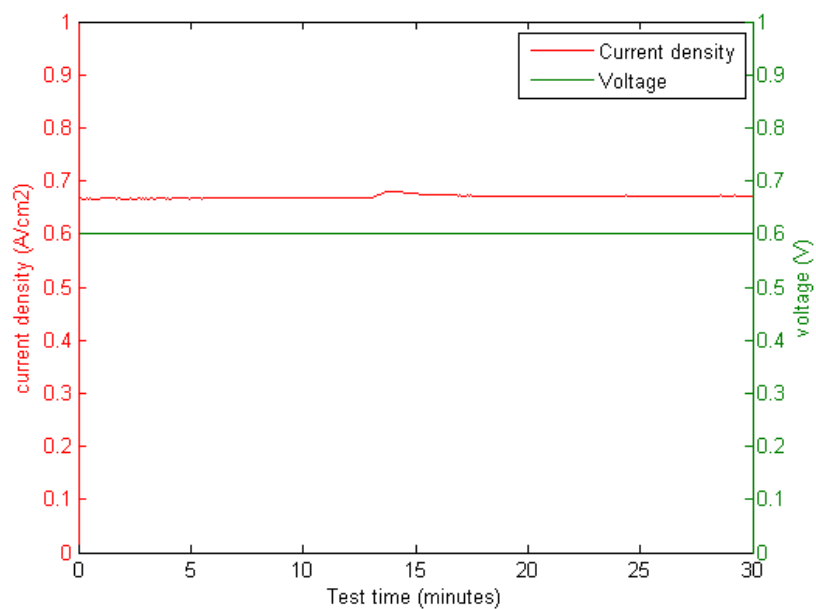


**Figure B.18** Performance profile in AICS flow field during discharge at 0.6V and 60°C for 30 minutes

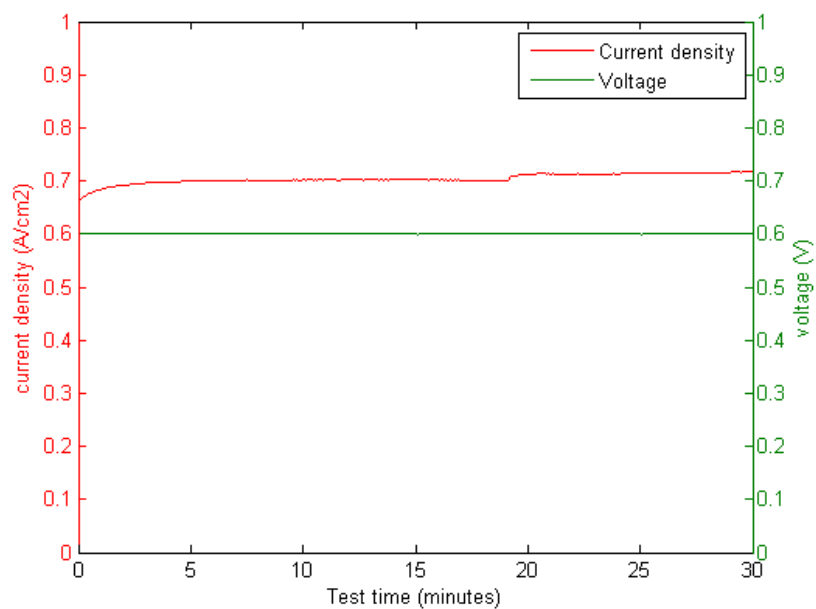


**Figure B.19** Performance profile in ASCS flow field during discharge at 0.6V and 60°C for 30 minutes

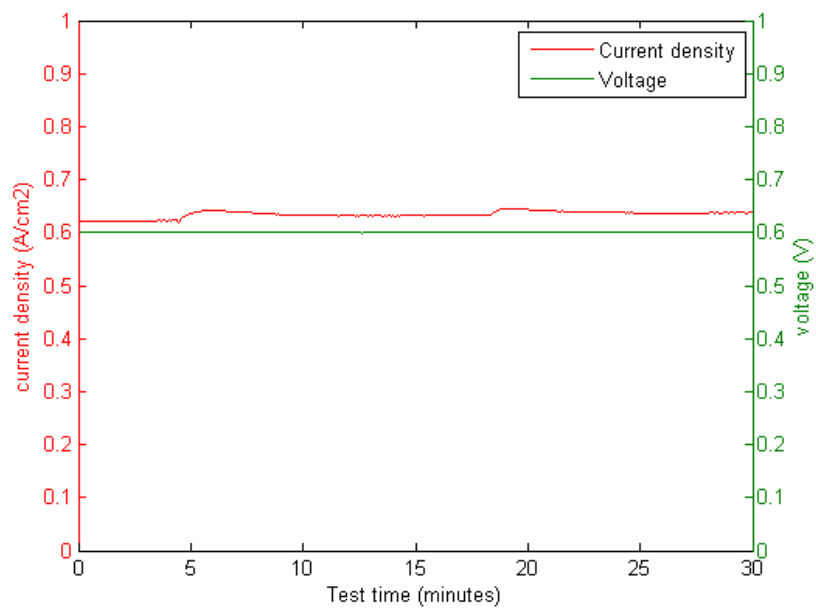


**Figure B.20** Performance profile in AICI flow field during discharge at 0.6V and 60°C for 30 minutes

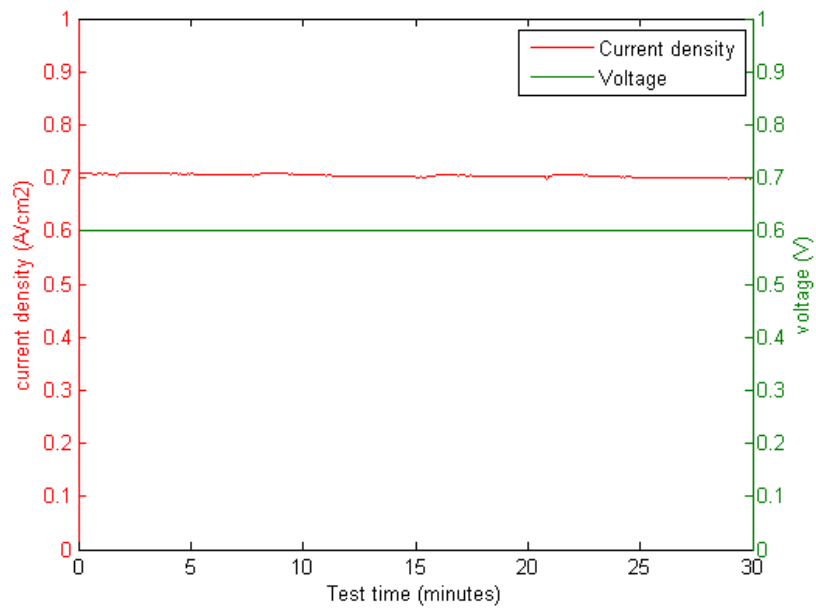


**Figure B.21** Performance profile in AICS flow field during discharge at 0.6V and cathode RH 50% for 30 minutes

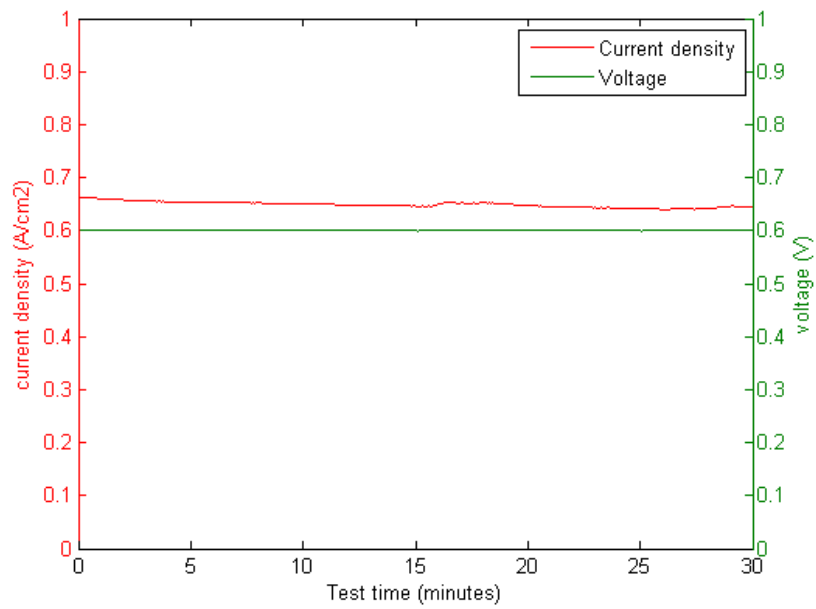


**Figure B.22** Performance profile in AICI flow field during discharge at 0.6V cathode RH 50% for 30 minutes

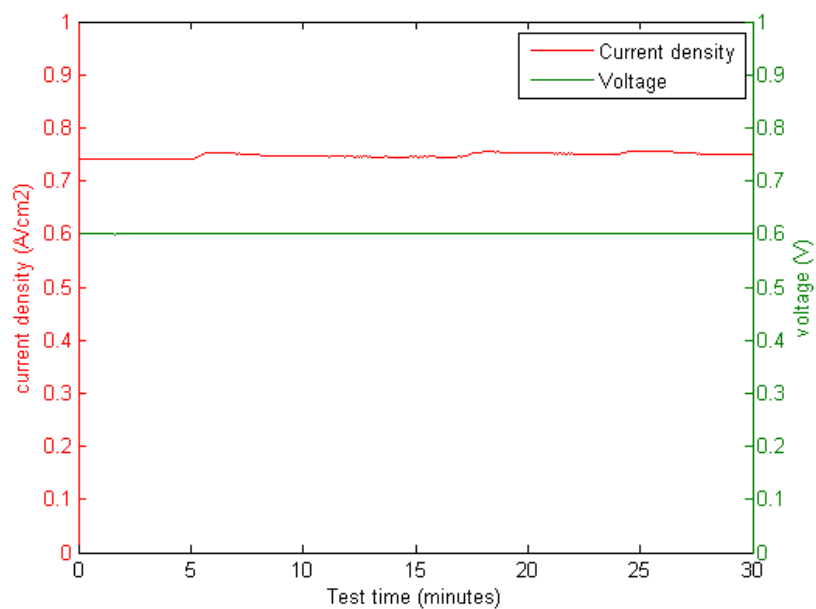


**Figure B.23** Performance profile in ASCS flow field during discharge at 0.6V and cathode RH 50% for 30 minutes

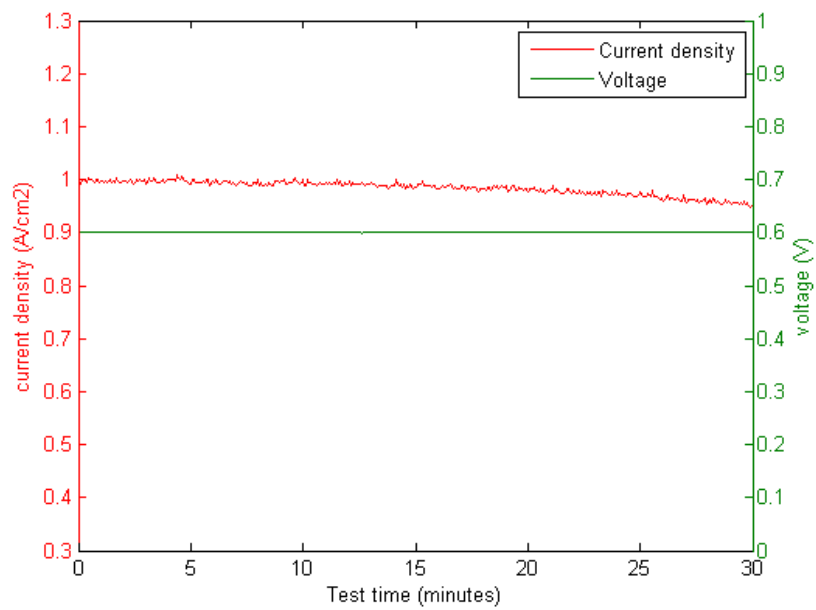


**Figure B.24** Performance profile in AICS flow field during discharge at 0.6V and oxygen flow rate of 4 slpm for 30 minutes

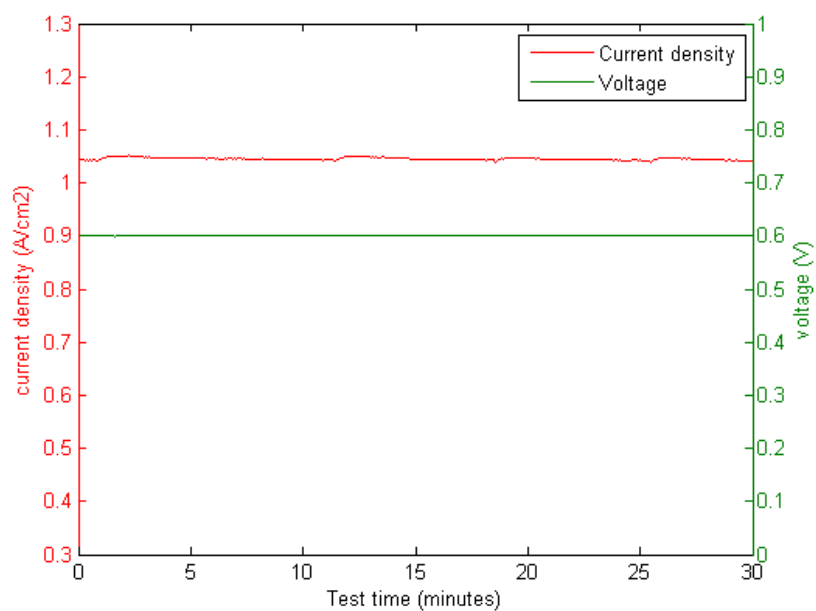


**Figure B.25** Performance profile in AICI flow field during discharge at 0.6V and oxygen flow rate of 4 slpm for 30 minutes

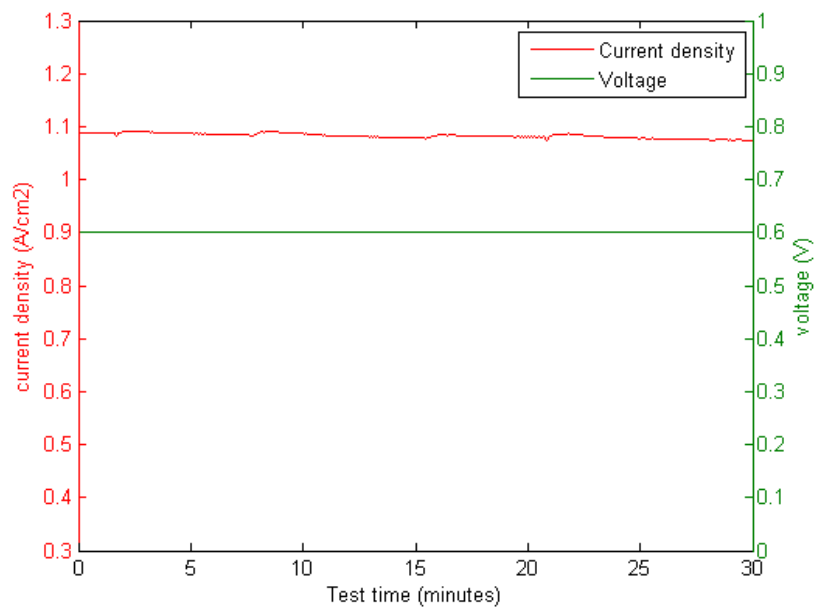


**Figure B.26** Performance profile in ASCS flow field during discharge at 0.6V and oxygen flow rate of 4 slpm for 30 minutes

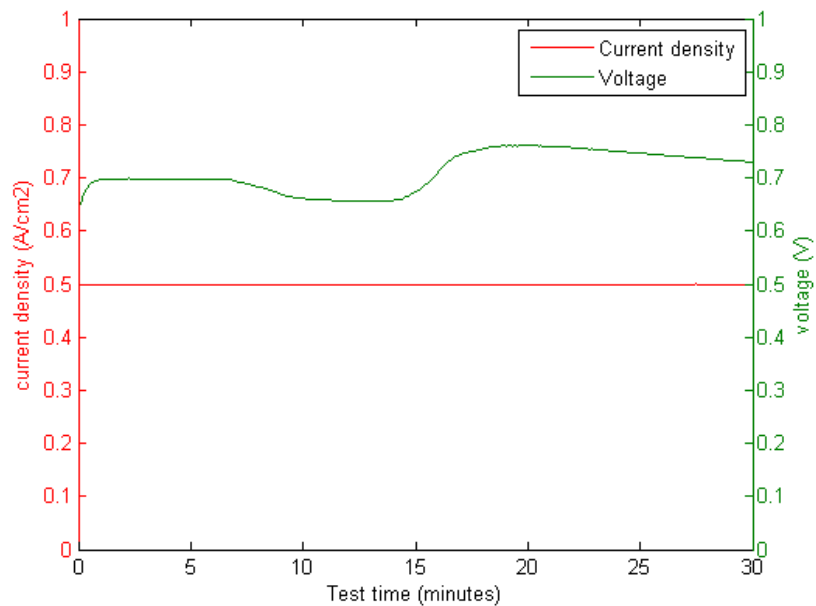


Figure B.27 Performance profile in ASCS flow field during discharge at 0.5A/cm<sup>2</sup> for 30 minutes

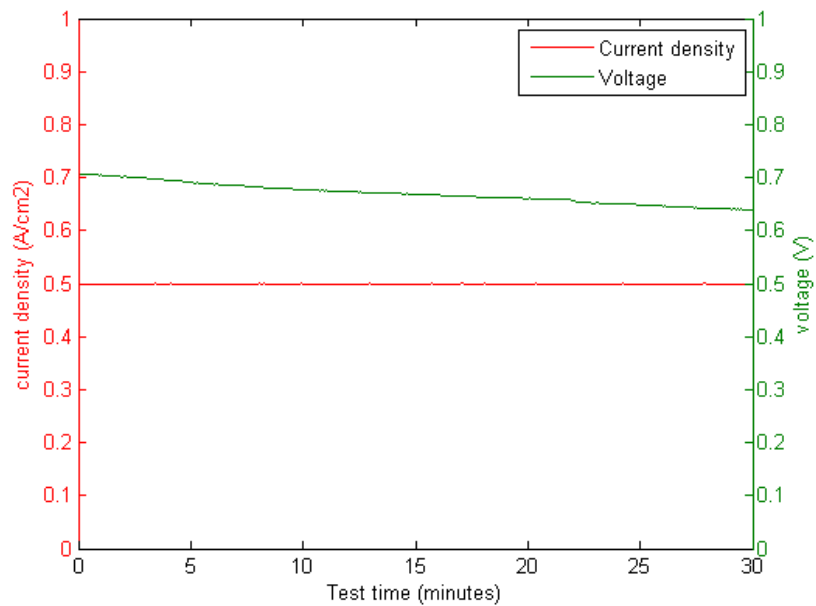


Figure B.28 Performance profile in AICS flow field during discharge at 0.5A/cm<sup>2</sup> for 30 minutes

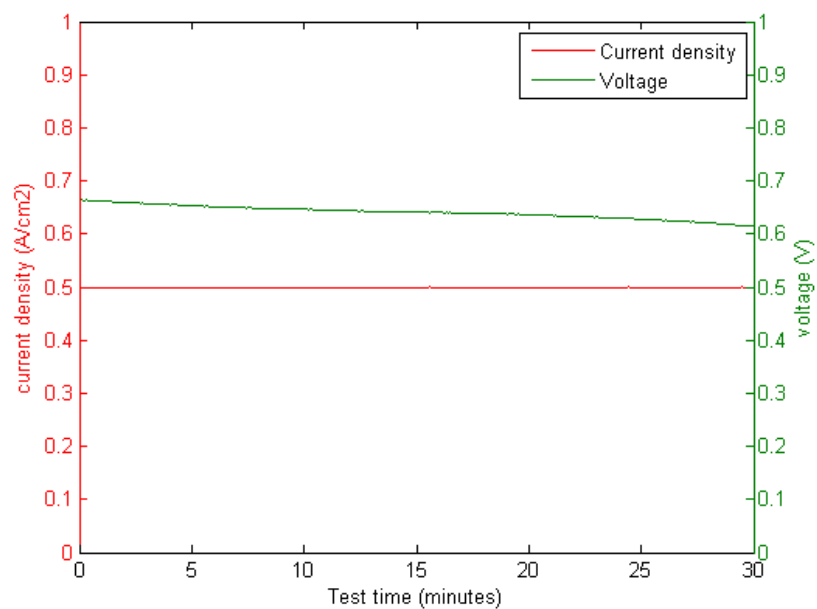


Figure B.29 Performance profile in AICI flow field during discharge at 0.5A/cm<sup>2</sup> for 30 minutes

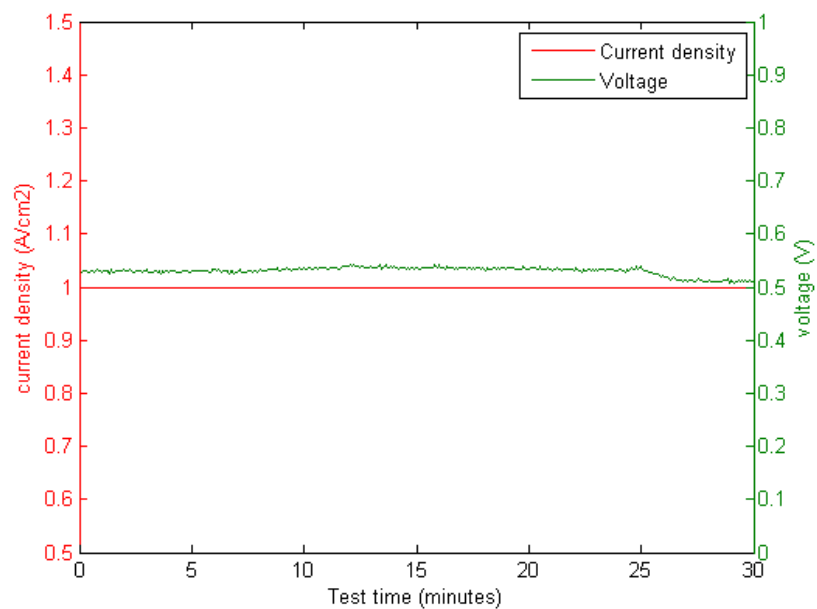


Figure B.30 Performance profile in AICS flow field during discharge at 1.0A/cm<sup>2</sup> for 30 minutes

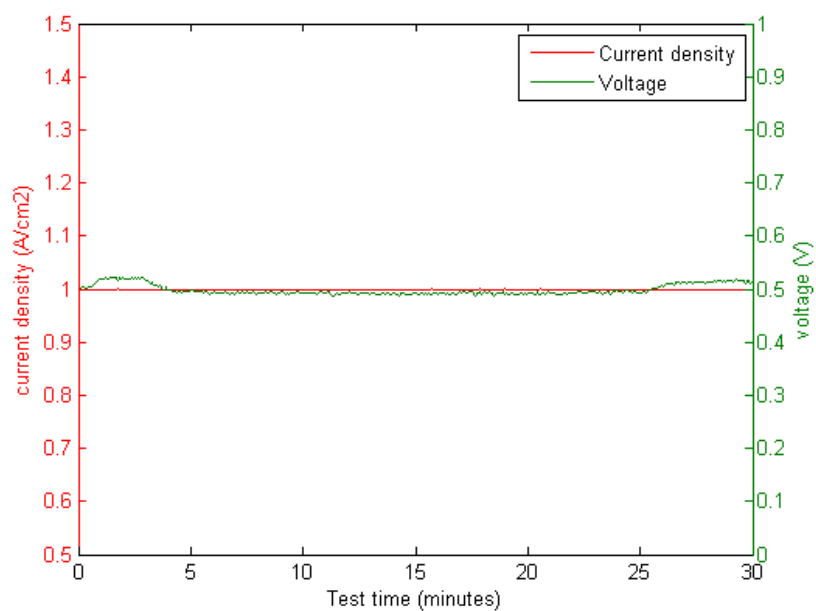


Figure B.31 Performance profile in AICI flow field during discharge at 1.0A/cm<sup>2</sup> for 30 minutes

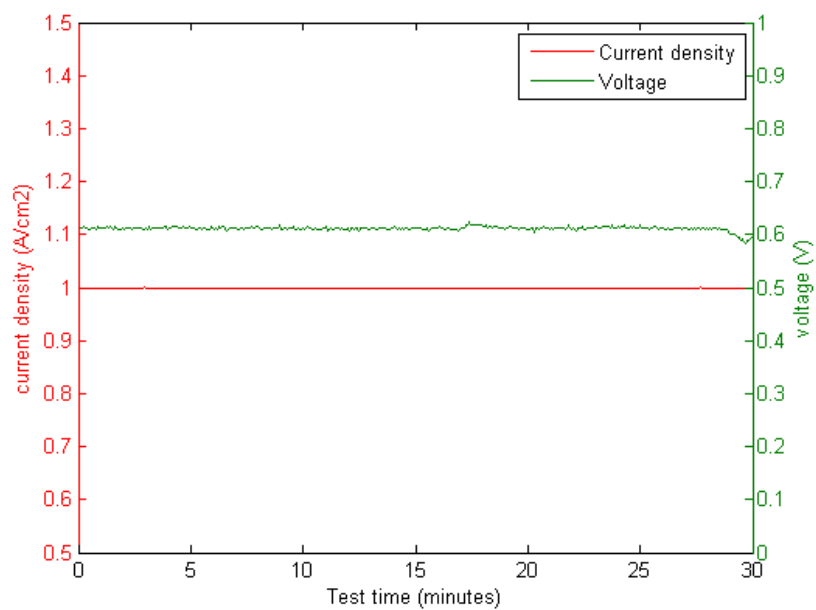


Figure B.32 Performance profile ASCS flow field during discharge at 1.0A/cm<sup>2</sup> for 30 minutes

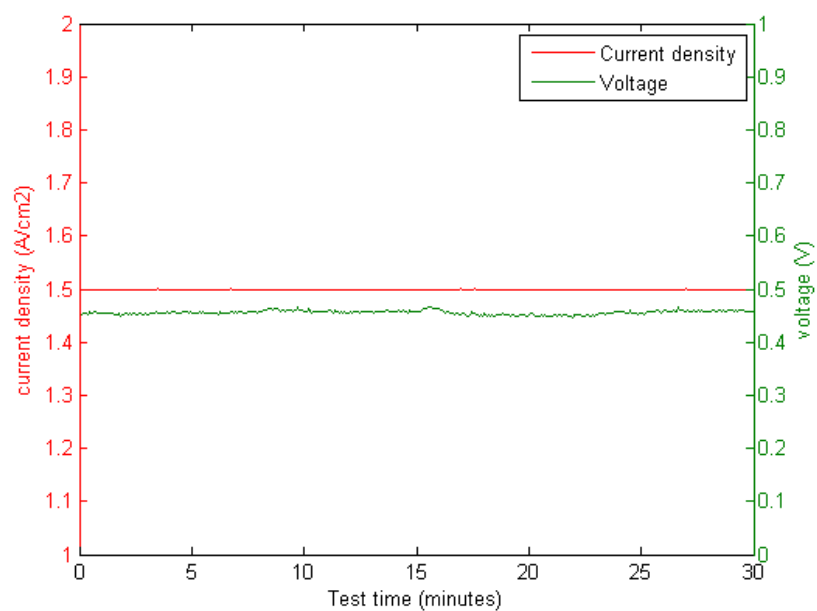


Figure B.33 Performance profile AICS flow field during discharge at  $1.5\text{A}/\text{cm}^2$  for 30 minutes

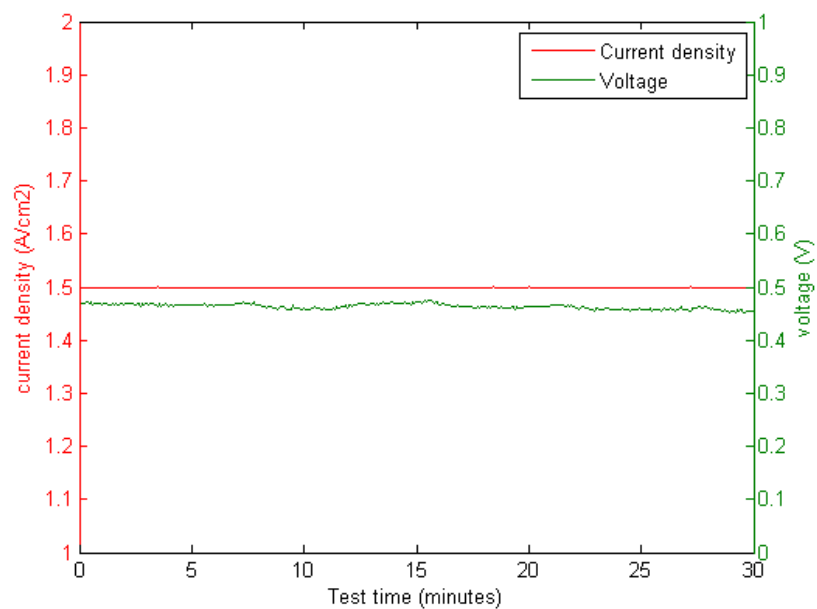


Figure B.34 Performance profile in AICI flow field during discharge at  $1.5\text{A}/\text{cm}^2$  for 30 minutes

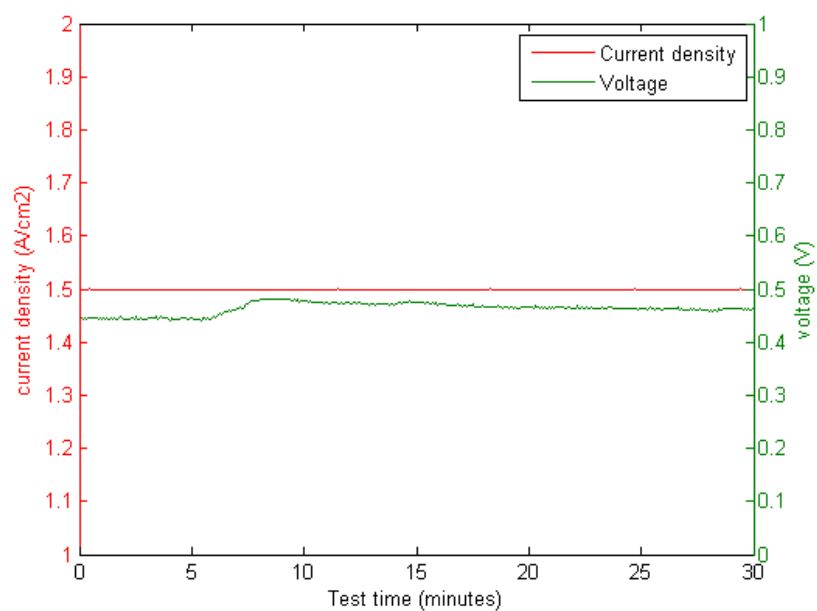


Figure B.35 Performance profile in ASCS flow field during discharge at  $1.5\text{A}/\text{cm}^2$  for 30 minutes

## Appendix C

### PERMISSION FOR FIGURE USAGE

Figure 1.1 and Fig. 1.2 in Chapter 1 were created by other researchers and used in their previous publications. To use those figures in this thesis, we got the permission from the authors and publisher.

Permission for using Fig. 1.1:



Fang Ruan <fang.amanda.ruan@gmail.com>

---

#### permission for using one figure in your paper

3 messages

---

**Fang Ruan** <fang.amanda.ruan@gmail.com>

Wed, Jan 8, 2014 at 4:54  
PM

To: Glenn Catlin <gcat84@gmail.com>

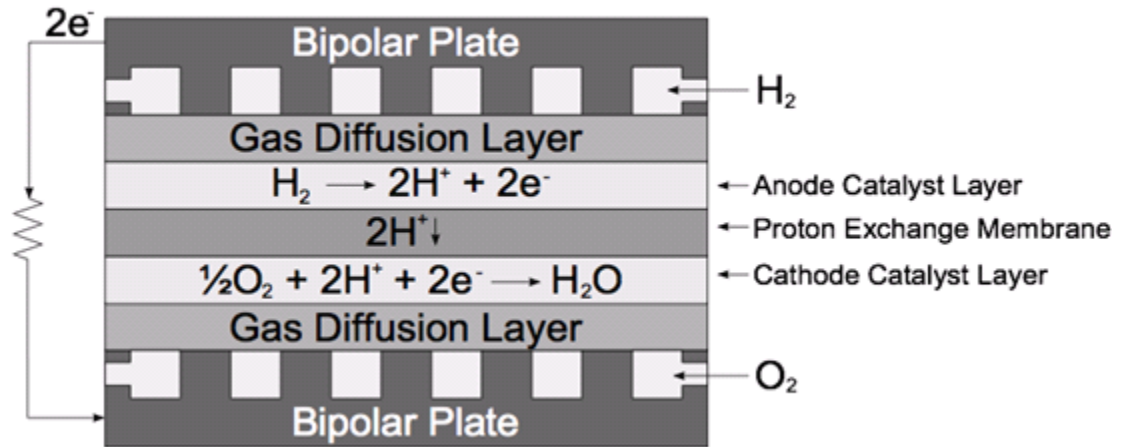
Hi Glenn,

I'm writing my master thesis now, and in the introduction part I used a figure in your thesis and I put your thesis in the reference list. Can you give me the permission for using this figure? Thanks a lot!

Best,

--

Fang



**Glenn Catlin** <gcat84@gmail.com>  
 To: Fang Ruan <fang.amanda.ruan@gmail.com>

Fri, Jan 10, 2014 at 6:10 AM

Hi Fang,

No problem, please go ahead and use any figures you would like with appropriate references to my work. I have included my article (which you probably already have). It might be useful to reference this article too.

Good luck on your writing!

-Glenn  
 [Quoted text hidden]

 **GCC-PEMFC-modeling-optimization.pdf**  
 2080K

**Fang Ruan** <fang.amanda.ruan@gmail.com>  
 To: Glenn Catlin <gcat84@gmail.com>

Fri, Jan 10, 2014 at 3:26 PM

Thanks a lot , Glenn!  
 [Quoted text hidden]  
 --  
 Fang

Permission for using Fig. 1.2:

**ELSEVIER LICENSE  
TERMS AND CONDITIONS**

Jan 27, 2014

This is a License Agreement between FANG RUAN ("You") and Elsevier ("Elsevier") provided by Copyright Clearance Center ("CCC"). The license consists of your order details, the terms and

conditions provided by Elsevier, and the payment terms and conditions.

All payments must be made in full to CCC. For payment instructions, please see information listed at the bottom of this form.

**Supplier** Elsevier Limited  
The Boulevard, Langford Lane  
Kidlington, Oxford, OX5 1GB, UK  
**Registered Company**

**Number**

1982084

**Customer name** FANG RUAN

**Customer address** 1063 MORSE AVE  
SUNNYVALE, CA 94089

**License number** 3317391148387

**License date** Jan 27, 2014

**Licensed content publisher** Elsevier

**Licensed content  
publication**

Journal of Power Sources

**Licensed content title** Performance studies of PEM fuel cells with interdigitated flow fields

**Licensed content author** Lin Wang, Hongtan Liu

**Licensed content date** 12 August 2004

**Licensed content volume  
number**

134

**Licensed content issue  
number**

2

**Number of pages** 12

**Start Page** 185

**End Page** 196

**Type of Use** reuse in a thesis/dissertation

**Portion** figures/tables/illustrations

**Number of  
figures/tables/illustrations**

1

**Format** both print and electronic

**Are you the author of this**

Elsevier article?

No

1/27/14 Rightslink Printable License  
<https://s100.copyright.com/AppDispatchServlet> 2/7

Will you be translating? No

Title of your  
thesis/dissertation

Net power output and pressure drop behavior of PEM fuel cells  
with serpentine and interdigitated flow fields

Expected completion date Feb 2014

Estimated size (number of  
pages)

106

Elsevier VAT number GB 494 6272 12

Permissions price 0.00 USD

VAT/Local Sales Tax 0.00 USD / 0.00 GBP

Total 0.00 USD

[Terms and Conditions](#)

## INTRODUCTION

1. The publisher for this copyrighted material is Elsevier. By clicking "accept" in connection with completing this licensing transaction, you agree that the following terms and conditions apply to this transaction (along with the Billing and Payment terms and conditions established by Copyright Clearance Center, Inc. ("CCC"), at the time that you opened your Rightslink account and that are available at any time at <http://myaccount.copyright.com>).

## GENERAL TERMS

2. Elsevier hereby grants you permission to reproduce the aforementioned material subject to the terms and conditions indicated.

3. Acknowledgement: If any part of the material to be used (for example, figures) has appeared in our publication with credit or acknowledgement to another source, permission must also be sought from that source. If such permission is not obtained then that material may not be included in your publication/copies. Suitable acknowledgement to the source must be made, either as a footnote or in a reference list at the end of your publication, as follows:  
"Reprinted from Publication title, Vol /edition number, Author(s), Title of article / title of chapter,

Pages No., Copyright (Year), with permission from Elsevier [OR APPLICABLE SOCIETY COPYRIGHT OWNER].” Also Lancet special credit -“Reprinted from The Lancet, Vol. number, Author(s), Title of article, PagesNo., Copyright (Year), with permission from Elsevier.”

4. Reproduction of this material is confined to the purpose and/or media for which permission is hereby given.

5. Altering/Modifying Material: Not Permitted. However figures and illustrations may be altered/adapted minimally to serve your work. Any other abbreviations, additions, deletions and/or any other alterations shall be made only with prior written authorization of Elsevier Ltd. (Please contact Elsevier at [permissions@elsevier.com](mailto:permissions@elsevier.com))

6. If the permission fee for the requested use of our material is waived in this instance, please be advised that your future requests for Elsevier materials may attract a fee.

1/27/14 Rightslink Printable License  
<https://s100.copyright.com/AppDispatchServlet> 3/7

7. Reservation of Rights: Publisher reserves all rights not specifically granted in the combination of (i) the license details provided by you and accepted in the course of this licensing transaction, (ii) these terms and conditions and (iii) CCC's Billing and Payment terms and conditions.

8. License Contingent Upon Payment: While you may exercise the rights licensed immediately upon issuance of the license at the end of the licensing process for the transaction, provided that you have disclosed complete and accurate details of your proposed use, no license is finally effective unless and until full payment is received from you (either by publisher or by CCC) as provided in CCC's Billing and Payment terms and conditions. If full payment is not received on a timely basis, then any license preliminarily granted shall be deemed automatically revoked and shall be void as if never granted. Further, in the event that you breach any of these terms and conditions or any of

CCC's Billing and Payment terms and conditions, the license is automatically revoked and shall be void as if never granted. Use of materials as described in a revoked license, as well as any use of the materials beyond the scope of an unrevoked license, may constitute copyright infringement and publisher reserves the right to take any and all action to protect its copyright in the materials.

9. Warranties: Publisher makes no representations or warranties with respect to the licensed material.

10. Indemnity: You hereby indemnify and agree to hold harmless publisher and CCC, and their respective officers, directors, employees and agents, from and against any and all claims arising out of your use of the licensed material other than as specifically authorized pursuant to this license.

11. No Transfer of License: This license is personal to you and may not be sublicensed, assigned, or transferred by you to any other person without publisher's written permission.

12. No Amendment Except in Writing: This license may not be amended except in a writing signed by both parties (or, in the case of publisher, by CCC on publisher's behalf).

13. Objection to Contrary Terms: Publisher hereby objects to any terms contained in any purchase order, acknowledgment, check endorsement or other writing prepared by you, which terms are inconsistent with these terms and conditions or CCC's Billing and Payment terms and conditions.

These terms and conditions, together with CCC's Billing and Payment terms and conditions (which are incorporated herein), comprise the entire agreement between you and publisher (and CCC) concerning this licensing transaction. In the event of any conflict between your obligations established by these terms and conditions and those established by CCC's Billing and Payment terms and conditions, these terms and conditions shall control.

14. Revocation: Elsevier or Copyright Clearance Center may deny the permissions described in this

License at their sole discretion, for any reason or no reason, with a full refund payable to you.

Notice of such denial will be made using the contact information provided by you. Failure to receive

such notice will not alter or invalidate the denial. In no event will Elsevier or Copyright Clearance

Center be responsible or liable for any costs, expenses or damage incurred by you as a result of a

denial of your permission request, other than a refund of the amount(s) paid by you to Elsevier

and/or Copyright Clearance Center for denied permissions.

#### LIMITED LICENSE

1/27/14 Rightslink Printable License

<https://s100.copyright.com/AppDispatchServlet> 4/7

The following terms and conditions apply only to specific license types:

15. Translation: This permission is granted for non-exclusive world English rights only unless

your license was granted for translation rights. If you licensed translation rights you may only translate

this content into the languages you requested. A professional translator must perform all translations

and reproduce the content word for word preserving the integrity of the article.

If this license is to reuse

1 or 2 figures then permission is granted for non-exclusive world rights in all languages.

16. Posting licensed content on any Website: The following terms and conditions apply as

follows: Licensing material from an Elsevier journal: All content posted to the web site must maintain

the copyright information line on the bottom of each image; A hyper-text must be included to the

Homepage of the journal from which you are licensing at

<http://www.sciencedirect.com/science/journal/xxxxx> or the Elsevier homepage for books at

<http://www.elsevier.com>; Central Storage: This license does not include permission for a scanned

version of the material to be stored in a central repository such as that provided by Heron/XanEdu.

Licensing material from an Elsevier book: A hyper-text link must be included to the Elsevier

homepage at <http://www.elsevier.com> . All content posted to the web site must maintain the

copyright information line on the bottom of each image.

Posting licensed content on Electronic reserve: In addition to the above the following

clauses are applicable: The web site must be password-protected and made available only to bona

fide students registered on a relevant course. This permission is granted for 1 year only. You may

obtain a new license for future website posting.

For journal authors: the following clauses are applicable in addition to the above: Permission

granted is limited to the author accepted manuscript version\* of your paper.

\*Accepted Author Manuscript (AAM) Definition: An accepted

author manuscript (AAM) is

the author's version of the manuscript of an article that has been accepted for publication and which

may include any author-incorporated changes suggested through the processes of submission

processing, peer review, and editor-author communications. AAMs do not include other

publisher value-added contributions such as copy-editing, formatting, technical enhancements and (if

relevant) pagination.

You are not allowed to download and post the published journal article (whether PDF or HTML,

proof or final version), nor may you scan the printed edition to create an electronic version. A

hyper-text must be included to the Homepage of the journal from which you are licensing at

<http://www.sciencedirect.com/science/journal/xxxxx>. As part of our normal production process,

you will receive an e-mail notice when your article appears on Elsevier's online service

ScienceDirect ([www.sciencedirect.com](http://www.sciencedirect.com)). That e-mail will include the article's Digital

Object Identifier (DOI). This number provides the electronic link to the published article and should

be included in the posting of your personal version. We ask that you wait until you receive this email

and have the DOI to do any posting.

Posting to a repository: Authors may post their AAM immediately to their employer's institutional

repository for internal use only and may make their manuscript publically available after the journal

27/14 Rightslink Printable License

<https://s100.copyright.com/AppDispatchServlet> 5/7

specific embargo period has ended.

Please also refer to Elsevier's Article Posting Policy for further information.

18. For book authors the following clauses are applicable in addition to the above: Authors are

permitted to place a brief summary of their work online only. You are not allowed to download and

post the published electronic version of your chapter, nor may you scan the printed edition to create

an electronic version. Posting to a repository: Authors are permitted to post a summary of their

chapter only in their institution's repository.

20. Thesis/Dissertation: If your license is for use in a thesis/dissertation your thesis may be

submitted to your institution in either print or electronic form. Should your thesis be published

commercially, please apply for permission. These requirements include permission for the

Library and Archives of Canada to supply single copies, on demand, of the complete thesis and

include permission for UMI to supply single copies, on demand, of the complete thesis. Should your

thesis be published commercially, please apply for permission.

Elsevier Open Access Terms and Conditions

Elsevier publishes Open Access articles in both its Open Access journals and via its Open Access

articles option in subscription journals.

Authors publishing in an Open Access journal or who choose to make their article Open Access in

an Elsevier subscription journal select one of the following Creative Commons user licenses, which

define how a reader may reuse their work: Creative Commons Attribution License (CC BY),

Creative Commons Attribution – Non Commercial - ShareAlike (CC BY NCSA) and Creative Commons Attribution – Non Commercial – No Derivatives (CC BYNC ND) Terms & Conditions applicable to all Elsevier Open Access articles:

Any reuse of the article must not represent the author as endorsing the adaptation of the article nor should the article be modified in such a way as to damage the author's honour or reputation.

The author(s) must be appropriately credited.

If any part of the material to be used (for example, figures) has appeared in our publication with credit or acknowledgement to another source it is the responsibility of the user to ensure their reuse complies with the terms and conditions determined by the rights holder.

Additional Terms & Conditions applicable to each Creative Commons user license:

CC BY: You may distribute and copy the article, create extracts, abstracts, and other revised versions, adaptations or derivative works of or from an article (such as a translation), to include in a collective work (such as an anthology), to text or data mine the article, including for commercial purposes without permission from Elsevier

1/27/14 Rightslink Printable License  
<https://s100.copyright.com/AppDispatchServlet/6/7>

CC BY NC SA: For non-commercial purposes you may distribute and copy the article, create extracts, abstracts and other revised versions, adaptations or derivative works of or from an article (such as a translation), to include in a collective work (such as an anthology), to text and data mine the article and license new adaptations or creations under identical terms without permission from Elsevier

CC BY NC ND: For non-commercial purposes you may distribute and copy the article and include it in a collective work (such as an anthology), provided you do not alter or modify the article, without permission from Elsevier

Any commercial reuse of Open Access articles published with a CC BY NC SA

or CC BY NC NDlicense requires permission from Elsevier and will be subject to a fee.

Commercial reuse includes:

- Promotional purposes (advertising or marketing)
- Commercial exploitation ( e.g. a product forsale or loan)
- Systematic distribution (for a fee or free ofcharge)

Please refer to Elsevier'sOpen Access Policy for further information.

## 21. Other Conditions:

v1.7

If you would like to pay for this license now, please remit this license along with your payment made payable to "COPYRIGHT CLEARANCE CENTER" otherwise you will be invoiced within 48 hours of the license date. Payment should be in the form of a check or money order referencing your account number and this invoice number RLNK501212311. Once you receive your invoice for this order, you may pay your invoice by credit card. Please follow instructions provided at that time.

Make Payment To:

Copyright Clearance Center  
Dept 001  
P.O. Box 843006  
Boston, MA 02284-3006

For suggestions or comments regarding this order, contact RightsLink Customer Support: [customercare@copyright.com](mailto:customercare@copyright.com) or +1-877-622-5543 (toll free in the US) or +1-978-646-2777.

Gratis licenses (referencing \$0 in the Total field) are free. Please retain this printable

license for your reference. No payment is required.